

IOWA STATE UNIVERSITY

Digital Repository

Retrospective Theses and Dissertations

Iowa State University Capstones, Theses and
Dissertations

1984

Falling film evaporation on horizontal tubes with smooth and structured surfaces

Ming-Chien Chyu
Iowa State University

Follow this and additional works at: <https://lib.dr.iastate.edu/rtd>



Part of the [Mechanical Engineering Commons](#)

Recommended Citation

Chyu, Ming-Chien, "Falling film evaporation on horizontal tubes with smooth and structured surfaces" (1984). *Retrospective Theses and Dissertations*. 8154.
<https://lib.dr.iastate.edu/rtd/8154>

This Dissertation is brought to you for free and open access by the Iowa State University Capstones, Theses and Dissertations at Iowa State University Digital Repository. It has been accepted for inclusion in Retrospective Theses and Dissertations by an authorized administrator of Iowa State University Digital Repository. For more information, please contact digirep@iastate.edu.

INFORMATION TO USERS

This reproduction was made from a copy of a document sent to us for microfilming. While the most advanced technology has been used to photograph and reproduce this document, the quality of the reproduction is heavily dependent upon the quality of the material submitted.

The following explanation of techniques is provided to help clarify markings or notations which may appear on this reproduction.

1. The sign or "target" for pages apparently lacking from the document photographed is "Missing Page(s)". If it was possible to obtain the missing page(s) or section, they are spliced into the film along with adjacent pages. This may have necessitated cutting through an image and duplicating adjacent pages to assure complete continuity.
2. When an image on the film is obliterated with a round black mark, it is an indication of either blurred copy because of movement during exposure, duplicate copy, or copyrighted materials that should not have been filmed. For blurred pages, a good image of the page can be found in the adjacent frame. If copyrighted materials were deleted, a target note will appear listing the pages in the adjacent frame.
3. When a map, drawing or chart, etc., is part of the material being photographed, a definite method of "sectioning" the material has been followed. It is customary to begin filming at the upper left hand corner of a large sheet and to continue from left to right in equal sections with small overlaps. If necessary, sectioning is continued again—beginning below the first row and continuing on until complete.
4. For illustrations that cannot be satisfactorily reproduced by xerographic means, photographic prints can be purchased at additional cost and inserted into your xerographic copy. These prints are available upon request from the Dissertations Customer Services Department.
5. Some pages in any document may have indistinct print. In all cases the best available copy has been filmed.

University
Microfilms
International
300 N. Zeeb Road
Ann Arbor, MI 48106

8505808

Chyu, Ming-Chien

FALLING FILM EVAPORATION ON HORIZONTAL TUBES WITH SMOOTH
AND STRUCTURED SURFACES

Iowa State University

Ph.D. 1984

**University
Microfilms
International** 300 N. Zeeb Road, Ann Arbor, MI 48106

Falling film evaporation on horizontal tubes

with

smooth and structured surfaces

by

Ming-Chien Chyu

A Dissertation Submitted to the
Graduate Faculty in Partial Fulfillment of the
Requirements for the Degree of
DOCTOR OF PHILOSOPHY
Major: Mechanical Engineering

Approved:

Signature was redacted for privacy.

In Charge of Major Work

Signature was redacted for privacy.

For the Major Department

Signature was redacted for privacy.

For the Graduate College

Iowa State University
Ames, Iowa
1984

TABLE OF CONTENTS

	<u>Page</u>
NOMENCLATURE	xii
I. INTRODUCTION	1
II. LITERATURE REVIEW	6
A. Taxonomical Consideration of the Literature	6
1. Convection-Enhancing vs. Boiling-Enhancing Surfaces	6
2. Vertical Tube or Plate vs. Horizontal Tube	6
B. Summary of Previous Work	8
1. Falling film evaporation on a horizontal tube with plain surface	8
2. Falling film evaporation on a horizontal tube with enhanced surface	12
3. Structured Heat Transfer Surfaces	23
C. Objectives of Research	30
III. ANALYSIS OF FALLING FILM EVAPORATION ON A HORIZONTAL TUBE	31
A. Introduction	31
B. Jet Impingement Region	32
C. Thermal Developing Region	36
D. Fully Developed Region	44
IV. EXPERIMENT	52
A. Apparatus	52
1. General Arrangement	52
2. Test Cylinders	58
3. Instrumentation	60
B. Experimental Procedure	62

C. Data Reduction	68
V. RESULTS AND DISCUSSION	72
A. Test Section 1 - Plain Surface	72
1. General heat transfer behavior	72
2. Effect of film flowrate	75
3. Effect of liquid feed height	77
4. Comparison of falling film evaporation and pool boiling	81
B. Test Section GEWA-T - Deformed Fin Surface	86
1. General heat transfer behavior	86
2. Effect of film flowrate	89
3. Effect of liquid feed height	91
4. Comparison of falling film evaporation and pool boiling	91
C. Test Section TE - Thermoexcel-E Surface	91
1. General heat transfer behavior	91
2. Flooded tests	97
3. Mechanism	101
4. Comparison of falling film evaporation and pool boiling	103
5. Effects of film flowrate and liquid feed height	105
6. Summary	108
D. Test Section HF - High Flux Porous Surface	110
1. General heat transfer behavior	110
2. Effect of film flowrate	114
3. Effect of liquid feed height	114
4. Comparison of falling film evaporation and pool boiling	114
5. Fouling	118
6. Summary	127

E. Summary of Results and General Discussion	129
1. Liquid supply mode	129
2. Heat transfer surface	129
3. Surface aging	133
4. Surface subcooling	134
5. Heat flux	134
6. Film flowrate	135
7. Liquid feed height	136
8. Rate of heat flux change	136
VI. CONCLUSIONS AND RECOMMENDATIONS	138
VII. REFERENCES	143
VIII. ACKNOWLEDGMENTS	150
IX. APPENDIX 1: DESIGN OF A PERFORATED-PIPE FLOW DISTRIBUTOR	152
X. APPENDIX 2: LOCATING THE THERMOCOUPLES	155
A. Introduction	155
B. Method	156
XI. APPENDIX 3: CALIBRATION OF INSTRUMENTS	159
A. Calibration of Temperature Measurement System	159
1. Introduction	159
2. Calibration	159
a. Experiment	159
b. Statistics	162
3. Conclusion	164
B. Calibration of Wattmeter	164
C. Calibration of Flowmeter	165

XII. APPENDIX 4: HEAT CONDUCTION STUDY OF THE TEST SECTION	167
A. Effect of Axially Non-Uniform Heat Flux Distribution at Inner Surface	167
1. Introduction	167
2. Analytical solution	169
B. Identification and Effect of the Circumferentially Non-Uniform Heat Flux Distribution at Inner Surface	175
1. Introduction	175
2. Analytical model	178
3. Experiment	184
4. Results and discussion	187
5. Conclusion	191
C. Effect of Circumferentially Non-Uniform Heat Transfer Coefficient Distribution at Outside Surface	191
1. Introduction	191
2. Analytical solution	192
3 Conclusion	197
XIII. APPENDIX 5: EXAMPLES OF COMPUTER PROGRAMS FOR DATA ACQUISITION AND REDUCTION	198
A. Computer Program for Falling Film Evaporation Test with High Flux Surface	198
B. Computer Program for Pool Boiling Test With High Flux Surface	201
XIV. APPENDIX 6: ERROR ANALYSIS	204

LIST OF FIGURES

	<u>Page</u>
Fig. 1. Horizontal spray-film evaporator	2
Fig. 2. Cross section of a GEWA-T tube (exaggerated)	25
Fig. 3. Geometry of the Thermoexcel-E surface	27
Fig. 4. Conceptual model of boiling in a porous matrix of sintered metallic particles	28
Fig. 5. Model for falling film evaporation on a horizontal tube	33
Fig. 6. Distribution of velocity at the outer surface of the hydrodynamic boundary layer in the jet impingement region	34
Fig. 7. Progress of temperature profile in the thermal developing region	40
Fig. 8. Angular position at the end of thermal developing region	42
Fig. 9. Variation of film thickness with respect to angular position	43
Fig. 10. Analytical prediction of average Nusselt number in the fully developed region	51
Fig. 11. Test facility for falling film evaporation and pool boiling on a horizontal tube	53
Fig. 12. Test chamber for falling film evaporation and pool boiling tests	54
Fig. 13. Flow distributor assembly	57

	<u>Page</u>
Fig. 14. Effect of surface aging, surface subcooling, heat flux change rate, and direction of power change on falling film evaporation heat transfer of a plain tube, $\Gamma = 0.0606 \text{ kg/s-m}$	73
Fig. 15. Effect of film Reynolds number on the falling film evaporation heat transfer coefficient of a plain tube	76
Fig. 16. Effect of flowrate on the heat transfer performance of a plain tube	78
Fig. 17. Effect of liquid feed height on the falling film evaporation heat transfer coefficient of a plain tube	79
Fig. 18. Effect of liquid feed height on falling film evaporation heat transfer of a plain tube	82
Fig. 19. Comparison of typical falling film evaporation and pool boiling data for a plain tube	83
Fig. 20. q'' vs. ΔT curves of FFE-GEWA-T19C tests	87
Fig. 21. q'' vs. ΔT curves of FFE-GEWA-T26B tests	88
Fig. 22. Effect of film Reynolds number on the falling film evaporation heat transfer coefficient of the GEWA-T26B surface	90
Fig. 23. Effect of liquid feed height on the falling film evaporation heat transfer coefficient of the GEWA-T26B surface	92
Fig. 24. Comparison of falling film evaporation and pool boiling data for the GEWA-T tube	93

	<u>Page</u>
Fig. 25. q'' vs. ΔT curves of FFE-TE-B tests	95
Fig. 26. q'' vs. ΔT curves of FFE-TE-D tests	96
Fig. 27. PB-TE-B curves	98
Fig. 28. PB-TE-D curves	99
Fig. 29. Comparison of the falling film evaporation and pool boiling for the Thermoexcel-E surface	104
Fig. 30. Effect of film Reynolds number on the falling film evaporation coefficient of the Thermoexcel-E tube	106
Fig. 31. Effect of liquid feed height on the falling film evaporation coefficient of the Thermoexcel-E tube	107
Fig. 32. Summary plot for the Thermoexcel-E surface	109
Fig. 33. q'' vs. ΔT curves of FFE-HF-B tests	111
Fig. 34. q'' vs. ΔT curves of FFE-HG-D tests	112
Fig. 35. Effect of film Reynolds number on falling film evaporation coefficient of the High Flux surface	115
Fig. 36. Effect of liquid feed height on the falling film evaporation coefficient of the High Flux Surface	116
Fig. 37. Comparison of the falling film evaporation and the pool boiling performances of the High Flux surface	117
Fig. 38. Fouled High Flux porous surface (160X)	119
Fig. 39. Degradation of porous surface performance with time due to fouling	124

	<u>Page</u>
Fig. 40. Summary plot for the performance of High Flux porous surface	128
Fig. 41. Comparison of heat transfer performance of different surfaces	132
Fig. A1. Perforated-pipe fluid distributor	154
Fig. A2. Technique to measure the radial distance between the bottom of thermocouple well and the tube surface (not to scale)	157
Fig. A3. Calibration of temperature measurement system	161
Fig. A4. Calibration curve for temperature measurement system	163
Fig. A5. Watlow Firerod J6A36 Cartridge Heater, 1kW, 240v	168
Fig. A6. Heat conduction problem with step change in heat flux at inner boundary of a hollow cylinder	170
Fig. A7. Influence of inactive zone in the heater on the temperature distribution in the test cylinder	176
Fig. A8. Influence of inactive zone in the heater on the radial heat flux distribution in the test cylinder	177
Fig. A9. Heat conduction problem with non-uniform heat flux at the inner boundary of a hollow cylinder	180
Fig. A10. Test facility to investigate circumferential heat flux distribution at inner surface of the test tube	185
Fig. A11. A typical circumferential temperature profile at the outside surface of the cylinder	188

Fig. A12. Heat conduction problem with non-uniform heat flux at
outer boundary of a hollow cylinder

193

Fig. A13. Schematic profiles of heat flux, temperature, and
heat transfer coefficient at the outer surface of
the hollow cylinder

196

LIST OF TABLES

	<u>Page</u>
Table 1. Spray-film applications	4
Table 2. Summary of investigations on thin film evaporation on horizontal tubes with enhanced surfaces	13
Table 3. Example of calculating the integral in eq. (37), $\phi_d = 25^\circ$, A = 2828	49

NOMENCLATURE

A	area
D	outside diameter of tube
g	acceleration of gravity
H	liquid feed height
h	heat transfer coefficient; hydraulic head
\bar{h}	average heat transfer coefficient
h_{fg}	specific latent heat of vaporization
k	thermal conductivity
KE	kinetic energy
L	length
Q	volumetric rate of flow
q'	heat transfer rate per unit length of tube
q''	surface heat flux, or heat transfer rate per unit area
R	radius
r	radial coordinate in a cylindrical coordinate system
Re	film Reynolds number, $4R/u_f$
T	temperature
ΔT	temperature difference; wall superheat
$\bar{\Delta T}$	average wall superheat
u	velocity
\bar{u}	average velocity
w	jet width
x	distance along the film length
y	distance in the direction normal to the heating surface

z axial coordinate in a cylindrical coordinate system
 α thermal diffusivity, $k/\rho C_p$
 Γ mass flow rate of film per unit length of tube
 δ film thickness
 θ angular coordinate in a cylindrical coordinate system
 μ dynamic viscosity
 ν kinematic viscosity
 ρ density
 τ time
 ϕ angular position

Subscripts

aux auxiliary
c convective
d developing
f liquid; film
fd fully developed
g gas; vapor
i inner surface; inlet condition; impingement
j jet
ind indicated
max maximum
min minimum
NB nucleate boiling
o outer surface; outlet condition
p pipe

s saturation; stagnation

v variation

w wall

Δr radial distance between the thermocouple bead and the base surface

∞ condition well away from the heat transfer surface

I. INTRODUCTION

Heat transfer through the process of falling film evaporation has been widely employed in heat exchange devices in chemical, refrigeration, petroleum refining, desalination, dairy, brewing, and coke industries. The horizontal-tube falling-film evaporator usually consists of a bundle of horizontal tubes connected by headers at each end as in a conventional shell-and-tube heat exchanger. In this case, however, the shell-side liquid flow is introduced through spray nozzles at the top of the bundle. Falling, evaporating films are then formed on the outside tube surfaces. Thus, the liquid falls by gravity from tube to tube, redistributing itself on each tube. A typical horizontal-tube falling film evaporator is shown in Fig. 1 [1].

The principal advantages of horizontal-tube falling film evaporators are high heat transfer rates at small temperature differences and low liquid requirement as compared with flooded bundle evaporators. Since there is no liquid pool, the effect of hydrostatic head on the heat transfer is eliminated. The formation of scale on the tube side in a vertical-tube falling film evaporator can reduce the liquid flow in the tube, thereby accelerating the formation of additional scale. By contrast, in a horizontal-tube evaporator, since the film flow is on the outside tube surfaces, the possibility of scale build-up blocking the liquid flow is minimal, and the shell-side deposit is easier to remove. The horizontal-tube falling film evaporators also show advantages over vertical-tube evaporators in dealing with problems such as liquid distribution, leveling, non-condensable gases on the tube side, and liquid entrainment [1].

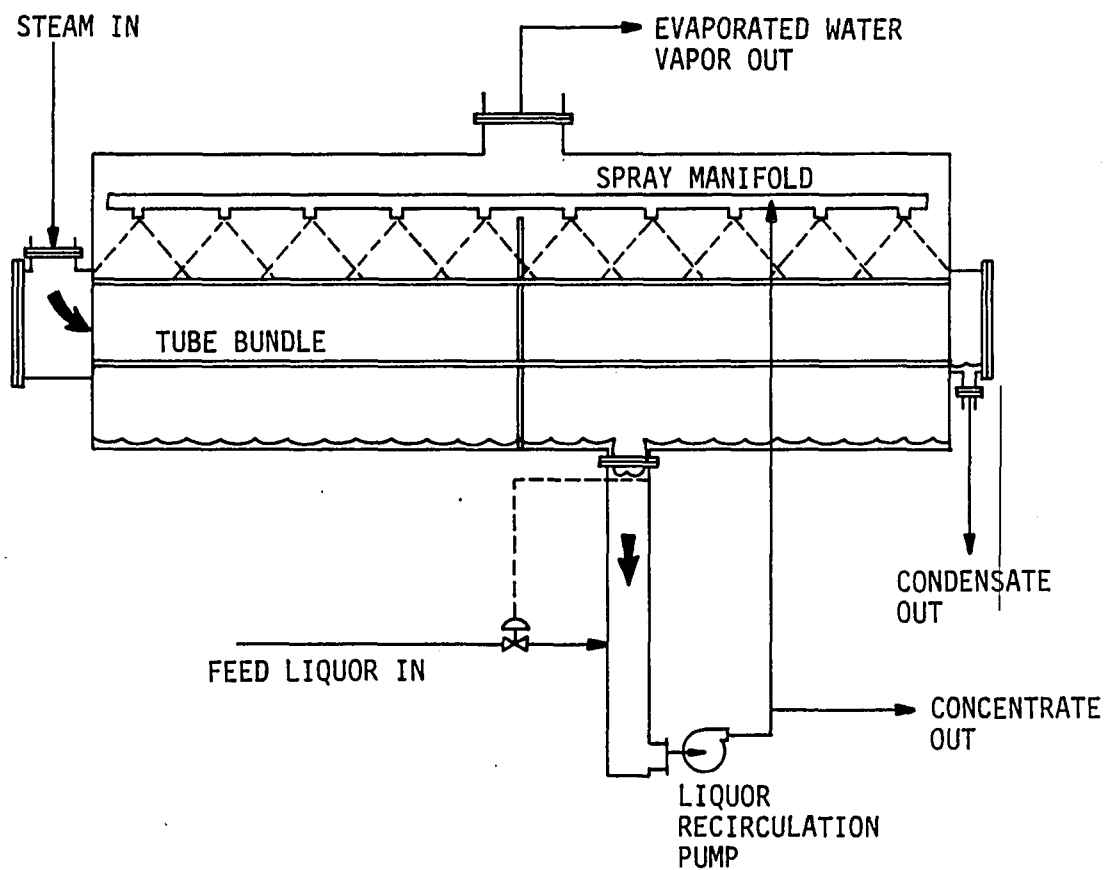


Fig. 1. Horizontal spray-film evaporator

Horizontal falling-film evaporators have been installed in a wide variety of commercial applications in the chemical process industries, as indicated in Table 1 [1]. This type of evaporator is used widely in concentrating chemicals that are sensitive to heat, such as ammonium nitrate and urea. Here, minimum heating time is desirable to prevent decomposition. In the closed cycle ocean thermal energy conversion system, a horizontal tube spray film evaporator was proposed to operate at low temperature difference without introducing hydrostatic head problems [2].

The horizontal tube multiple effect (HTME) distillation system incorporates horizontal heat transfer tube bundles with steam condensing on the inside of the tubes and brine vaporizing on the outside. The HTME process may produce potable water more economically than other systems due to the efficient heat transfer realized by the thin film evaporation and the elimination of many of the intereffect pumps and the associated equipment.

As is the case for most industrial heat exchangers, there is a strong incentive to improve horizontal-tube falling film evaporators. The objective may be to increase the evaporative capacity of a given heat exchanger, reduce heat exchanger size for a specified evaporative capacity, or reduce the overall temperature driving force required. In the case where the falling film is heated by condensing steam, the heat transfer rate is controlled by the heat transfer coefficient on the evaporating side. Enhancement of heat transfer on the evaporating side can make possible a reduction in both the first cost and the operating cost, due to the lower temperature difference required. To achieve this goal, a few special heat transfer surfaces have been considered and tested so far, as will be described in the literature review. In addition, a variety of

Table 1. Spray-film applications [1]

Configuration	Liquor	Application
Multiple Effect	Sulfite Liquor	Chemical Recovery
	Caustic Solution	Chemical Recovery
	Corn Syrup	Product Concentration
	Seawater	Fresh Water Production
	Spent Grains	Byproduct Recovery
	Demineralizer Waster	Waste Disposal
Vapor Compression	Fructose/Dextrose	Product Concentration
	Maple Sugar	Product Concentration
	Caustic Soda	Product Concentration
	Sodium Bicarbonate	Product Concentration
	Organic Intermediate	Product Concentration
	Seawater	Fresh Water Production
	Sulfite Liquor	Chemical Recovery
	Photo Waste	Chemical Recovery
	Copper Sulfate	Chemical Recovery
	Wood Sugar	Byproduct Recovery
	Boric Acid	Waste Disposal
	Soft Drink Waste	Waste Disposal
	Seawater	Fresh Water Production
Heat Recovery	Caustic Extract	Chemical Recovery
	Brackish Water	Power Plant Make-Up

structured surfaces with special geometries prepared on the substrates have been developed recently for boiling. These surfaces have realized remarkable enhancements of pool boiling. However, no spray evaporation tests have been reported for most of them. As for those surfaces tested, many factors which may be influential to the heat transfer performance have never been investigated. Therefore, there is a need of a thorough exploration of the characteristics for the structured surfaces to assess their potential for spray film evaporator service.

II. LITERATURE REVIEW

A. Taxonomical Consideration of the Literature

1. Convection-enhancing vs. boiling-enhancing surfaces

The literature search reveals that the enhanced surfaces tested for falling-film evaporation fall into two main categories, convection enhancing and boiling enhancing, corresponding to the two major heat transfer mechanisms associated with falling-film evaporation. The convection enhancing surfaces usually improve non-boiling convective heat transfer by having large-scale (macroscopic) structures, such as ribs, grooves, or fins. The boiling enhancing surfaces promote nucleate or bubble boiling within the film flow by providing small-scale (microscopic) structures, such as a porous metallic matrix or miniature subsurface tunnels with periodic openings. A surface with macroscopic structure would have little influence other than the extended-surface effect on the heat transfer performance at large temperature differences when boiling is the dominant mode of heat transfer. A surface with microscopic structures would have little effect, other than that of a rough surface, at low temperature differences when flow convection is the dominant mode of heat transfer before the incipient boiling.

2. Vertical tubes or plates vs. horizontal tubes

In the case of plain surfaces, literature bearing the title of falling-film evaporation can deal with different situations: vertical tube, vertical plate, or horizontal tube. The cases of vertical tube and plate are considered identical as far as heat transfer is concerned. However, caution should be exercised to distinguish between these cases and horizontal tubes.

The local heat transfer coefficient distribution for an evaporating water film falling along a vertical tube was studied by Seban [3]. Data were obtained on a 0.31 m long heated section preceded by a 0.30 m adiabatic section for the development of flow and preheating by the surrounding vapor. High heat transfer coefficients near the entrance were evident, but there was a tendency for the coefficients to degrade toward constant values near the bottom of the tube. It is these asymptotic values of heat transfer coefficient on which the well-known correlation by Chun and Seban [4] is based. However, in the case of a horizontal tube, neither is there an adiabatic developing section available, nor is the film flow path long enough to reach the asymptotic value of the heat transfer coefficient. As a result, the Chun and Seban correlation tends to underestimate horizontal tube data.

Another distinction between the vertical and the horizontal tube is that the effect of liquid feed height is an issue for horizontal tubes but not for vertical tubes. The vertical distance between two consecutive tubes through which liquid falls before impacting the lower one has a significant effect on heat transfer data, as reported by Liu [5]. Greater feed height results in higher impact velocity and, consequently, higher heat transfer coefficient.

Although there are some important differences between the horizontal and vertical cases, there is a close relationship between the two. As a matter of fact, the development of the former has been strongly based on theory and experiment in the latter case. For example, as will be introduced later, the correlations proposed by Lorenz and Yung [6] and Owens [7] for a horizontal tube were based on works proposed for a vertical

tube or plate. The literature reviewed has been categorized according to the taxonomical considerations above. However, only studies dealing with falling film evaporation on horizontal tubes with plain or enhanced surfaces, either convection- or boiling-enhancing, are presented in Section II.B.

B. Summary of Previous Work

1. Falling film evaporation on a horizontal tube with plain surface

Individual tube performance within a bundle of tubes was reported by Cannizzaro et al. [8]. Heat transfer data were recorded for two 2.0-in. diameter commercial copper tubes installed in the central region of the third effect bundle of a horizontal tube multiple effect (HTME) test facility where brine-film was evaporated on the shell side and steam condensed on the tube side. The brine-side heat transfer coefficient based on the difference between the wall temperature and the saturation temperature of brine was reported to increase with brine saturation temperature. Change of heat flux caused no variation of the coefficients. Flow rates over the individual tubes were not measured. Based on Cannizzaro's data, Standiford [9] proposed the following correlation:

$$h = 0.05 \left(\frac{k^3 \rho^2 g}{\mu^2} \right)^{1/3} \left(\frac{8\rho \Gamma}{\mu D} \right)^{1/3} \quad (1)$$

Results were presented by Fletcher et al. [10] for an experimental investigation of an evaporating water film on a single horizontal tube. A 1.0-in. and a 2.0-in. diameter smooth 90/10 copper-nickel desalination tubes were tested. The data exhibited an increase in the heat transfer coefficient as the saturation temperature was increased; however, the

increase was much smaller than that reported by Cannizzaro et al. [8]. The data reported were also significantly lower than those reported by Cannizarro. The authors attributed the differences to the diverse properties of fresh water and sea water, the difference between a single tube and a tube bundle, and the differences in the feedwater distribution systems. It was concluded that the heat transfer is significantly influenced by the tube diameter, but not by the heat flux.

In their subsequent effort, Fletcher et al. [11] investigated the evaporation heat transfer of saturated sea water films on horizontal tubes. The data obtained are 50 percent higher than those for distilled water film, but still slightly lower than the sea water data for tubes located in a tube bundle reported by Cannizzaro et al. [8]. Heat transfer coefficients for the 1.0-in. diameter smooth tube were reported higher than those for the 2.0-in. diameter tube.

Parken [12] conducted an experimental and theoretical study which includes the effects of feedwater temperature, flowrate, cocurrent vapor shear, and heat flux on the boiling and non-boiling heat transfer coefficients. He observed an increase in the non-boiling evaporation coefficients with decreasing tube diameter, increasing flowrate, or increasing feedwater temperature. No effect of change in heat flux on the heat transfer coefficient was evident. The results obtained with vigorous nucleate boiling in the water film showed a remarkable effect of surface condition and aging on the heat transfer coefficient. A degradation in coefficient to approximately 30 percent of the initial value in seven hours was observed. The stabilized coefficients were found to be ten to forty percent higher than the corresponding non-boiling evaporation heat transfer

coefficients. Increases in tube diameter, saturation temperature, heat flux, or flowrate were each observed to increase the boiling coefficient. The non-boiling data were in excellent agreement with the results of a laminar analysis involving both an integral approach with a cubic polynomial velocity profile and a finite-difference scheme with a stagnation point boundary layer profile used to determine the film thickness and evaporation heat transfer coefficients. Only numerical data based on the analysis are available. Sernas [13] correlated Parken's non-boiling experimental data by the following expression for the 2.5 cm diameter tube:

$$\frac{\bar{h}}{k} \left(\frac{3\mu\Gamma}{gp^2} \right)^{1/3} = 0.01757 \left(\frac{4\Gamma}{\mu} \right)^{0.57} \left(\frac{v}{\alpha} \right)^{0.66} \quad (2)$$

For the 5 cm tube, the constant is 0.01578.

The dependence of heat transfer on the vertical spacing of the tubes (water feed height) was experimentally demonstrated by Liu [5]. It was found that in the ranges of test variables, the heat transfer coefficient was a function of only the water temperature and the vertical spacing of tubes. Attempts were made to predict the test results by solving the boundary layer flow equations of momentum, thermal energy, and turbulent kinetic energy using uniform initial profiles of velocity. Three-fourths of the free falling body velocity was arbitrarily taken for the initial velocity. The analysis showed an insensitivity of the heat transfer coefficients to changes of flow rate, heat flux, and tube diameter within the limited test range of variables. The prediction agreed with the test results in magnitude, variation of heat transfer coefficients, and the effects of feed height and fluid properties.

Owens [7] proposed the following correlations based on experimental data of Conti [14] and Liu [5] for non-boiling films, and data of Fletcher et al. [10] and Parken [12] for boiling films:

$$\text{Non-boiling} \quad \begin{cases} \text{Laminar} & \text{Nu} = 2.2(H/D)^{0.1} Re^{-1/3} \\ \text{Transition} & Re_{tr} = 1680 \text{ Pr}^{-1.5} \\ \text{Turbulent} & \text{Nu} = 0.185(H/D)^{0.1} \text{Pr}^{0.5} \end{cases} \quad (3)$$

$$\text{Boiling, Turbulent} \quad \text{Nu} = 0.0175(H/D)^{0.1} (q'')^{0.25} \text{Pr}^{0.5} \quad (4)$$

$$\text{Boiling, Turbulent} \quad \text{Nu} = 0.0175(H/D)^{0.1} (q'')^{0.25} \text{Pr}^{0.5} \quad (5)$$

$$\text{Boiling, Turbulent} \quad \text{Nu} = 0.0175(H/D)^{0.1} (q'')^{0.25} \text{Pr}^{0.5} \quad (6)$$

where the heat flux q'' is in kW/m^2 . The exponent of H/D was tentatively determined as 0.1 due to insufficient data. The expression for the boiling film has the same form as that of the non-boiling case except for the heat flux dependence.

A simple model of combined evaporation and boiling of liquid films on horizontal tubes was developed by Lorenz and Yung [6]. Within the length of contact, which is a half of the tube circumference, two distinct convective heat transfer regions were defined: a thermal developing region and a fully developed region. In the thermal developing region, the film is superheated from the saturation temperature to a fully developed linear profile, while all of the heat transferred from the wall goes into superheating the liquid film and no evaporation occurs. The developing length was estimated using Nusselt's [15] expression for film thickness together with an approximate integral method. In the fully developed region, all of the heat transferred goes to evaporation at the liquid/vapor interface. The correlation developed by Chun and Seban [4] for heat transfer of evaporating liquid films on vertical tubes was employed for the fully developed region. The average heat transfer coefficient over the entire length of contact is

$$\bar{h} = h_d \frac{L_d}{L} + h_c \left(1 - \frac{L_d}{L}\right) + h_{NB} \quad (7)$$

where the quantities (L_d/L) and $(1 - L_d/L)$ weight the respective convective heat transfer components according to the length over which each is effective. The pool boiling correlation by Rohsenow [14] was suggested to estimate h_{NB} . Boiling was assumed to occur over the entire length and therefore the weighting factor for h_{NB} is unity. Predictions based on this model were shown to agree favorably with experiment data.

As noted above, among those predictions reported, correlations proposed by Standiford [9], Sernas [13], and Owens [7] are all based on experimental data. Numerical approaches were made by Parken [12] and Liu [5]. Lorenz and Yung's [6] model includes an analytical solution for the thermal developing region; however, the developing heat transfer coefficient was estimated by assuming thermal development was reached in a too short distance. Besides, the empirical correlation by Chun and Seban [4] for a vertical surface instead of a horizontal tube was used for the fully developed region. A mathematical model of the fully developed film evaporation process based on Nusselt's [15] film condensation work was proposed by Sabin and Poppendiek [16]. A similar attempt was made by Nakazatomi and Bergles [17]. However, mathematical errors were found in both of the works. Therefore, it is worthwhile to resolve the problem through an analytical approach and to compare the result with experimental data and those predictions reported.

2. Falling-film evaporation on horizontal tubes with enhanced surfaces

The literature reviewed pertinent to the enhanced surfaces is summarized in Table 2. The method of surface modification, surface

Table 2. Summary of investigations of thin film evaporation on horizontal tubes with enhanced surfaces^a

Part I. Convection-Enhancing Surfaces

Method of Surface Modification	Surface Description	Investigation
Machining	Circumferentially grooved by cutting American Standard threads on aluminum-alloy tubes; 8 and 28 threads per inch; geometrical ratio of extended surface 2:1.	Conti [18] 1978
Machining	Brass tubing cut with 10 or 16 American standard threads per inch.	Schultz et al. [19] 1977
Machining	Straight-edged circumferential grooves on circular and elliptical aluminum tubes.	Moalem-Maron et al. [20] 1978
Forming	Knurled.	Cox [21] 1970 Newson [22] 1976

^aHeat transfer coefficients in this table are based on the base area, unless specified otherwise.

General Considerations	Results Reported
51mm(2 in.) OD tube, electrically heated; ammonia; Re: 32-3200, 22°C(72°F), 919.8 kPa (133.4 psia), $q'': 11 \text{ kW/m}^2$.	Enhancement factor about 1.75 beyond the geometrical area extension, total improvement about 3.5 compared with smooth tube; performance more dependent on flow rate than smooth tube.
3/4 in. OD tube, electrically heated; water; single tube and bundle.	Thread-side heat transfer coefficient highly sensitive to superheat. No smooth tube data compared.
Water on shell side; steam on tube side.	Heat transfer characteristics, flow regimes and heat transfer coefficients predicted; small-sized grooves show marked improvement over the large ones; 100% enhancement with $1 \times 1 \times 1 \text{ mm}$ grooves obtained.
2 in. OD tube bundle, 3.4 in. triangular pitch; HTME distillation, saline water shell side, steam tube side; $q'': 31600-66300 \text{ W/m}^2$.	Evaporation side coefficient increases by 40-70% in excess of smooth tube value; bubbles grow larger due to slower movement on knurled surface; h decreases at higher wall temperature than smooth tubes, when bubbles become too small to contact an adjacent tube.

Table 2. (Continued)

Method of Surface Modification	Surface Description	Investigation
Forming	Knurled. 90/10 Cu-Ni tube.	Fletcher et al. [11] 1975
Forming	Circumferentially rolled-in grooves on copper nickel tubes, 60% land and 40% grooves.	Prince [23] 1971
Forming	Straight knurled, grooves pressed axially, 0.020 in. wide, 0.010 in. deep, 0.030 in. in pitch; surface area increased 40%.	Sabin and Poppendiek [16] 1978
Forming	Diamond knurled, grooves lie at about a 40 degree angle to tube axis, 0.015 in. wide, 0.006 in. deep; surface area increases 20%.	Sabin and Poppendiek [16] 1978
Not stated, machining or forming	Circumferential triangular grooves on copper or titanium tubes.	Edwards et al. [24] 1973

General Considerations	Results Reported
2.0 in. OD tube, electrically heated; sea water, 93°C (200°F) Γ : $0.3347 - 0.3742 \text{ kg/s-m}$.	Evaporation heat transfer coefficient lower than that of smooth tube; nucleation evident.
1.0 in. OD tube bundle; water evaporating on shell side, steam condensing on tube side; evaporation temperature: $100-116^{\circ}\text{C}$; $q": 15,000-80,000 \text{ W/m}^2$.	150% improvement in overall heat transfer coefficient.
1 in. OD tube, electrical- ly heated; ammonia, $13-24^{\circ}\text{C}$, $\Gamma: 5.6 \times 10^{-3} - 5.6 \times 10^{-3} \text{ kg/s-m}$; $q": 3155-25240 \text{ W/m}^2$.	Good wettability; liquid film flow impeded and film thickened; h close to smooth tube value despite the increased surface area.
1 in. OD tube, electrical- ly heated; ammonia, $13-24^{\circ}\text{C}$, $\Gamma: 5.6 \times 10^{-4} - 5.6 \times 10^{-3} \text{ kg/s-m}$; $q": 3155-25240 \text{ W/m}^2$.	Good wettability; h about twice as high as that of smooth tube.
1 in. OD tube bundle, water.	Model developed, computational result presented, 500% enhancement possible, no experimental results compared; copper gives groove side coefficient four times greater than titanium; finer grooves give better performance if not flooded; no nucleation.

Table 2. (Continued)

Method of Surface Modification	Surface Description	Investigation
Not stated, machining or forming	Tube with longitudinal ribs.	Newson [22, 25] 1976, 1978
Not stated, machining or forming	Circumferential square-edged grooves with straight, cut-edged or circular bottoms; triangular grooves; circular-bottom grooves; all 0.8 mm groove depth, on aluminum tubes.	Sideman and Levin [26] 1979
Not stated, extended or drawn	Elliptical, parabolic, and hyperbolic-shape smooth tubes.	Sideman et al. [27, 28, 29] 1975, 1977, 1979 Semiat et al. [30] 1978

General Considerations	Results Reported
Suggested profile for enhancing non-boiling evaporation coefficient.	Mechanism discussed; 250% improvement in heat transfer coefficient over smooth surface attainable by an inclined plate with optimal geometry.
Analysis restricted to vertical plate, laminar film, effect of waves neglected; water, 60°C.	Square-edged grooves with either straight or cut-edged bottoms are best for $Re > 1000$; circular-bottom-square-edge grooves for $250 < Re < 1000$; triangular grooves good for $50 < Re < 250$.
Deionized water on shell side, steam on tube side.	20% increase in overall heat transfer coefficient for elliptic-shape tube with vertical to horizontal axis ratio greater than 4; parabolic and hyperbolic-shape tubes give lower values than corresponding circular tubes; experimental data for elliptic-shape tube only; no nucleation.

Table 2. (Continued)

Part II. Boiling-Enhancing Surfaces

Method of Surface Modification	Surface Description	Investigation
Coating	Stainless-steel High Flux porous matrix coated on standard stainless-steel tube.	Conti [18] 1978
Coating	Aluminum tube coated with High Flux porous matrix.	Czikk et al. [2] 1978
Coating	Iron High Flux porous matrix of 0.010 in. (0.025 cm) thick, coated on a steel tube.	Sabin and Poppendiek [16] 1978
Coating	Titanium tube coated with High Flux porous matrix.	Hillis et al. [31] 1979

General Considerations	Results Reported
5 cm (2 in.) OD tube, electrically heated; ammonia, Re: 32-3200, 22°C (72°F); 919.8 kPa (133.4 psia); q'' : 11 kW/m ² .	Temperature difference decreases monotonically during a start-up period of several hours; enhancement factor of about 3 obtained; performance rather independent upon Γ .
1 in. OD tube bundle, triangular 1.5 in. pitch layout electrically heated; ammonia, Γ : 0.0344 - 0.0900 kg/s-m (91-238 lbm/hr ft); q'' : 1100-35000 W/m ² (3600-11000 B/hr-ft ²); 1-1/2 in. OD single tube spray, ammonia Γ =0.0278 kg/s-m; q'' : 11600-25230 W/m ² (3679-8000 B/hr-ft ²).	General agreement among the spray tube bundle, the single tube spray, and pool boiling data observed; typical superheat of 0.47°C (0.86°F) at $q''=15800$ W/m ² (5000 B/hr-ft ²); distinct nucleation and excellent wetting observed.
1 in. OD tube, electrically heated; ammonia, 13-24°C, Γ : 5.6×10^{-4} - 5.6×10^{-3} kg/s-m; q'' : 3155-25240 W/m ² .	Good wettability; h about twice as high as smooth tube.
Sprayed-bundle evaporator with 388 tubes of 1.5 in. OD; sea water on tube side, ammonia on shell side.	Heat transfer coefficient independent on heat transfer rate, ammonia temperature and feed rate; nucleation sites deactivated by ammonia can be reactivated by drying out.

Table 2. (Continued)

Method of Surface Modification	Surface Description	Investigation
Coating	Titanium tube coated with High Flux porous matrix.	Lorenz et al. [32] 1981
Coating	Plating a steel tube with nickel at very high current, to form porous nickel coating with sharp roughness elements a few thousandths of an inch high.	Sabin and Poppendiek [16] 1978
Machining and forming	Portion of the ridge of a fine thread rolled over, and striped longitudinally to form cavities on the tube.	Sabin and Poppendiek [16] 1978

General Considerations	Results Reported
Sprayed-bundle evaporator with 6304 tubes of 1.0 in. OD; sea water on tube side, ammonia on shell side.	Poor performance due to fouling of the porous surface.
1 in. OD tube, electrical-ly heated; \dot{m} ammonia, $13-24^{\circ}\text{C}$, $\Gamma: 5.6 \times 10^{-4} - 5.6 \times 10^{-3}$ kg/s-m; $q'': 3155-25240 \text{ W/m}^2$.	Good wettability; about 50% improvement in h.
1 in. OD tube, electrical-ly heated; \dot{m} ammonia, $13-24^{\circ}\text{C}$, $\Gamma: 5.6 \times 10^{-4} - 5.6 \times 10^{-3}$ kg/s-m; $q'': 3155-25240 \text{ W/m}^2$.	Poor performance attributed to vapor trapped in cavities, which kept liquid from contacting heated surface.

geometry, reference, test condition and result for each investigation are noted. There is much more literature on the convection-enhancing surfaces than the boiling-enhancing surfaces. Grooved and knurled surfaces are the two major groups of the convection-enhancing surfaces. The large-scale structures enhance the non-boiling convective heat transfer. A maximum enhancement in heat transfer coefficient of 250 percent over the smooth surface was reported. Most of the studies done for the boiling-enhancing surfaces were for the porous surfaces. The porous surfaces promote nucleate boiling by providing small-scale structures to facilitate the generation of vapor phase. Performances from poorer to three times as good as a smooth tube were reported.

The literature survey shows some variables that are known to be influential in falling film evaporation on plain surface, as shown in the literature review in Section II-B-1, have not been investigated for the enhanced surfaces. As introduced below, there are some commercial structured surfaces which have never been tested in spray evaporators. Therefore, there is a need for thorough studies of falling film evaporation on additional structured surfaces.

3. Structured heat transfer surfaces

Special surface geometries that promote high-performance nucleate boiling have been developed based on the understanding of the character of nucleation sites, the shape necessary to form stable vapor traps, and the conditions necessary for thin film evaporation in porous structures. The first of them was patented in 1968, and by 1980 six nucleate boiling surface geometries were commercially available [33].

Among the three best known commercial surfaces is GEWA-T manufactured

by Wieland-Werke AG, Ulm, F. R. Germany. The surface has circumferential reentrant grooves which are formed by properly flattening the tips of spiral fins of an integral fin tube to restrict the mouth of the space between two fins, as shown in Fig. 2 [34]. The details of manufacturing are described in the patent [35]. Single-tube pool boiling tests in different liquids have been conducted [36,37,38]. A maximum of 5.3 times the heat transfer coefficient of the plain tube was reported. Boiling heat transfer from a simulated bundle of GEWA-T tubes electrically heated and flooded with refrigerant was investigated by Stephan and Mitrovic [39,40]. Heat transfer coefficients three times those for smooth tubes were reported. In addition to the effect of extended surface, the improvement in boiling heat transfer was considered to be caused by the sweeping-off motion of the bubbles moving in the reentrant channels. The path which a single bubble travels in the channel is longer than the contact length around a low-fin tube because of the restricted opening. Bubbles still growing on the wall inside the channel are swept-off by large bubbles. This increases the frequency of bubble generation, as well as heat transfer coefficient. At higher heat flux, the vapor volume in the channel is so large that a continuous vapor stream core is formed, with a thin liquid film evaporating on the wall. The liquid film is partially dried out at even higher heat flux, causing a drop in heat transfer coefficient where vapor is in contact with the surface. This interpretation is quite speculative since even external observation of the heated tubes was quite difficult.

The "Thermoexcel-E" surface by Hitachi (Japan) has minute, parallel tunnels with tiny holes communicating with the outside located at regular

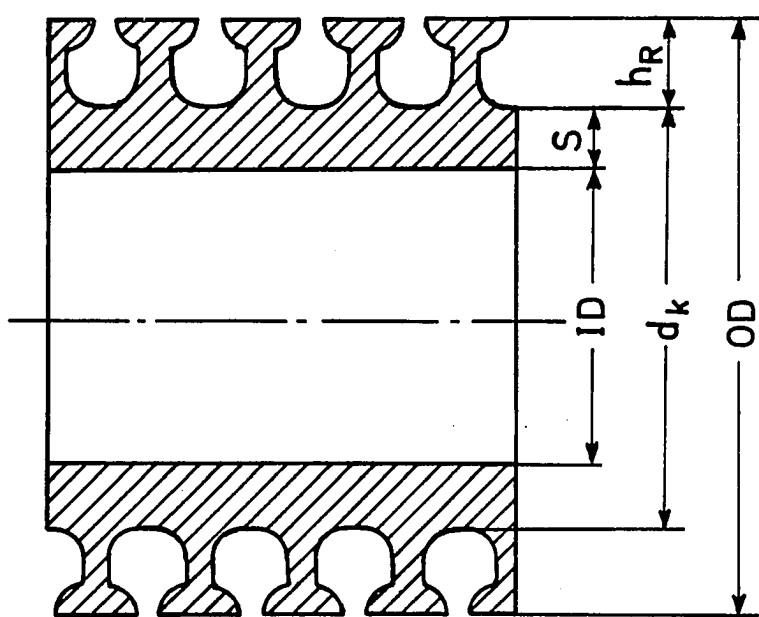
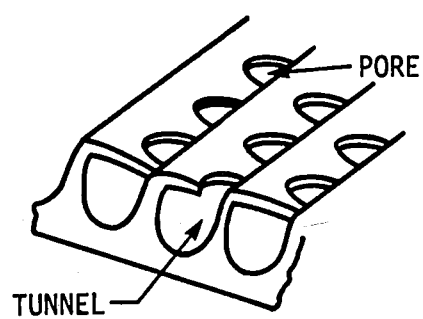


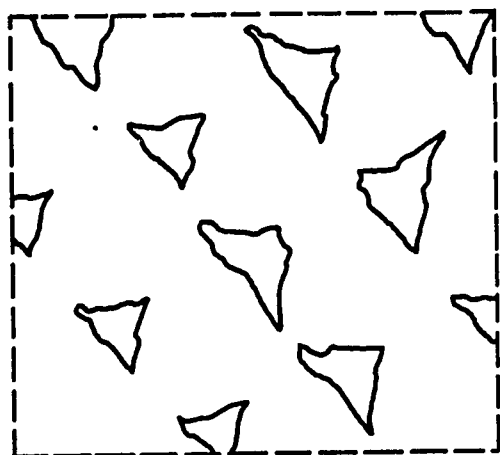
Fig. 2. Cross section of a GEWA-T tube (exaggerated)

intervals. Thus, interconnected reentrant pores of uniform size are evenly distributed on the surface, as shown in Fig. 3. The manufacturing operations include forming helical, interrupted fins on the surface, and bending down the upper parts of the fins through high-speed brushing to close the grooves between the neighboring fins [40]. Pool boiling tests on the Thermoexcel-E surface have been conducted for different liquids [36,42-45]. Improvements in heat transfer of five to ten times above the plain tube were reported. Thin film evaporation of liquid inside the minute, but large surface area tunnels is believed to be the major mechanism of heat transfer [44,46-48]. Vapor generated is ejected from the pores in the form of bubbles, and liquid is sucked into the tunnels to replenish the evaporated liquid. The heat transfer coefficient drops when the heat flux is so high that the internal surface dries out. Falling film evaporation of R-11 was tested on a vertical Thermoexcel-E surface [49]. Active nucleation was always evident. The heat transfer coefficient was nearly independent of superheat and flow rate. The coefficients of falling film evaporation show higher values at low heat flux, and coincide with pool boiling at high heat flux.

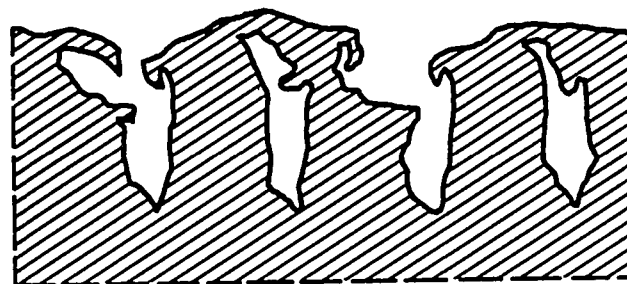
Nucleate boiling enhancement by the use of porous metal coatings has been realized by the surfaces commercialized by Union Carbide Corporation in the United States under the name High Flux. Typically, the porous coating is composed of metal particles that are bonded to each other and the substrate by brazing or sintering, as described in detail in the patent [50]. There are several additional patents on High Flux. Figure 4 [51] shows the cross-sectional view of the porous structure, where numerous reentrant cavities are provided to increase the probability of vapor



(a) IDEALIZED VIEW



(b) TOP VIEW



(c) ACTUAL CROSS-SECTION VIEW

Fig. 3. Geometry of the Thermoexcel-E surface

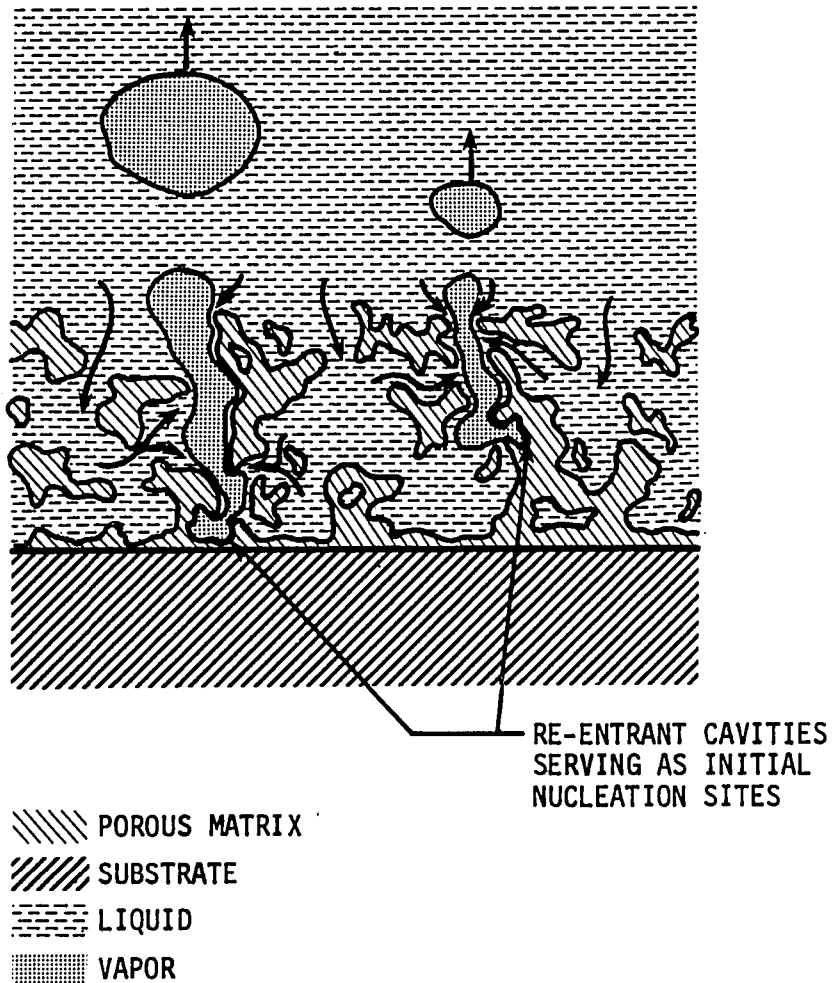


Fig. 4. Conceptual model of boiling in a porous matrix of sintered metallic particles

trapping. The size of reentrant cavities is controlled by the size of the initial particles that make up the surface. Boiling performance can be optimized by controlling the pore size distribution. Performance and characteristics of porous boiling surface have been investigated [36,38,51-55]. Typically, a factor of increase of about ten in heat transfer coefficients is evident. In addition to greatly enhanced heat transfer, boiling curve hysteresis was observed with both moderately and highly wetting liquids. Several mechanisms have been postulated for boiling from porous surfaces [56]. In a plausible model, steady vapor generation in a porous matrix is considered to be primarily internal [51]. Vapor escapes through preferential chimneys; the liquid is supplied primarily through other channels surrounding the vapor chimneys. Preheating of the liquid and evaporation takes place on the internal surface of the vapor chimney wetted by the liquid. The high nucleate boiling coefficients attained are due to the large internal surface area and small liquid film temperature difference between solid and vapor. While the actual heat transfer process is dynamic in nature, a relatively simple static model was developed, in which the total temperature difference is composed of the nucleation superheat required to expand bubbles against surface tension and the temperature difference across the liquid film [54]. Pore size distribution and shape factors need to be determined before the heat flux can be estimated.

The three special surfaces introduced above have received much interest due to potential energy, materials, and cost savings considerations. However, the preceding literature survey as summarized in Table 2, Part II shows that only the High Flux surface has been utilized

for spray evaporators. Yet, some variables which are known to be influential in falling film evaporation on plain surface such as flow rate and liquid feed height have not been closely investigated. As for the GEWA-T and Thermoexcel-E surfaces, no work on horizontal tube spray evaporation has been reported.

C. Objectives of Research

The literature survey in section II-B-1 shows even though some correlations based on experimental data are available, no complete analytical solution to the falling film evaporation on a horizontal smooth tube has ever been reported. As for the structured surfaces, the literature survey in section II-B-2 reveals that there is a need for thorough studies of falling film evaporation on all the commercial special surfaces. The objectives of the present study are therefore (a) to develop a model for falling film evaporation on a horizontal smooth tube, which includes analytical solutions for the thermal developing and fully developed regions. The jet impingement effect at the apex of the tube will also be taken into account. The result will be compared with experimental data and correlations reported. (b) to explore the performances of a variety of enhanced boiling surfaces to assess their potential for spray-film evaporator service. Variables which might affect either convection or nucleate boiling heat transfer will be investigated. Water is the selected working fluid based on the use of spray film evaporation in desalination.

III. ANALYSIS OF FALLING FILM EVAPORATION
ON A HORIZONTAL TUBE

A. Introduction

As noted in the preceding chapter, no complete analytical work has been reported to predict heat transfer of falling film evaporation on a horizontal tube. Lorenz and Yung [6] used the correlation by Chun and Seban [4] to estimate the heat transfer coefficient in the fully developed region in their semi-analytical model for falling film evaporation. However, the correlation by Chun and Seban was based on falling film evaporation data on a vertical surface instead of a horizontal tube. Besides, the developing heat transfer coefficient in the Lorenz and Yung model was estimated by assuming thermal development reached in a distance too short. (See eq. (19).) Nusselt [15] (1916) was the first who analyzed laminar film flow on a horizontal tube; however only the result of film condensation was presented. The developed film evaporation coefficient on a horizontal tube can be calculated by solving Nusselt's problem for film evaporation. This has been tried by Sabin and Poppdiek [16] and Nakazatomi and Bergles [17]. However, as explained later, mathematical errors were found in both works. The effect of thermal entrance region was not considered at all. The present model is unique in its complete analytical solutions for the thermal developing and the fully developed regions and taking the effect of the jet impingement at the apex of the tube into account.

The present model describes heat transfer in three distinct regions, the jet impingement region, the thermal developing region and the fully developed region. When a thin film flow on the tube surface is established

by feeding liquid at saturation temperature to the top of a horizontal tube, as shown in Fig. 5, there is a short region at the top where the heat transfer coefficient is particularly high due to impingement of the liquid to the surface. A subsequent thermal developing region is required for the film flow to be superheated from the uniform saturation temperature to a fully developed linear profile. There is negligible latent heat transfer in this region because most of the heat transfer goes to superheat the liquid film. A fully developed region characterized by the linear temperature profile and evaporation at the free surface of the film immediately follows the thermal developing region until near the bottom of the tube where the liquid drains from the tube.

B. Jet Impingement Region

Since the film thickness is much smaller than the tube radius, the situation at the top of the horizontal tube may be considered as a two-dimensional liquid jet impinging on a flat plate. Heat transfer for a plane liquid jet striking a surface generating uniform heat flux has been studied by McMurray et al. [57] and Miyasaka and Inada [58]. It was found that the flow field can be divided into three zones, stagnation flow zone, impingement flow zone, and uniform parallel flow zone. As shown in Fig. 6 [58], the stagnation flow zone is characterized by the velocity just outside the hydrodynamic boundary layer, u_{\max} , linearly proportional to the distance from the stagnation point, x . The local heat transfer coefficient data can be correlated by the following equation:

$$h_s = 1.03 \text{ Pr}^{1/3} \cdot k \left[\frac{d(u_{\max}/u_j)}{d(x/w)} \right] \cdot \frac{u_j}{v_w}^{0.5} \quad (8)$$

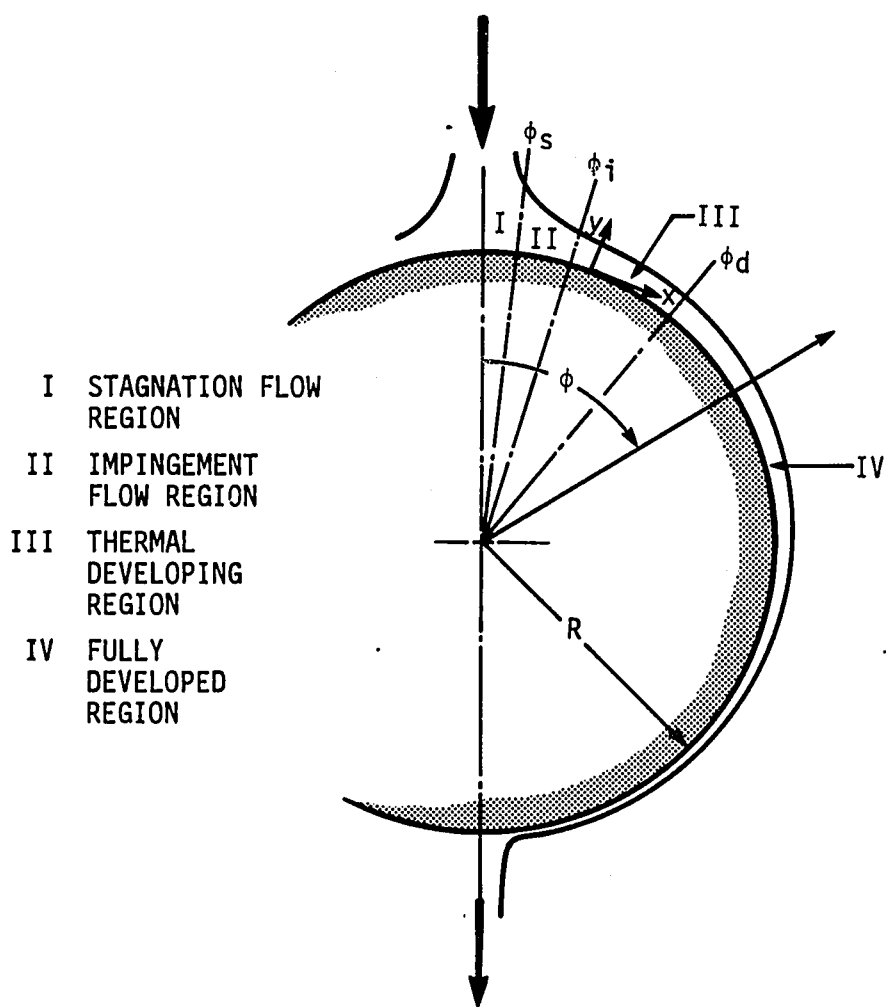


Fig. 5. Model for falling film evaporation on a horizontal tube

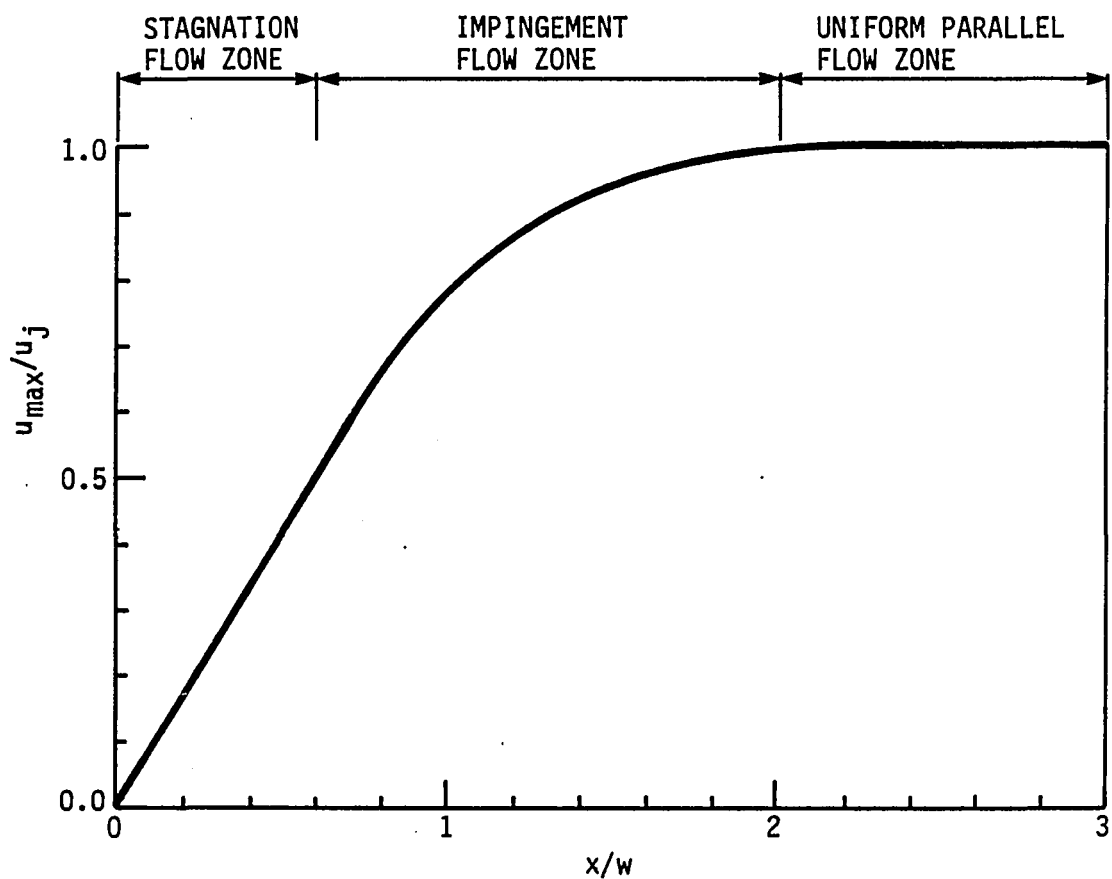


Fig. 6. Distribution of velocity just outside the hydrodynamic boundary layer in the jet impingement region

Since the velocity gradient is constant in the stagnation flow zone, this is also the equation for the average heat transfer coefficient, \bar{h}_s . The jet velocity u_j , for the case of a spray film evaporator is that of a free falling body, $\sqrt{2gH}$, where H is the liquid feed height. The jet width, w , is calculated based on the conservation of mass, i.e., $w = 2\Gamma_i/u_j\rho$. The stagnation flow zone covers the region of $0 < \frac{x}{w} < 0.6$; therefore, the angle

$$\phi_s = 0.6 \left(\frac{w}{R} \right) \quad (9)$$

is taken as the angular position at the end of the stagnation flow zone.

The impingement flow zone covers the range of $0.5 < u_{max}/u_j < 1.0$.

The local heat transfer data can be correlated by the following equations [58]:

$$Nu_i = \frac{h_i x}{k} = 0.73 Pr^{1/3} Re_x^{0.5} \quad (10)$$

for a laminar boundary layer, and

$$Nu_i = \frac{h_i x}{k} = 0.037 Pr^{1/3} Re_x^{0.8} \quad (11)$$

for a turbulent boundary layer. Note that the local Reynolds number, Re_x , is based on the local velocity just outside the boundary layer, $u_{max}(x)$.

$$Re_x = \frac{x u_{max}(x)}{v} \quad (12)$$

The hydrodynamic boundary layer is laminar from the stagnation point to some critical Reynolds number at which point a transition to turbulent boundary layer begins. According to the data reported by McMurray et al.

[57], the critical Reynolds number, Re_c , is about 4.5×10^5 . The average heat transfer coefficient in the impingement flow zone, \bar{h}_i , can be calculated numerically based on the local u_{max} data given in Fig. 6. The impingement flow zone covers the range of $0.6 < \frac{x}{w} < 2.0$. Therefore the angle

$$\phi_i = 2.0 \left(\frac{w}{R} \right) \quad (13)$$

is taken as the angular position at the end of the impingement flow zone.

The uniform parallel flow zone characterizes film-flow forced convection along a flat plate. As shown in Fig. 6, hydrodynamic development is reached at the entrance of this region. However, in the case of falling film evaporation on a horizontal tube, the velocity and film thickness change along the tube wall. In addition, there is evaporation at the outer surface of the film. Therefore, the result for the uniform parallel film flow on a flat plate cannot be adopted in the present model. A different approach is presented in the next section.

C. Thermal Developing Region

The model is developed based on the following assumptions for both the thermally developing and developed regions:

- (a) the entire tube surface is covered with liquid film, i.e., perfect wetting condition
- (b) the film flow is laminar
- (c) the film flow is steady
- (d) the film thickness is small compared to the tube diameter
- (e) there is no nucleate boiling within the film

- (f) heat transfer is only by conduction across a liquid layer
- (g) evaporation occurs on the liquid-vapor interface where the temperature is at saturation
- (h) the wall temperature is uniform
- (i) the drag on the liquid-vapor interface is negligible
- (j) the fluid properties are constant
- (k) the surface tension effect is negligible

Based on the previous discussion, hydrodynamic development is reached at the end of the jet impingement region. The fully developed velocity distribution in a liquid film flowing over a horizontal plane tube can be obtained by considering a force balance on an element of film, along with the no-slip boundary condition, $u = 0$ at $y = 0$:

$$u(y, \phi) = \frac{g(\rho_f - \rho_g) \sin \phi}{\mu} (y\delta - \frac{y^2}{2}) \quad (14)$$

and the mean velocity is obtained by integrating u across the film:

$$\bar{u}(\phi) = \frac{g(\rho_f - \rho_g)(\sin \phi)\delta^2}{3\mu} \quad (15)$$

with the film thickness

$$\delta(\phi) = [\frac{3\mu\Gamma(\phi)}{g\rho_f(\rho_f - \rho_g)\sin\phi}]^{1/3} \quad (16)$$

where Γ is the film flow rate per unit length of tube. The above relations are valid in both thermally developing and developed regions.

In the thermal developing region, heat from the heating surface is transferred to superheat the film flow. There is latent heat

transport; however, most of the heat goes to superheating the film. Therefore, the film flow rate can be assumed constant. By assuming negligible convection and a very thin film compared to the tube diameter, to an observer moving with the average film velocity, the change of temperature profile in the developing region can be obtained by solving a one-dimensional transient heat conduction problem in cartesian coordinates as shown below:

$$\frac{\partial T}{\partial \tau} = \alpha \frac{\partial^2 T}{\partial y^2} \quad (17)$$

with the initial condition

$$T(0, y) = T_s, \quad 0 < y \leq \delta$$

and the boundary conditions

$$T(\tau, 0) = T_w, \quad \tau \geq 0$$

$$T(\tau, \delta) = T_s, \quad \tau \geq 0$$

As depicted by the initial and boundary conditions, it is assumed that the film is at uniform saturation temperature at the beginning, and constant temperature at the wall and saturation temperature at the outside surface all the way. This problem has a non-homogeneous boundary condition at $y = 0$. The solution can be obtained by converting the non-homogeneous problem into a homogeneous one by the use of a partial solution to the non-homogeneous problem. The problem can also be solved by the Laplace transformation method. The solution is given as [59]

$$\frac{T(\tau, y) - T_s}{T_w - T_s} = 1 - \frac{y}{\delta} - \frac{2}{\pi} \sum_{n=1}^{\infty} \frac{\sin n\pi(\frac{y}{\delta})}{n \cdot \exp(\frac{n^2 \pi^2 \alpha \tau}{\delta^2})} \quad (18)$$

It is observed that the solution is composed of the steady-state solution and a transient term in the form of infinite series. The temperature profile becomes more and more linear with time. However, theoretically it takes an infinitely long time for the linear temperature profile to develop. The temperature profile in the thermal developing film is plotted in Fig. 7. It is shown that the temperature profile is very close to linear for $\tau > \delta^2/\pi\alpha$. Therefore, the approximate time required for the steady-state temperature profile to develop is taken as

$$\tau_d = \frac{\delta^2}{\pi\alpha} \quad (19)$$

Lorenz and Yung [6] took $\tau_d = \delta^2/4\pi\alpha$. Apparently, the temperature profile is far away from linear at that value of τ_d . The angular position at the end of the thermal developing region, ϕ_d , can be calculated by integrating the reciprocal of the mean film velocity,

$$\int_{\phi_i}^{\phi_d} \frac{d\phi}{\bar{u}(\phi)} = \int_0^{\tau_d} \frac{d\tau}{R} \quad (20)$$

where ϕ_i is the angular position at the end of the impingement flow region and the beginning of the thermal developing region. By substituting eqs. (15) and (19) for $\bar{u}(\phi)$ and τ_d , eq. (20) yields the following implicit equation for the angular position at the end of the thermal developing region, ϕ_d :

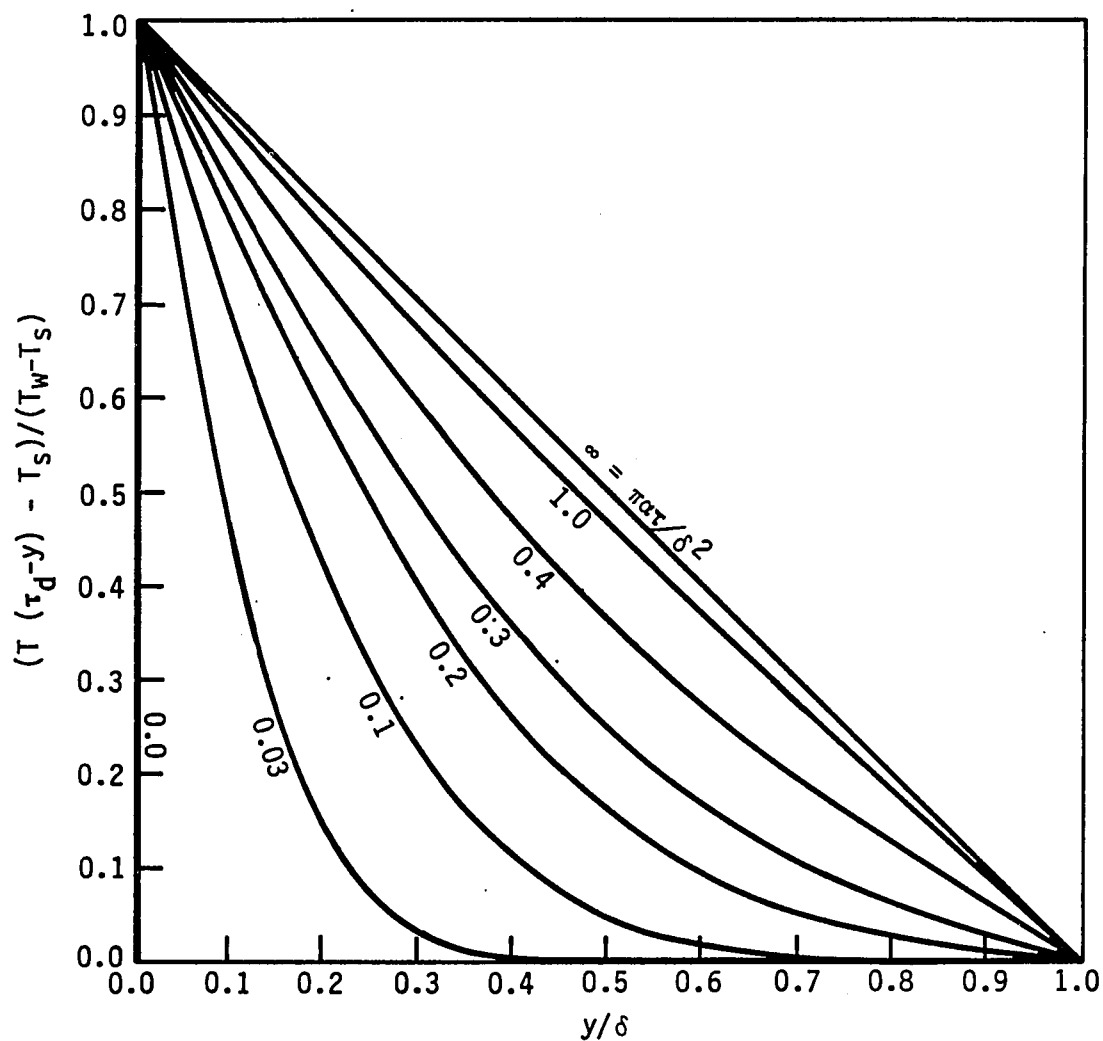


Fig. 7. Progress of temperature profile in the thermal developing region

$$\left(\int_{\phi_i}^{\phi_d} \sin^{-1/3} \phi d\phi \right) \sin^{2/3} \phi_d = \frac{1}{\pi \alpha R} \left(\frac{3\mu \Gamma^4}{g \rho_f^5} \right)^{1/3} \quad (21)$$

The left side of the equation can be evaluated numerically, and the curves of ϕ_d for different values of ϕ_i are plotted in Fig. 8. The average heat transfer rate in the developing region is evaluated by integrating the local heat transfer rate at the heated wall:

$$\overline{q''_d} = \frac{1}{\tau_d} \int_0^{\tau_d} \left(-k \frac{\partial T(\tau, y)}{\partial y} \Big|_{y=0} \right) d\tau \quad (22)$$

By substituting eq. (18) for $T(\tau, y)$ and eq. (19) for τ_d , the average heat transfer rate can be expressed as

$$\begin{aligned} \overline{q''_d} &= k(T_w - T_s) \left[\frac{g \rho_f (\rho_f - \rho_g)}{3\mu \Gamma_i} \right]^{1/3} \left[1 - \frac{2}{\pi} \sum_{n=1}^{\infty} \frac{1}{n^2} \left(\frac{1}{\exp(n^2 \pi)} - 1 \right) \right] \\ &= 2.020k(T_w - T_s) \left[\frac{g \rho_f (\rho_f - \rho_g)}{3\mu \Gamma_i} \right]^{1/3} \end{aligned} \quad (23)$$

The above equation was developed by assuming a constant film thickness, δ . Judging from eq. (16), δ is a weak function of ϕ . As shown in Fig. 9, δ is nearly constant with respect to ϕ except in the regions close to the top and the bottom stagnation points. The thermal developing region is quite unlikely to reach close to the bottom stagnation point in most cases; in other words, ϕ_d is always considerably smaller than π . At the entrance of thermal developing region, although δ may be large, the thermal boundary layer is much smaller than δ . The thick hydrodynamic layer actually does not significantly affect the slow heat diffusion near the wall. The thermal development is always reached when δ is very close to that at

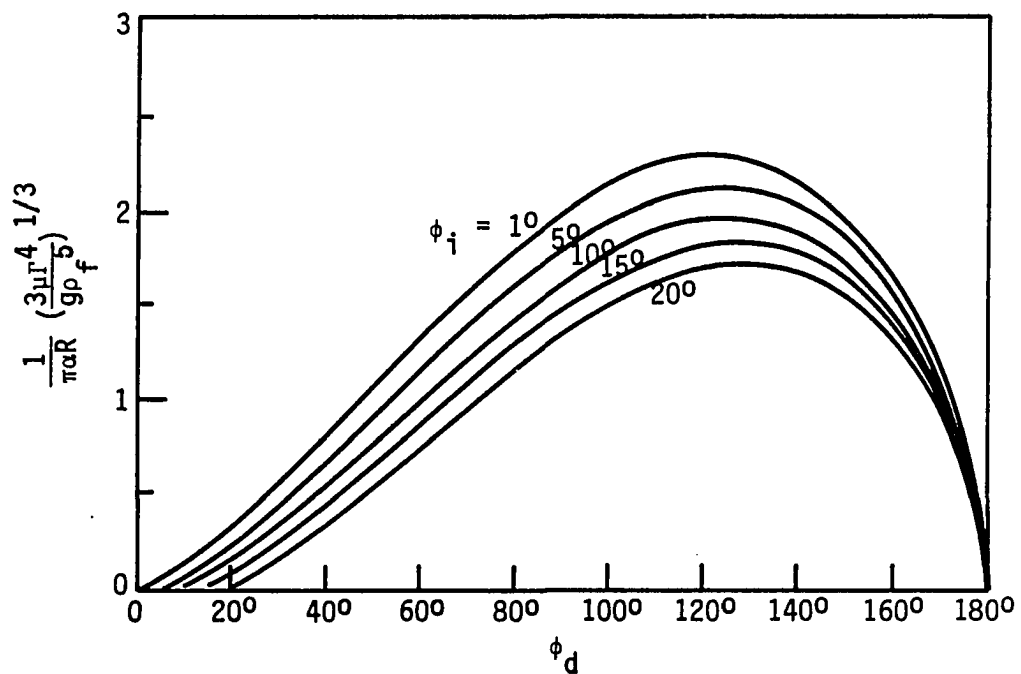


Fig. 8. Angular position at the end of the thermal developing region

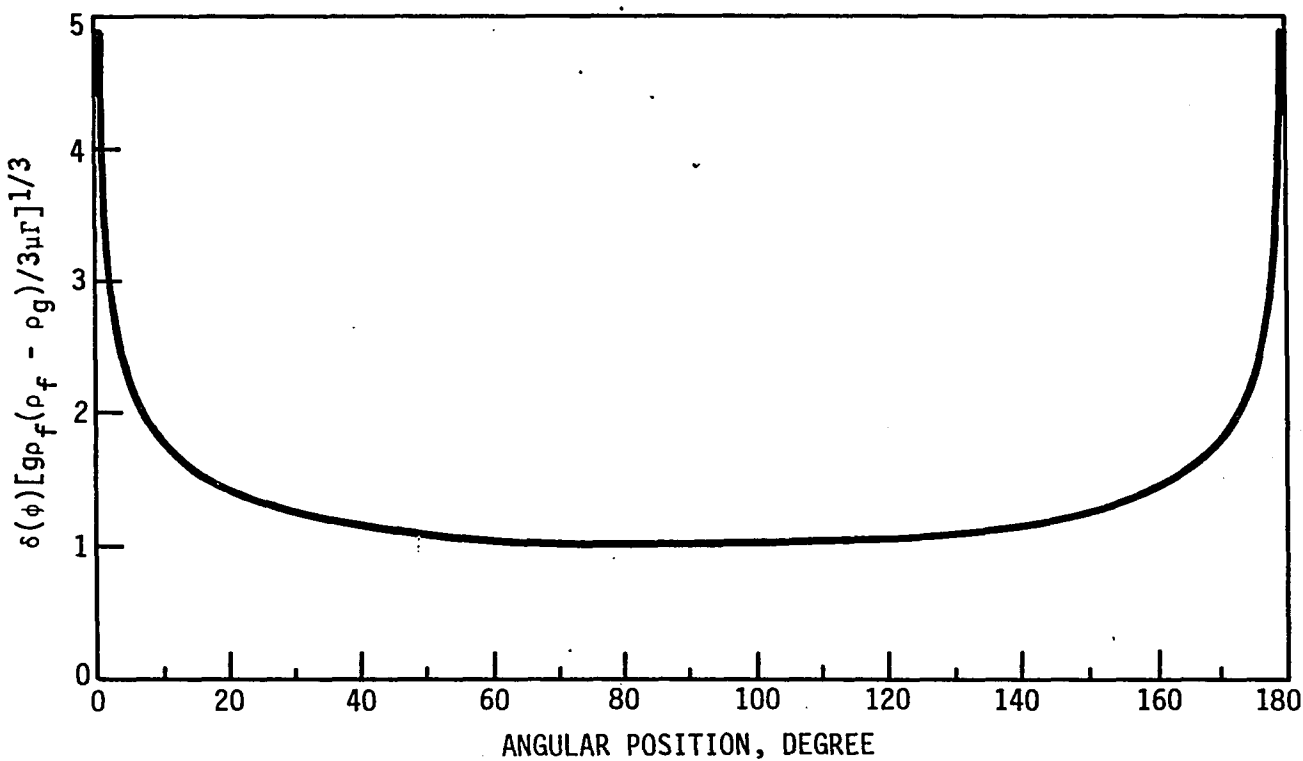


Fig. 9. Variation of film thickness with respect to angular position

$\phi = \pi/2$. Therefore, the constant δ at $\phi = \pi/2$ was used to develop the expression for \bar{q}_d'' . Based on eq. (23), the mean heat transfer coefficient in the thermal developing region is

$$\bar{h}_d = 2.020k \left[\frac{g\rho_f(\rho_f - \rho_g)}{3\mu R_i} \right]^{1/3} \quad (24)$$

D. Fully Developed Region

In the fully developed region, a linear temperature profile is assumed throughout. Heat is conducted across the film, and evaporation takes place at the film free surface. Since conduction heat transfer across the film equals the latent heat of vaporization,

$$- h_{fg} \cdot d\Gamma = k_f \left(\frac{T_w - T_s}{\delta} \right) R d\phi \quad (25)$$

The $d\Gamma$ on the left-hand side of the equation can be substituted for by taking the differential form of eq. (16); this leads to a differential equation of δ as a function of ϕ :

$$- e d\phi = \delta d(\delta^3 \sin\phi) \quad (26)$$

where

$$e = \frac{3R\mu_f k_f (T_w - T_s)}{\bar{h}_{fg} g \rho_f (\rho_f - \rho_g)} \quad (27)$$

Equation (26) is identical to Nusselt's equation for film condensation [15] except that the signs of the two sides of the equation are different, and the temperature difference term is $(T_s - T_w)$ instead of $(T_w - T_s)$ in

eq. (27). (See eq. (35).) The difference is due to the fact that film thickness decreases, and the direction of heat transfer reverses, i.e., from wall to film, during vaporization. However, if $(T_s - T_w)$ has been used in defining e , a differential equation identical to that for condensation would have resulted.

In order to solve the differential equation (26), a non-dimensional variable is introduced:

$$z = \frac{\delta^4}{e} \quad (28)$$

and eq. (26) becomes

$$\frac{3}{4} \sin\phi \frac{dz}{d\phi} + z \cos\phi + 1 = 0 \quad (29)$$

This linear differential equation is readily solved as

$$z = \frac{-4}{3 \sin^{4/3}\phi} \left(\int_0^\phi \sin^{1/3}\phi' d\phi' + C \right) \quad (30)$$

Assuming that the fully developed region starts at the angular position ϕ_d , the integration constant C is to be evaluated by the boundary condition at ϕ_d , where the film thickness based on hydrodynamic consideration is given by eq. (16). Assuming that the film flow rate at ϕ_d is Γ_i , the irrigation flow rate at the top of the tube, the film thickness at ϕ_d is

$$\delta(\phi_d) = \left[\frac{3\mu_f \Gamma_i}{g\rho_f(\rho_f - \rho_g) \sin\phi_d} \right]^{1/3} \quad (31)$$

The integration constant C is thus obtained as

$$C = -\frac{3}{4e} \left[\frac{3\mu_f \Gamma_i}{g\rho_f(\rho_f - \rho_g)} \right]^{4/3} - \int_0^\phi \sin^{1/3} \phi d\phi \quad (32)$$

Substituting C back into eq. (30) yields the film thickness as a function of ϕ

$$\delta(\phi) = \left\{ \left[\frac{3\mu_f \Gamma_i}{g\rho_f(\rho_f - \rho_g) \sin \phi} \right]^{4/3} - \frac{4e}{3 \sin^{4/3} \phi} \int_0^\phi \sin^{1/3} \phi' d\phi' \right\}^{1/4} \quad (33)$$

At this point, it is worthwhile to compare eq. (33) with Nusselt's solution for film condensation [15],

$$\delta_{\text{cond}}(\phi) = \left[\frac{4e_{\text{cond}}}{3 \sin^{4/3} \phi} \int_0^\phi \sin^{1/3} \phi' d\phi' \right]^{1/4} \quad (34)$$

where, as mentioned before, the temperature difference $(T_s - T_w)$ instead of $(T_w - T_s)$, is used in defining e for condensation; i.e.,

$$e_{\text{cond}} = \frac{3R\mu_f k_f (T_s - T_w)}{h_{fg} g \rho_f (\rho_f - \rho_g)} \quad (35)$$

Comparing with eq. (34), there is an extra non-integral term in eq. (33), which is due to the finite film thickness at the inlet in the case of falling film evaporation, and the minus sign of the integral term is because film thickness decreases with respect to ϕ during evaporation.

Based on the film thickness solution, the fully developed heat transfer coefficient at any position ϕ is given by

$$h_{fd}(\phi) = \frac{k_f}{\delta(\phi)}$$

$$= \frac{k_f}{\left\{ \left[\frac{3\mu_f \Gamma_i}{g\rho_f(\rho_f - \rho_g) \sin\phi} \right]^{4/3} - \frac{4e}{3\sin^{4/3}\phi} \int_{\phi_d}^{\phi} \sin^{1/3}\phi' d\phi' \right\}^{1/4}} \quad (36)$$

and the mean value of Nusselt number over the fully developed region is

$$\begin{aligned} \overline{Nu}_{fd} &= \frac{\overline{h}_{fd} e^{1/4}}{k_f} \\ &= \frac{1}{\pi - \phi_d} \int_{\phi_d}^{\pi} \frac{\sin^{1/3}\phi}{(A - \frac{4}{3} \int_{\phi_d}^{\phi} \sin^{1/3}\phi' d\phi')^{1/4}} d\phi \end{aligned} \quad (37)$$

where

$$A = \left[\frac{3\mu_f \Gamma_i^4}{g\rho_f(\rho_f - \rho_g)} \right]^{1/3} \left[\frac{h_f g}{Rk_f(T_w - T_s)} \right] \quad (38)$$

and e is defined in eq. (27). Note the \overline{Nu}_{fd} is based on $e^{1/4}$. A result similar to eq. (37) was obtained by Sabin and Poppendiek [16]; however, the constant in the denominator of the integrand was only one half of that of A as given by eq. (38). This led to an over-estimation of the mean heat transfer coefficient. This might be the reason why their prediction was purported to be in good agreement with the experimental data, even though the effects of the jet impingement region and the thermal developing region were not considered in their model.

It is observed that the smaller the value of A , the greater is \overline{Nu}_{fd} . However, a mathematical problem arises when A is smaller than $\frac{4}{3} \int_{\phi_d}^{\pi} \sin^{1/3}\phi' d\phi'$. Physically, this lower limit corresponds to

incipient dryout at the bottom of the tube. The heat transfer coefficient increases due to effective heat transfer across a thin liquid film when the flow rate is small.

The integral in eq. (37) can be estimated through numerical integration as exemplified in Table 3. The easier way is to get \overline{Nu}_{fd} from Fig. 10, in which the computer solution to eq. (37) is plotted. Data shown in Fig. 10 are generated by fitting a sixth-degree polynomial to the integral $\int_0^\phi \sin^{1/3} \phi' d\phi'$, and numerically integrating using the trapezoidal rule. The mean fully developed heat transfer coefficient is quite constant for ϕ_d up to 90° .

Finally, the overall average heat transfer coefficient can be calculated by summing heat transfer contributions from each of the flow regions:

$$\bar{h} = \bar{h}_s \left(\frac{\phi_s}{\pi} \right) + \bar{h}_i \left(\frac{\phi_i - \phi_s}{\pi} \right) + \bar{h}_d \left(\frac{\phi_d - \phi_i}{\pi} \right) + \bar{h}_{fd} \left(1 - \frac{\phi_d}{\pi} \right) \quad (39)$$

For most cases, \bar{h}_s and \bar{h}_i are one order of magnitude greater than \bar{h}_d and \bar{h}_{fd} . However, because the effect of jet impingement is significant in a small region of $0 \leq \phi \leq \phi_i$, the jet impingement accounts for only a small portion of the overall average heat transfer coefficient. The major contribution is from the thermal developing region. Data based on the present model will be compared with experimental results and other predictions reported in Chapter V.

Table 3. Example of calculating the integral in eq. (37), $\phi_d = 25^\circ$, $A = 2828$

ϕ, dgr	ϕ, rad	$\int_0^\phi \sin^{1/3} \phi' d\phi'$	$\int_d^\phi \sin^{1/3} \phi' d\phi'$	$\frac{\sin^{1/3} \phi}{(A - \frac{4}{3} \int_d^\phi \sin^{1/3} \phi' d\phi')^{1/4}}$
0	0	0	-	-
5	0.08727	0.029025	-	-
10	0.17453	0.073102	-	-
15	0.26180	0.125416	-	-
20	0.34906	0.183833	-	-
25	0.43633	0.247157	0	0.102926
30	0.52359	0.314582	0.067425	0.108840
35	0.61086	0.385507	0.138350	0.113938
40	0.69813	0.459450	0.212293	0.118349
45	0.78540	0.536008	0.288851	0.122172
50	0.87266	0.614831	0.367674	0.125478
55	0.95993	0.695605	0.448448	0.128314
60	1.04720	0.778044	0.530887	0.130718
65	1.13446	0.861881	0.614724	0.132715
70	1.22173	0.946864	0.699707	0.134326
75	1.30900	1.032753	0.785596	0.135566
80	1.39626	1.119315	0.872158	0.136445
85	1.48353	1.206323	0.959166	0.136971
90	1.57080	1.293552	1.046395	0.137146
95	1.65806	1.380781	1.133624	0.136973
100	1.74533	1.467789	1.220632	0.136451
105	1.83260	1.554351	1.307194	0.135575
110	1.91986	1.640240	1.393083	0.1343373
115	2.00713	1.725223	1.478066	0.1327286

Table 3 (Continued)

ϕ , dgr	ϕ , rad	$\int_0^\phi \sin^{1/3} \phi' d\phi'$	$\int_\phi^d \sin^{1/3} \phi' d\phi'$	$\frac{\sin^{1/3} \phi}{(A - \frac{4}{3} \int_\phi^d \sin^{1/3} \phi' d\phi')^{1/4}}$
		$= \int_0^\phi \sin^{1/3} \phi' d\phi' - \int_0^\phi \sin^{1/3} \phi' d\phi' = K$		$= \frac{\sin^{1/3} \phi}{(A - \frac{4}{3} K)^{1/4}}$
120	2.09440	1.809060	1.561903	0.1307322
125	2.18166	1.891499	1.644342	0.1283297
130	2.26893	1.972273	1.725116	0.1254979
135	2.35619	2.051096	1.803939	0.1221943
140	2.44346	2.127654	1.880497	0.1183720
145	2.53073	2.201597	1.954440	0.1139622
150	2.61800	2.272522	2.025365	0.1088656
155	2.70526	2.339947	2.092790	0.1029327
160	2.79253	2.403271	2.156114	0.0959234
165	2.87979	2.461688	2.214531	0.0874129
170	2.96706	2.514002	2.266845	0.0765249
175	3.05433	2.558079	2.310922	0.0608154
180	3.14159	2.587104	2.339947	0.0000000
Trapezoidal rule: $\int_0^\pi \frac{\sin^{1/3} \phi' d\phi'}{(A - \frac{4}{3} \int_0^\pi \sin^{1/3} \phi' d\phi')^{1/4}}$				
$= 0.3238923$				

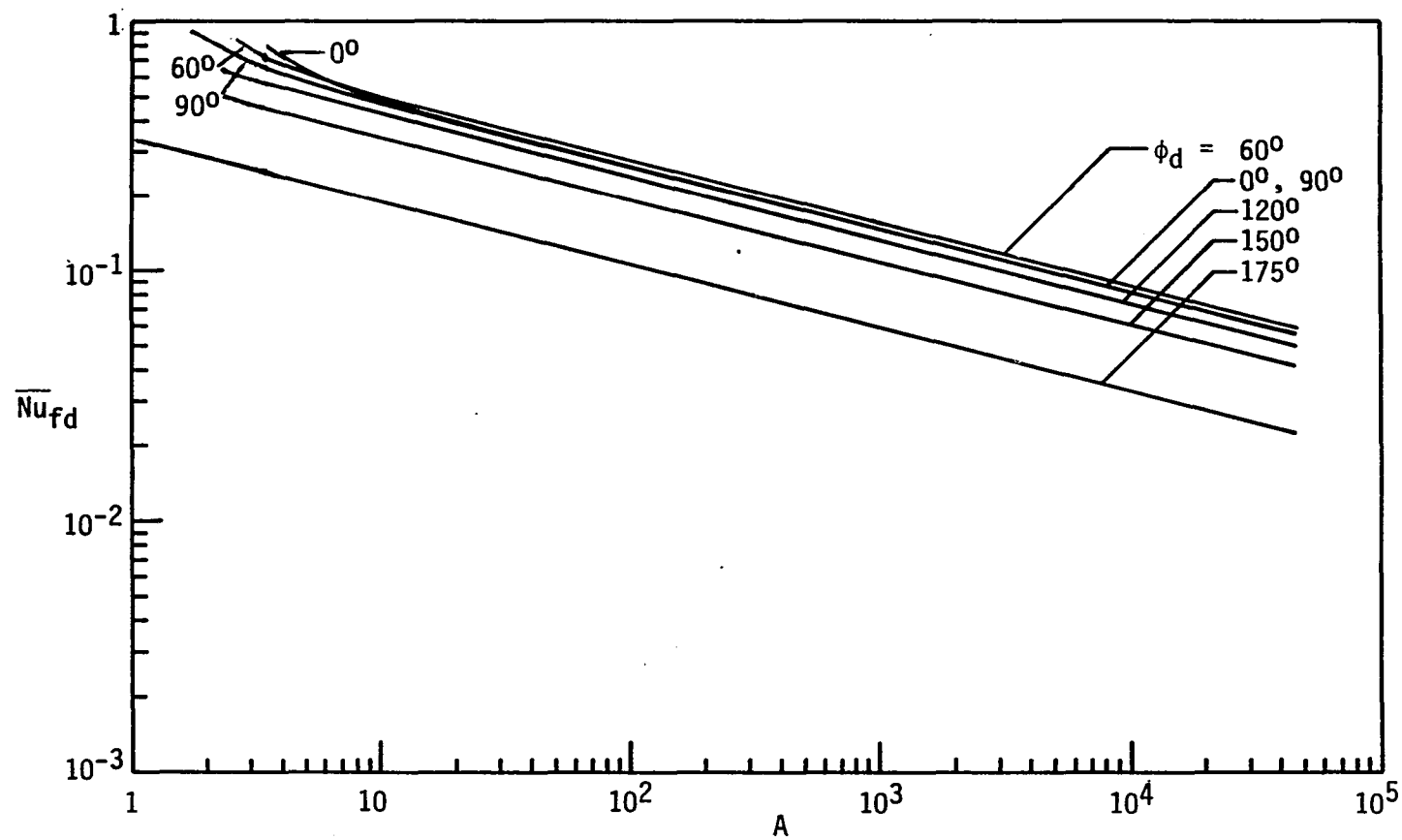


Fig. 10. Analytical predictions of Nusselt number in the fully developed region

IV. EXPERIMENT

A. Apparatus

1. General arrangement

The requirement for the test facility was to provide an even distribution of water at saturation to an electrically heated horizontal tube in a saturated vapor atmosphere for specified ranges of flow rate and heating power. As shown in Fig. 11, the degassed and preheated water was circulated by a pump (Oberdorfer #3000R, 600 rpm, driven by a Dayton capacitor ac motor, 0.5 hp, 1725 rpm) through a filter, deionizer, and flowmeter to feed the test chamber. The bypass across the pump helped control the flow rate. A diamond filter tube for the filter shell was used. Water ran through the deionizer (Barnstead, Ultrapure) before each test; however, the deionizer was bypassed when the water temperature exceeded 49°C, as specified by the manufacturer as a limit of operation. The flow rate into the test chamber was fine-controlled by a needle valve.

For preheating and degassing, the water was boiled in the degassing/surge tank (stainless steel, 33 cm dia. x 28 cm) by an electric heater (Chromalox, 3000 W). The vapor generated in the degassing/surge tank and the test chamber was condensed in a water-cooled condenser. The condensate was directed back to the tank. The pressure in the chamber was very close to atmospheric. Most of the lines were 12.7 mm O.D. copper tubing.

A test chamber was designed and constructed to perform either spray evaporation or flooded boiling. As shown in Fig. 12, an inner chamber holding the liquid distributor, test section, and auxiliary heater was placed inside the large chamber. There was communication between inner and

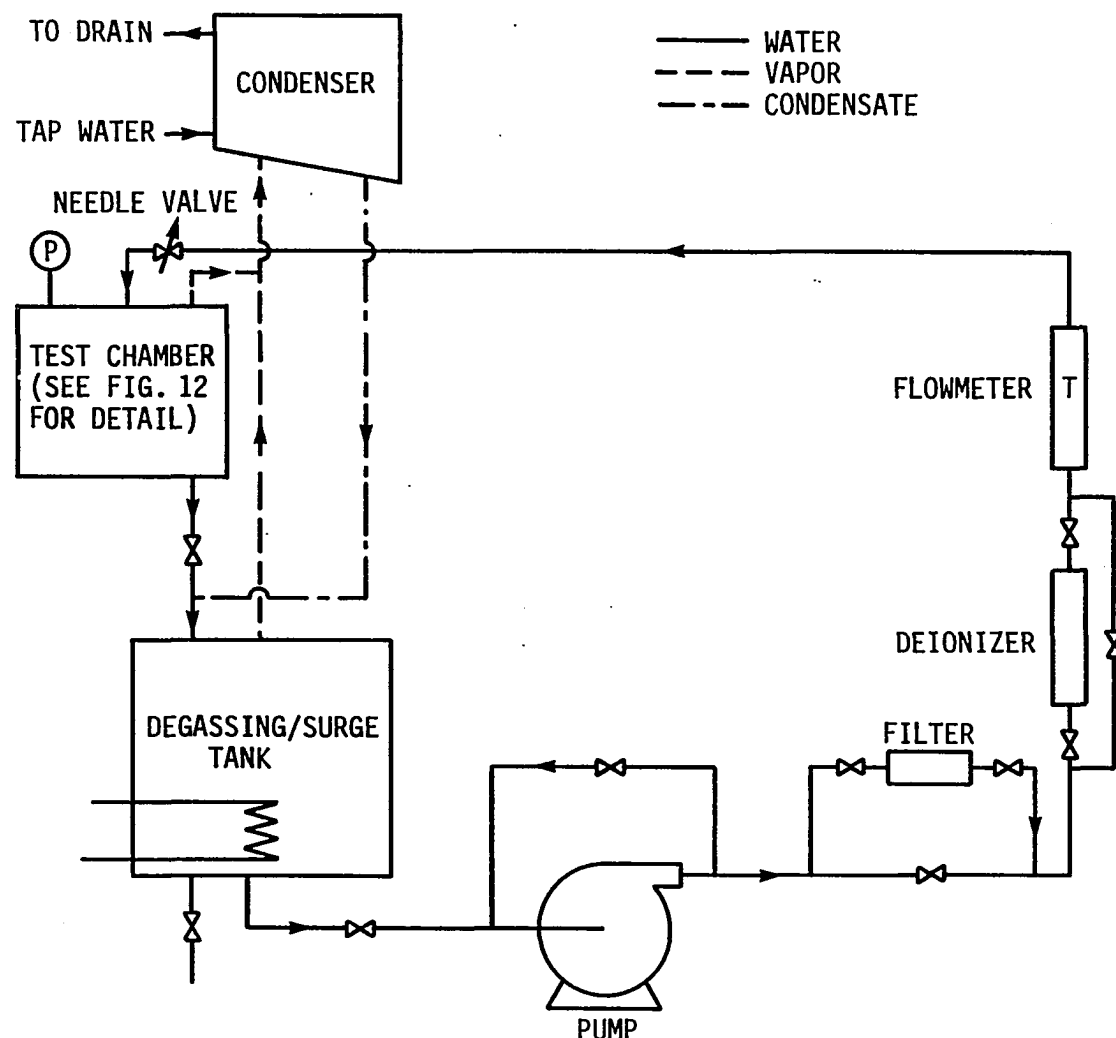


Fig. 11. Test facility for falling film evaporation and pool boiling on a horizontal tube

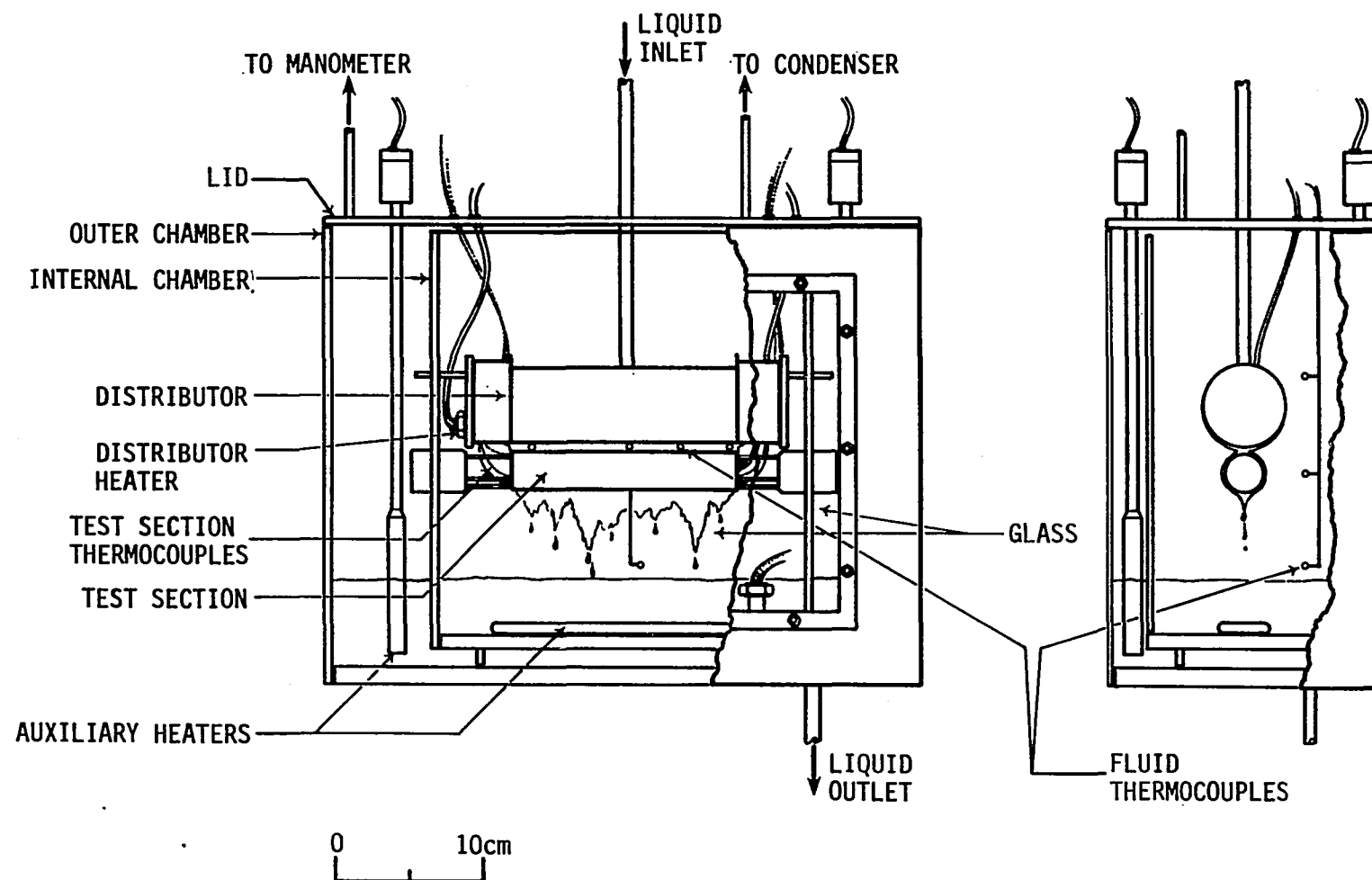


Fig. 12. Test chamber for spray evaporation and pool boiling tests (spray mode shown)

outer chambers so that the liquid levels were the same. The double-chamber configuration was important in maintaining saturated conditions in the inner space without the use of heavy insulation which would have hindered visual observations. It also isolated the test section from the rather strong circulation induced by the four auxiliary heaters (120 v, 500 W each) required for the pool boiling tests. A compromise between maintaining the pool temperature and reducing the convection currents induced by the auxiliary heaters was necessary when there was no shield between the heaters and the test section [56].

Both chambers were made of aluminum with glass windows on the front and rear sides. The fluid thermocouples were used to measure the vapor space temperature or the pool temperature, depending on the mode of test. Maintenance of saturated conditions was particularly important for both tests. The test cylinder was supported by three rods which were secured to brass fittings at either end. The hardware was arranged so that the test cylinder could be rotated and secured in any position. The distributor fed saturated water on the test cylinder. Because the film heat transfer coefficient depends on the ambient vapor content and temperature, an auxiliary heater (240 v, 1000 W) was placed at the bottom of the inner chamber and was always flooded with water during the tests to help saturate the space with vapor. The vapor space in the inner chamber was maintained within 0.1 K of the saturation temperature.

Different distributors were tried before the one with the best performance was developed. Previous experience suggested that a tube perforated with circular holes at the bottom is the most straightforward type [5,60]. A similar configuration is a tray with a perforated bottom

[10] or with a continuous slit [12]. All of these types of distributors were tried in the present study.

In all cases, it was found that due to the temperature gradient built up within the supply tube in the vertical direction, the water coming out from the bottom of the distributors was always subcooled, even if the water was heated by a preheater installed in the supply tube. The discontinuous liquid feed from the spaced holes created ridges and valleys in the film on the test cylinder. The flow distributed by a slot tended to converge into a column due to surface tension and never became a uniform sheet. The flow was subject to interruption when impurities were caught at any point along the slot. These problems were resolved by using a supply tube perforated at the apex [1,61]. Water at the highest temperature overflowed out of the spaced holes, and redistributed itself uniformly as it flowed around the tube wall. This type of distributor was further improved for the present experiment.

As depicted in Fig. 13, the flow distributor assembly employed consisted of a threaded cylindrical shell and two head plates, enclosing a perforated-pipe internal distributor and a cylindrical heater. The heater (Watlow, 240 v, 2000 W) was attached to one of the head plates. The head plates were secured to the shell by four threaded rods. Gaskets were employed between the head plates and the shell to prevent leakage. The head plates were made of aluminum, and the shell and the perforated pipe of brass. The internal distributor was designed so that the incoming liquid was uniformly distributed (see Appendix 1). Maldistribution of the inlet liquid with its substantial subcooling by the perforated pipe would have caused a non-uniform temperature distribution within the distributor shell.

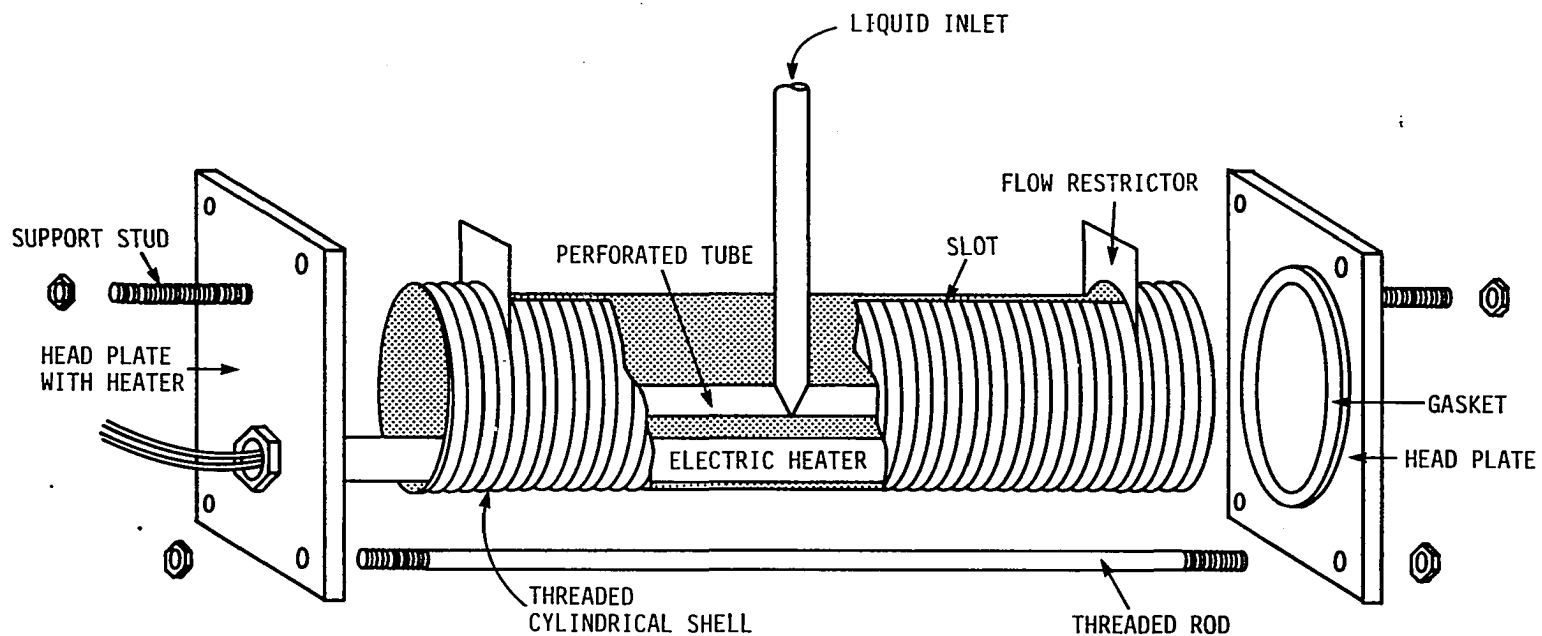


Fig. 13. Flow distributor assembly

The non-uniformity would have been also shown by non-uniform liquid efflux out of the distributor. The percentage of maldistribution of the perforated pipe was estimated to be smaller than 3 percent (Appendix 1).

Subcooled liquid evenly distributed by the perforated pipe was then boiled by the electric heater in the shell. The liquid at upper level, which was very close to saturation, overflowed through the slot. The slot had exactly the same length as the test section and two flow restrictors were provided on the ends to make sure that all the liquid fed the test section. The threads ensured total wetting of the shell surface downstream of the slot. Liquid left the bottom of the shell in columns or drips not from fixed points, but from random points moving along the bottom line. This idealized the real feed situation in a spray evaporator where lower tubes receive the surplus feed from the tubes above. The liquid formed in a sheet between the distributor and the test section when the distance between the two was smaller than 3 mm.

The liquid feed height was adjusted by moving the distributor up and down along slots on the side walls of the inner chamber. The longitudinal temperature variation of the feed, as monitored by thermocouples at the bottom of the shell, was always within ± 0.1 K, and the average subcooling at that location was maintained within 0.1 K. The distribution of the feed could not be obtained quantitatively; however, the flow was believed to be evenly distributed judging from the uniform frequency of dripping at random points along the bottom line of the distributor.

2. Test cylinders

Test cylinders were of copper, nominally 25.4 mm in diameter and 110 or 152 mm in length. A central 12.7 mm diameter hole was provided for a

cartridge heater. Six thermocouple wells of 1 mm diameter were drilled 60° apart, with outer edges approximately 1.5 mm from the outer base surface and 40 or 50 mm in depth. In order to reduce the difficulty incurred from drilling small holes for a long distance, thermocouple wells were prepared by two stages of drilling in some cylinders, i.e., 1.3 mm diameter for 38 mm deep and 1 mm for another 12 mm. Some thermocouple wells were prepared by drilling oversize holes to accommodate copper capillary tubes which were soldered into the holes. The thermocouples were then inserted through the capillary tubes. The bottom of the holes was located following the method described in Appendix 2. The cartridge heaters (Watlow Electric, J6A36, 240 v, 1000 W) were soldered to the cylinder. In some tests, high power density heaters (Watlow Electric, J6AX531A, 240 v, 2320 W) were used. The leads of the heater were encased in heat-shrinkable tubing to protect the wires from moisture. Both ends of the test cylinder were insulated with silicone seal.

The five test sections had the following characteristics:

1 smooth surface, machined microroughness

GEWA-T19C Wieland Werke Metallwerke "GEWA-T" deformed low fin surface, 19 fins/in., 0.25 mm gap width, PD = 25.05 mm, d_k = 23.05 mm, h_R = 1.0 mm, ID = 12.7 mm, S = 5.175 mm (see Fig. 2)

GEWA-T26B similar to above except 26 fins/in., 0.15 mm gap width,

OD = 24.95 mm, d_k = 22.95 mm, h_R = 1.0 mm, ID = 12.7 mm, S = 5.125 mm (see Fig. 2)

TE Hitachi "Thermoexcel-E" tunnel-pore surface, 0.12 mm pore diameter (see Fig. 3)

HF Union Carbide Linde "High Flux" porous metallic matrix surface, 0.38 mm thick; about 45 percent of the copper particles constituting the matrix ranging from 200 mesh (74 μm) to 325 mesh (44 μm), with the remainder being finer

All the surface treatments were provided by the manufacturers. The GEWA-T, TE, and HF were sized for boiling water.

3. Instrumentation

Temperatures were sensed with copper-constantan thermocouples (ANSI Type T, Teflon insulated, AWG 30, Omega Engineering, Cat. No. TT-T-30). Thermocouple readings were monitored by the ISU Heat Transfer Laboratory Data Acquisition System [62]. The system basically was composed of an ice-point reference, an A/D converter, a scanner, a calculator, and a printer. The calculator could be instructed by a program to command the scanner to close a selected channel of thermocouple input received from the ice-point reference and the probe junction. The analog signal from the scanner was then converted to a digital signal by the A/D converter, which was subsequently transmitted to the calculator. Temperature readings were then compared with a program converting emf to temperature. Another channel was then selected, and the process repeated. The temperature

measuring system was calibrated against a precision thermometer. Details of the calibration are described in Appendix 3A.

In addition to the twelve thermocouples inserted in the test section, four were installed at the bottom of the flow distributor to monitor the feed temperature, and another three were located at different levels in the inner chamber for the vapor space temperature. (See Fig. 12.) As for the flooded tests, thermocouples for the distributor were not needed because there was no liquid feed, and the three chamber thermocouples monitored the pool temperature at different levels.

The alternating current power supplied to the test-section heater was adjusted by a powerstat (Superior Electric, primary 230 v, output 0-270 v, maximum output 2.4 kva, maximum output current 9 a) and monitored by a wattmeter (Weston electrodynamometer wattmeter, Model 310). The wattmeter was calibrated as described in Appendix 3B. The power to the heater in the flow distributor was adjusted by a powerstat (Superior Electric, primary 230 v, maximum output 2.4 kva, 9 a) and monitored by an A. C. ammeter (Simpson, 10 a). The power supplied to the auxiliary heater in the inner test chamber was adjusted by a powerstat (General Radio, primary 230 v, maximum output 2 kva, 9 a). The four auxiliary heaters located in the outer chamber were simultaneously controlled by a powerstat (Superior Electric, primary 115 v, maximum output 3.5 kva, 26 a). The power to the heater in the degassing/surge tank was controlled by another powerstat (General Radio, 240 v, 8 a open rating, maximum output 260 v).

The atmospheric pressure was measured with a mercury barometer which was calibrated against a precision barometer in the Department of Meteorology. An inclined mercury manometer was used to verify that

the pressure differential between the chamber and its surroundings was negligible. The flowrate into the distributor was measured by a rotameter (Brooks, Model 1110, size 8). The rotameter was calibrated in accordance with the recommendations and limitations given by the manufacturer. Details of the calibration are described in Appendix 3C. The liquid feed height was obtained by marking the wall of the inlet pipe of the distributor when it touched the test cylinder (zero feed height), and measuring the height to which the mark was raised.

B. Experimental Procedure

Prior to running, the test sections were cleaned with acetone to ensure cleanliness and wettability. The distilled water was circulated through the deionizer when the temperature was below the operating limit. For the spray evaporation test, the distilled water was brought to the saturation condition and was degassed by circulating and heating with the auxiliary heater in the inner chamber, the heater in the degassing/surge tank, and the heater in the distributor. The heating process generally required about one hour. For the flooded tests, there was no circulation, and the distilled water in the test chamber was heated and degassed by the auxiliary heaters in the outer chamber. For all tests, the test cylinder was always installed during the preheating, but the test heater was not powered before the saturation condition was reached.

Due to the sophisticated nature of falling film evaporation, factors which might affect either convection or nucleate boiling heat transfer were explored. The variables known to be influential in convection for a particular fluid were film flow rate and liquid feed height [7]. The

variables known to affect nucleate boiling were surface aging, surface subcooling, rate of heat flux change, and direction of heat flux change [56]. Influences on heat transfer due to the interaction between these two groups of variables were investigated through a carefully arranged test program. Above all, surface geometry was the most interesting factor to be explored.

Curves of experimental results were coded for convenience as follows:

Mode of flow - Test section - Surface aging - Surface subcooling -
Heat flux - Film flowrate - Ratio of liquid feed height to tube
diameter - Qualitative rate of heat flux change - Direction of heat
flux change.

The dimensionless liquid feed height as used in Owens [7] correlation was adopted as the variable for the effect of liquid feed height. The heat flux, film flowrate, and ratio of feed height to tube diameter are not applicable to the pool boiling test curves.

The codes used for the above terms are defined as follows:

Mode of flow	FFE = falling film evaporation
	PB = pool boiling
Test section	1 = smooth surface
(see IV-A-2 for	GEWA-T19C = GEWA-T surface, 19 fins/
details)	in., 0.25 mm gap width
	GEWA-T26B = GEWA-T surface, 26 fins/
	in., 0.15 mm gap width
	TE = Thermoexcel-E surface
	HF = High Flux porous surface
Surface aging	D = Tube surface was heated in the air

by its built-in heater to about 20 K above saturation temperature to evaporate the probable liquid entrapped in the pores. Then the surface was cooled down to slightly below saturation so that there was no quenching when applying feed or submersion. The test section was not heated before the working fluid (and surface) subcooling was removed

B = surface was given a high heat flux (about 90,000 W/m²), so as to trigger fully-established nucleate boiling in saturated liquid; and this continued for more than 30 minutes before the run

Surface subcooling

The temperature difference between saturation and the temperature to which the surface was cooled after pre-drying or pre-boiling and before the run, K

Heat flux, q"

Heat transfer rate per unit area, W/m²

Film flowrate, Γ

Liquid film flowrate per unit length per side of tube, kg/s-m

Ratio of liquid feed height to tube diameter, H/D The ratio of the distance between the bottom of the flow distributor and the top of the test cylinder to the cylinder diameter, dimensionless

Qualitative rate of heat flux change C = power was increased or decreased continuously and slowly (about 4000 W/m²-min) to a new operating condition
S = power was changed stepwise, from hundreds to thousands of W/m² per step

Direction of changing heat flux INC = increasing heat flux
DEC = decreasing heat flux

A "V" (variable) was used to code one of those quantitative variables, i.e., q", Γ , and H/D, when it was taken as the independent variable in that particular test run.

For example, FFE-TE-D-78-V-0.0606-1.0-C represents the water falling film evaporation curve of the Thermoexcel-E surface according to the following procedure:

1. Heat the tube in air by its built-in heater to about 20 K above saturation temperature, and then cool it down to slightly below saturation.
2. Turn on the circulation pump and spray distilled water at 78 K subcooling on the test cylinder.
3. Supply electric power to the auxiliary heater in the inner chamber, the heater in the degassing/surge tank, and the heater

in the distributor, to bring the circulating water to saturation.

No power is supplied to the test heater at this moment.

4. Adjust flowrate through the needle valve at the inlet of the test chamber and adjust liquid feed height by moving the flow distributor up or down.
5. Adjust the power to the distributor heater and the auxiliary heater so that the feed and space subcoolings are within tolerable limits.
6. Increase the power to the test section heater, continuously and slowly, and start taking data.

The following quantities are then measured: power to the test section heater, atmospheric pressure, and pressure difference between atmosphere and test chamber. These quantities are read into the calculator in the Data Acquisition System. Based on these quantities and the test section temperatures sampled, the calculator computes average heat flux and average wall superheat. Details of the data reduction are described in the next section. The power is increased up to the power limit of the test section heater, and is subsequently decreased down to zero so as to generate a complete boiling curve. The feed and film flow patterns were observed periodically to spot any maldistribution, surface wetting problems, or bubble generation.

As another example, FFE-HF-B-23-1.028x10⁴-V-2.0-S represents the falling film evaporation curve for the High Flux surface according to the following procedure::

1. Circulate and bring the distilled water to saturation by following step 3 in the last example.

2. Supply the test section with a high heat flux of about 9×10^4 W/m² to trigger fully-established boiling, continuing for at least thirty minutes.
3. Turn off the test section heater, as well as all the other heaters on the loop and let the system cool down. Keep the circulation so that the test section is never exposed to the air.
4. When the test section (and the circulating water) cools down to 23 K below saturation, start reheating the system to saturation by following step 3 in the last example.
5. Repeat step 5 in the last example.
6. Step-increase the power to the test section to the limit, maintaining it for 10 minutes, and then reduce the power to heat flux of 1.028×10^4 W/m². Adjust feed height.
7. Set flowrate at different values by adjusting the needle valve, and record the data.

In the pool boiling tests, there is no circulation through the loop. The outlet of the test chamber is closed and the water level is kept higher than the test section. The distributor is elevated to keep a substantial distance from the test section. The same procedure of surface aging, surface subcooling, qualitative rate of heat flux change, and direction of changing heat flux, as described before, are applicable. In addition to the barometric data, the height of pool level is also taken to calculate the static pressure at the center line of the test section for accurate data reduction.

C. Data Reduction

The heat flux distribution within the test cylinder was studied by solving the two-dimensional heat conduction problem in cylindrical coordinates as shown in Appendix 4A. The inactive zones in the commercial heater placed in the cylinder were located, and the axial heat flux distribution under the influence of the inactive zones was solved. The local value of the surface heat flux where the thermocouples were longitudinally located was taken as the true heat flux. In the case calculated in Appendix 4A, a typical value of h , for the present study $1 \times 10^4 \text{ W/m}^2\text{-K}$, was used. The error introduced by applying this result to heat flux calculations at the different h 's observed in the present tests was negligible.

Each wall temperature could be corrected for the temperature drop over the distance between the thermocouple bead and the base surface according to the temperature distribution solved for in Appendix 4A. However, little error is introduced by assuming uniform radial heat flow and the one-dimensional conduction equation in a cylinder is used:

$$\Delta T_{\Delta r} = \ln[R_o/(R_o - \Delta r)] \frac{R_o q''}{k} \quad (40)$$

$\Delta T_{\Delta r}$ is the temperature drop across Δr , the radial distance between the thermocouple junction and the base surface. The radial position of the bottom of each thermocouple well where the thermocouple junction was located was measured through a novel method presented in Appendix 2.

An attempt was made to obtain accurate wall temperature averages through numerical integration of the six circumferential temperatures.

This required the functional form of the temperature distribution. The circumferential wall temperature profile was measured by rotating the test cylinder. However, the result was never reasonable. The expected profile as shown by the analytical and experimental results reported [5,12] was never obtained.

Through a unique method of inferring the inner heat flux distribution from the outer surface temperature distribution, as described in Appendix 4B, it was verified that the circumferential non-uniformity in the heat flux provided by the commercial electric heater could be as great as ± 50 percent of the average value. The non-uniformity increases with the number of heating-cooling cycles and/or service time. The variation of the outer surface temperature of the cylinder due to the non-uniform internal heating was in the order of magnitude of 0.1°C , depending on the power level. The rather small surface temperature variation was due to the effective thermal equalization provided by the thick-walled copper cylinder employed in the present tests. However, the influence of non-uniform internal heating was still great enough to override the temperature profile resulting from the circumferential distribution of heat transfer coefficient provided by the evaporating falling film.

In Appendix 4C, the influence of the circumferentially non-uniform heat transfer coefficient on the surface temperature profile of a hollow cylinder was studied. It was found that the variation of the outer surface temperature due to the non-uniform heat transfer coefficient distribution provided by the evaporating falling liquid film was in the order of magnitude of 0.1°C , which was commensurate with the variation caused by the

uneven internal heating. Therefore, it was concluded that the expected wall temperature profile could never be obtained by using the present commercial cartridge heater in the test cylinder, because of its uneven heating. Since greater error could have been introduced if numerical integration was employed, it was decided that the arithmetic mean of the twelve extrapolated wall temperatures was sufficient for the average wall temperature. The average of ten samples of this averaged wall temperature, taken over a period of about 5 minutes, was taken as the wall temperature.

The average wall superheat, ΔT , was calculated by taking the difference between the average wall temperature and the saturation temperature. The saturation temperature was calculated by an expression fitting data from the ASME Steam Tables [63]. The test chamber pressure was the sum of the atmospheric pressure and the pressure difference between the chamber and the environment. The pool pressure at the center line of the test section was used to calculate T_s in the flooded tests.

Since every effort was made to uniformly distribute the liquid feed, the film flow rate per unit length per side of tube, $\Gamma(\text{kg/s-m})$, was calculated by dividing half of the total mass flow rate $m(\text{kg/s})$, by the cylinder length, $L(\text{m})$, i.e.,

$$\Gamma = \frac{\dot{m}}{2L} \quad (41)$$

The film Reynolds number was calculated by

$$Re = \frac{4\Gamma}{\mu} \quad (42)$$

The average heat transfer coefficient was calculated based on the local heat flux and average wall superheat at the particular longitudinal

position, i.e.,

$$\bar{h} = \frac{q''}{\Delta T} \quad (43)$$

Examples of the computer program used for data acquisition and reduction are presented in Appendix 5.

The estimated uncertainties for the data presented are as follows:

$\pm 220 \text{ W/m}^2$ in heat flux, $\pm 0.06 \text{ K}$ in wall superheat and surface subcooling, $\pm 0.004 \text{ kg/s-m}$ in film flow rate, and ± 0.1 in ratio of feed height to diameter. The details of error analysis are presented in Appendix 6.

In addition to the plotted data as presented in the following chapter, tabular data are available at the Heat Transfer Lab.

V. RESULTS AND DISCUSSION

A. Test Section 1 - Plain Surface

1. General heat transfer behavior

Two test runs with the same flow rate and feed height, but with different surface aging and way of changing heat flux, are shown in Fig. 14. Additional test runs featuring D-C and B-S with different surface subcooling, are not shown here because the data agree well with those in Fig. 14. It is concluded that B and D treatments with different subcooling, with S or C, INC or DEC, have no significant effect on heat transfer performance. This conclusion was also reached when pool boiling water with the same test section [51].

Analytical prediction based on the model presented in Chapter III, as well as correlations for film evaporation (no nucleate boiling) suggested by Chun and Seban [4], Lorenz and Yung [6], and Owens [7] are compared with the experimental data in Fig. 14. The data are shown to be in good agreement with the present model. They are in even better agreement with the Owens [7] correlation. Since Owens' correlation is actually based on experimental data reported from different sources, the agreement between the present data and Owens correlation implies agreement with other experimental data reported. The present data happen to agree with the Chun and Seban's [4] curve, even though the latter is for the developed film evaporation on a vertical surface.

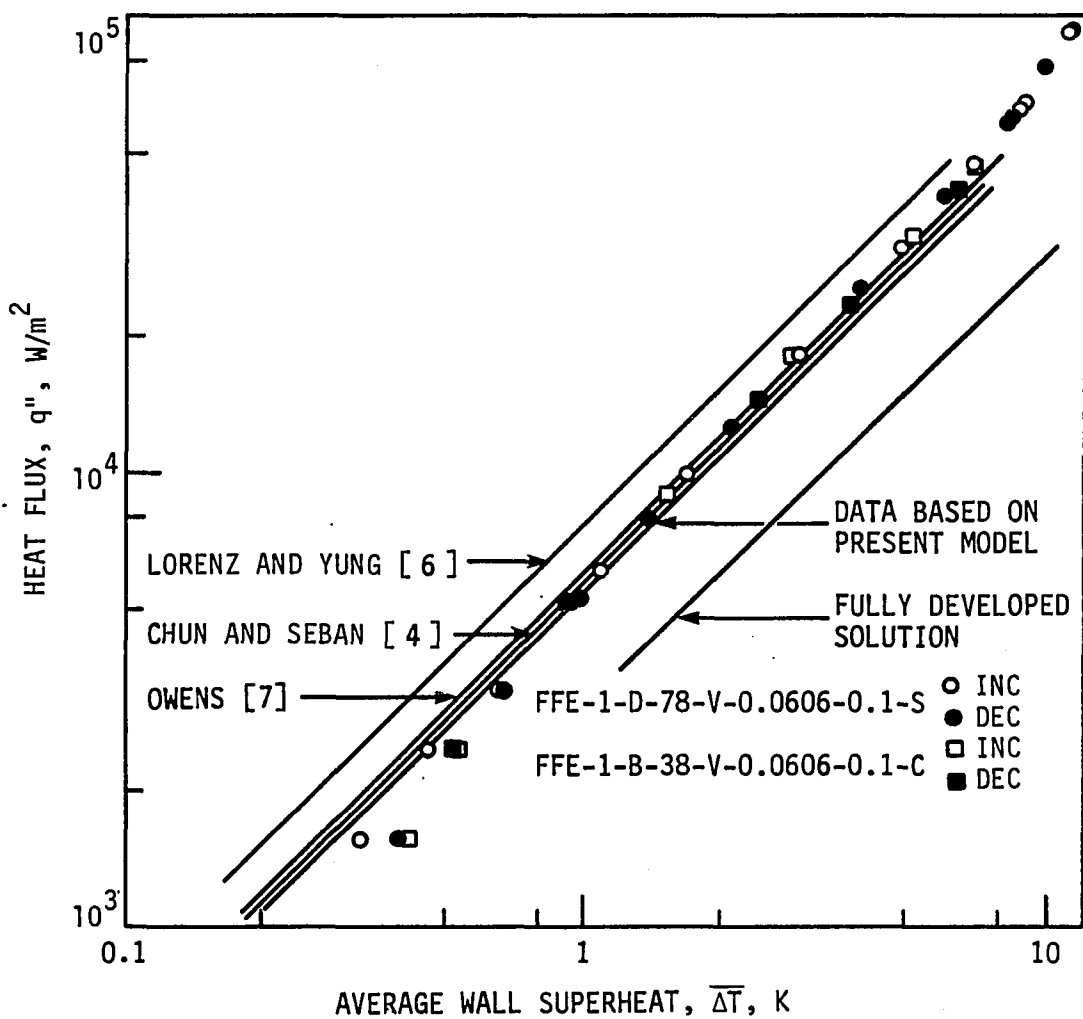


Fig. 14. Effect of surface aging, surface subcooling, heat flux change rate, and direction of power change on falling film evaporation heat transfer of a plain tube, $\Gamma = 0.0606 \text{ kg/s-m}$

The present analysis predicts slightly lower heat transfer rates than the experimental data. This is as expected because the model was developed based on the assumption of a steady two-dimensional jet impinging on the tube. However, perturbation of the film flow generally due to feed impingement in columns (three-dimensional jets) and drops at the top of the tube was evident during the tests. In order to simulate the situation in a real spray evaporator, the feed distributor was so designed that the liquid columns and drops attacked the tube at unsteady points which shifted along the apex line of the tube. This could have further disturbed the film and enhanced the heat transfer coefficient. It was also observed that the feed liquid columns and drops were much larger in size than the assumed jet width. This would have resulted in a larger jet impingement region in which the heat transfer is high. In addition, the non-uniform velocity profile and turbulence level within the impinging jet introduced during jet issuing can significantly affect the heat transfer [64, 65, 66].

Also presented in Fig. 14 is the fully developed solution as given by eq. (37). The average heat transfer coefficient is only about 50 percent of the experimentally observed value if the entire film flow is considered as fully developed. This confirms the importance of the developing region in the model.

The agreement between the present data and non-boiling correlations as well as the lack of a pronounced upswing in the $q'' - \Delta T$ curve indicates that nucleate boiling did not play an important role in falling film evaporation on the plain tube. This is supported by the observations during the tests. For all the test runs, no bubbles were observed at low

power levels. At about $q'' > 2 \times 10^4 \text{ W/m}^2$, tiny bubbles generated at isolated nucleation sites were carried along the tube surface by the falling film. The number and volume of the bubbles generated were judged to be less than in pool boiling. The weak nucleate boiling in the flowing liquid film makes the data present curves only slightly steeper than a constant heat transfer coefficient curve in a q'' vs. ΔT plot. The data show higher heat transfer coefficients than the non-boiling predictions at high heat fluxes because the nucleate boiling gradually increase in intensity as the heat flux increases. Established nucleate boiling is observed at even higher heat flux, which is realized by employing a special high power density heater. This is shown in Fig. 18, which will be discussed later.

Unsteady dry patches on the surface were observed at about $q'' = 4 \times 10^4 \text{ W/m}^2$ or higher. Generally, dryout started with a dry spot somewhere on the tube wall. A dry patch immediately downstream was subsequently formed because the liquid feed to the dry spot was momentarily disrupted. The dry area was then rewetted after several seconds. Apparently, these local dry patches due to low flow rate did not significantly affect the heat transfer coefficient.

2. Effect of film flow rate

The influence of film flow rate on the heat transfer coefficient is illustrated in Fig 15. At low heat flux, when nucleate boiling is not significant, heat transfer is dominated by convection and/or conduction. As depicted by the FFE-1-D-75- 8.958×10^3 -V-1.0-S and FFE-1-D-74- 3.660×10^4 -V-1.0-S data, the heat transfer coefficient is relatively high at low flow rate, as heat is readily conducted across the thin laminar liquid film. As flow rate increases, the heat transfer

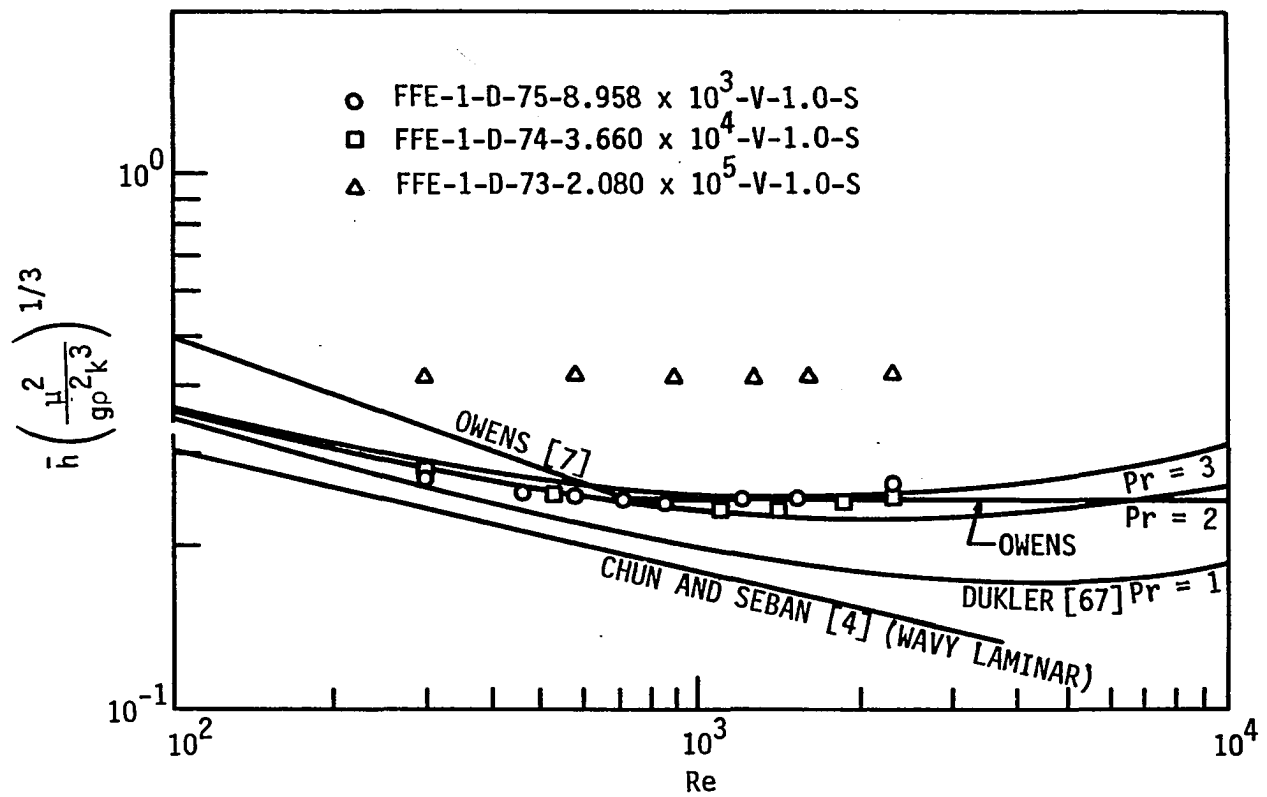


Fig. 15. Effect of film Reynolds number on the falling film evaporation heat transfer coefficient of a plain tube

coefficient decreases due to a thicker liquid film. Convection causes the temperature profile to become non-linear as flow rate is further increased and the film flow turns turbulent. Turbulence causes an increase of h at high Re . The present data for $Pr = 1.75$ are in good agreement with Dukler's [67] predictions for $Pr = 2$. At higher Re , the data are actually in better agreement with Owens' [7] correlation for turbulent non-boiling film evaporation. The result of the present analysis (see Chapter III) can not be presented on a h vs. Re plot because the predicted mean heat transfer coefficient is a function of not only Re but also wall superheat.

At a much higher heat flux (FFE-1-D-73-2.080x10⁵-V-1.0-S), the heat transfer coefficient is higher and constant throughout the test range of Re . This is indicative of established nucleate boiling.

The $q'' - \Delta T$ curves reflect the small changes in heat transfer coefficient with film flow rate, as illustrated in Fig. 16. According to Owens' correlation, a falling film with the flow rate $\Gamma = 0.0371 \text{ kg/s-m}$ should be in the laminar regime, where the heat transfer coefficient is higher than at $\Gamma = 0.0606$ and 0.110 kg/s-m . Although the data presented in Fig. 16 are quite close together, the influence of flow rate is clear.

3. Effect of liquid feed height

The effect of changing liquid feed height on the heat transfer was investigated at different heat fluxes. In Fig. 17, the non-dimensionalized heat transfer coefficients are plotted against the non-dimensionalized feed height adopted in Owens' correlation [7]. The low heat flux data (FFE-1-B-0-1.080x10⁴-0.0606-V-S and FFE-1-B-0-5.503x10⁴-0.0606-V-S) show rather good agreement with Owens' correlation for turbulent falling film

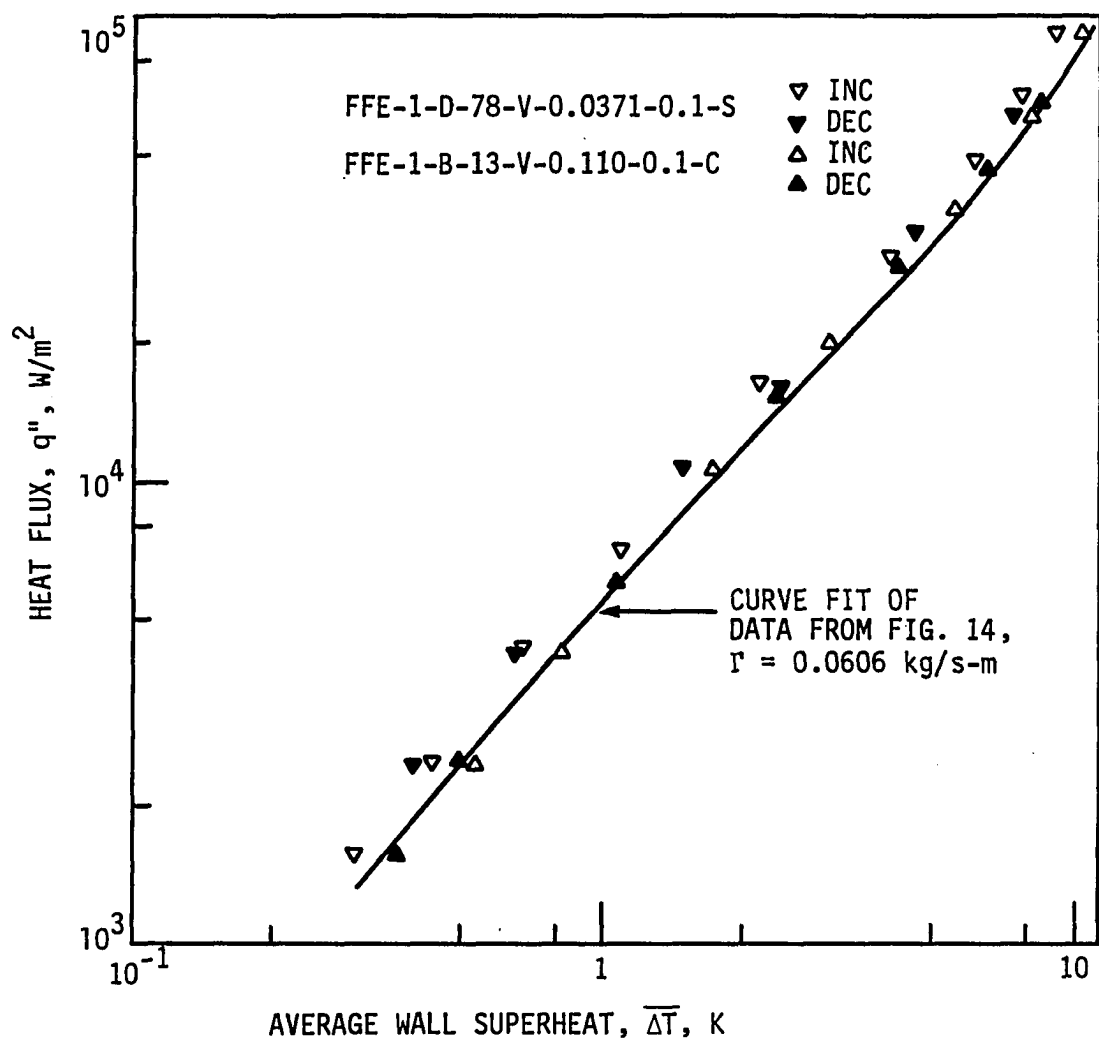


Fig. 16. Effect of flowrate on the heat transfer performance of a plain tube

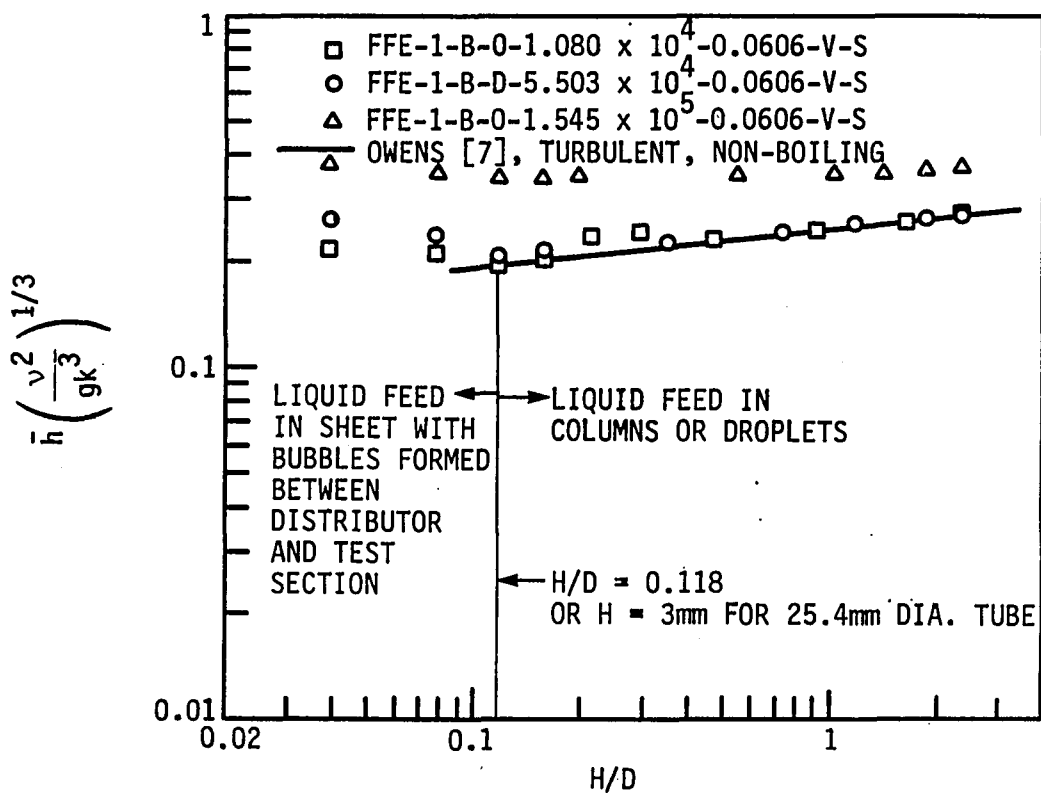


Fig. 17. Effect of liquid feed height on the falling film evaporation heat transfer coefficient for the plain tube

evaporation without boiling in $0.1 < H/D < 2.5$. The slope of the data curve confirms the 0.1 power index of the term H/D used in his correlation.

The change of feed height has a rather weak influence on the heat transfer coefficient at high heat flux. This is due to nucleate boiling in the film flow, which dominates any change in hydrodynamics.

The present data show a minimum heat transfer coefficient at $H/D = 0.118$ or $H = 3$ mm for the 25.4 mm diameter test cylinder. It was observed that liquid feed was distributed in columns (continuous) or droplets (discontinuous) when feed height was large, and in a sheet when H was smaller than 3 mm. In the latter case, bubbles entrained from the distributor in which feed water was boiling, and grew larger in the narrow space between the distributor and the test cylinder. These bubbles were apparently bigger in size than those generated on the surface of the test section due to nucleate boiling. Some of them were carried with the falling film and some of them ruptured between the distributor and the test section. These bubbles were considered to be responsible for the high heat transfer coefficients at very small H/D .

The dynamics of a free-stream bubble flowing with a water film has been studied by Parken [12]. It was assumed that the free-stream bubble at steady state was partially submerged in the water film with its base somewhere below the film-vapor interface and the dome protruding through the interface and exposed to the vapor. There is a thin layer of liquid, the so-called "macrolayer," with a linear temperature profile, under the bubble. The evaporation of the macrolayer provides an efficient means of heat transfer. The wall temperature underneath the bubble was thus lowered

due to the thin macrolayer. This resulted in a higher local heat flux passing through the thin liquid layer. This was verified by an observed bubble growth rate several times higher than that which could be attributed to the uniform heat flux supplied by the heated surface.

Additional enhancement of heat transfer can be attributed to the ripples generated by the bubble. A refined color photographic study [68] revealed that the ambient film was affected by the bubble's presence for approximately one-quarter bubble diameter outwards from the meniscus where concentric ripples surrounded the bubble in this region.

Test runs of the same flow rate but different feed heights are shown in Fig. 18. The data for each H/D follow closely the curves predicted by Owens [7], before nucleate boiling causes a departure from convection at about $q'' = 10^5 \text{ W/m}^2$. The trend for the data to converge to the same fully-established nucleate boiling curve is clear. The high heat flux in the present tests was realized by employing a special high power density heater.

4. Comparison of falling film evaporation and pool boiling

It was one of the objectives of the present study to compare the heat transfer performances of falling film evaporation and pool boiling for smooth and enhanced test sections. The experimental apparatus was arranged so that pool boiling tests could be conducted immediately following falling film evaporation tests (or vice versa). Fig. 19 compares one FFE-1 curve with three PB-1 curves.

The FFE-1-B-0-V-0.0606-1.0-S test was followed by the PB-1-B-0-S test. After increasing the heat flux up to the power limit in falling film

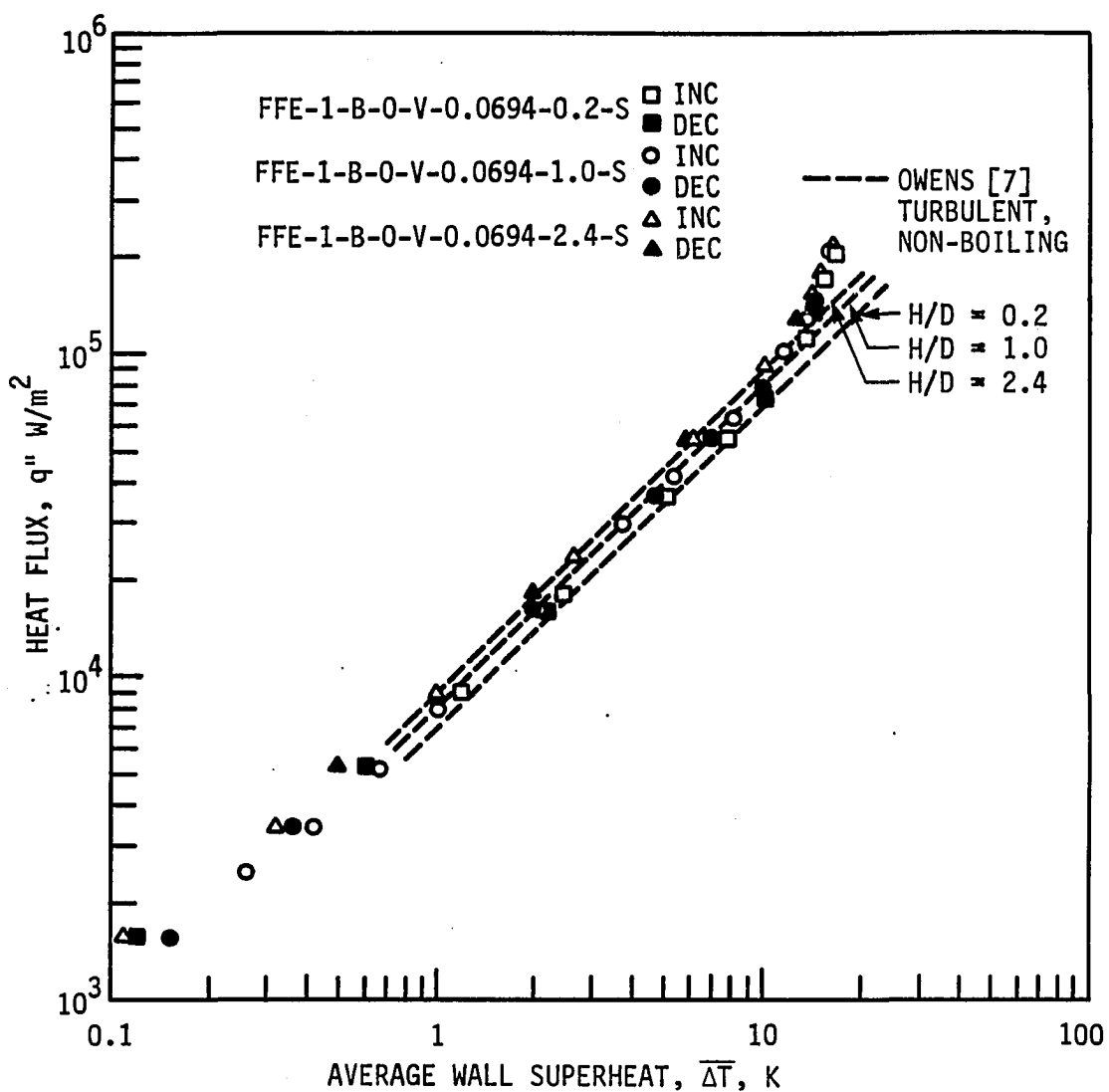


Fig. 18. Effect of liquid feed height on falling film evaporation heat transfer of the plain tube

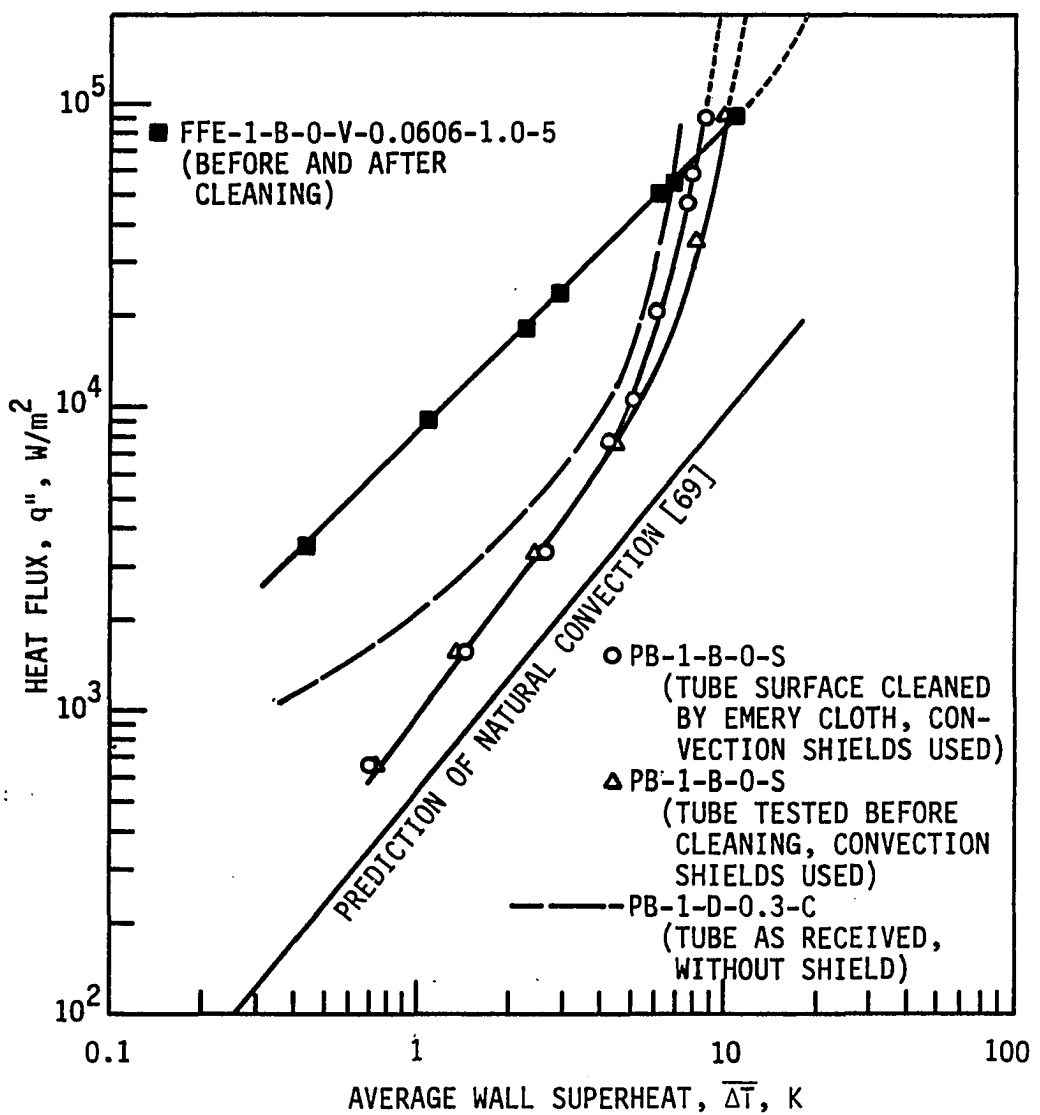


Fig. 19. Comparison of typical falling film evaporation and pool boiling data for the plain tube

evaporation, the system was switched to the pool boiling mode by raising the water level and shutting off the water feed distribution. The heat flux was then lowered to generate a pool boiling curve. The series of tests was subsequently repeated backward, i.e., starting with the pool boiling test, increasing the heat flux up to the limit, shifting to the falling film evaporation, and then lowering the power. These results were identical with the first data. The FFE-1 data of the series agreed well with Owens' [7] correlation, while the PB-1 data showed 40 percent degradation in nucleate boiling heat transfer coefficient ($h = q''/\Delta T$) compared with the pool boiling data of the same test section as received about four years ago, i.e., the PB-1-D-0.3-C data [56]. The two PB-1 curves also differ in the low heat flux range, because convection shields separating the test section from the influence of auxiliary heaters were employed in the PB-1-B-0-S tests. This resulted in the natural convection data being much closer to the prediction at low power level than the PB-1-D-0.3-C data.

The degradation of the pool boiling heat transfer coefficient was apparently due to aging of the surface. A scale or deposit could have resulted from impurities in the boiling liquid, or a film may have formed from oxidation or other chemical reaction. This "fouling" could clog the nucleation cavities in the heater wall, resulting in a higher superheat required for a given heat flux. The cavities may have been quite clogged even though the surface looked clean after the regular cleaning with acetone before the tests. To rejuvenate the aged tube, the surface was manually scraped with aluminum oxide abrasive cloth. A coarser cloth

(No. 240) was first used to scrape off whatever heterogeneous substances were on the surface; then a finer one (No. 600) was used to smooth out the scratches left.

After polishing, the cylinder was shiny and scratch-free as far as the naked eye could tell. The FFE-PB series of tests was repeated after surface rejuvenation. The falling film evaporation data followed the previous data curve, i.e., the FFE-1-B-0-V-0.0606-1.0-S data, while the pool boiling test data shifted to the left of the previous data. Obviously, emery polishing of the heater surface didn't affect the falling film evaporation data because convection was the dominant mode of heat transfer and the thermal behavior was not influenced by any slight change of roughness. The pool boiling coefficient (evaluated at constant q'') showed a 20 percent improvement after cleaning. However, the coefficient was still about 20 percent lower than the data of the cylinder as received (PB-1-D-0.3-C). It is possible that some cavities were still filled with fouling material, since the polishing did not remove much material; these cavities remained inactive. Consequently, the performance of the new tube was not completely restored.

The data in Fig. 19 suggest that the fully-established FFE boiling curve lies to the right of the fully developed PB curve. It is speculated that the higher superheats of the falling film evaporation is due to unfavorable liquid temperature profiles in the thin films compared to those in a pool. The thickness of the thermal boundary layer defined by the film thickness is likely to be less than the thickness of the superheated liquid layer in the pool. For a given heat flux or temperature gradient, the wall

superheat at incipient boiling will be lower for the pool than for the film. The incipient behavior then governs the behavior of the rest of the boiling curve.

B. Test Section GEWA-T - Deformed Fin Surface

1. General heat transfer behavior

The q'' vs. ΔT curves of GEWA-T19C and GEWA-T26B shown in Figs. 20 and 21, were characterized by a relatively high heat transfer coefficient at low heat flux and no sharp upswing which would indicate established nucleate boiling. Hence, the GEWA-T surface can be characterized as a convection-enhancing surfaces. The enhancement is primarily due to extended-surface and surface-tension effects rather than nucleate boiling.

It was visually observed that the circumferential grooves in the surfaces were readily flooded by the liquid. Even the smaller gap width of 0.15mm (GEWA-T26B), which is the minimum available for GEWA-T tubing, was not able to prevent water from entering the channels. At low flow rates, the channels carried the flow and the tips of the deformed fins appeared dry. At higher heat fluxes, bubbles generated inside the channels were observed at the bottom of the tube where flow emerged from the channels. At even higher fluxes, liquid splashed about from the openings because bubbles burst inside the channels. At higher flow rates, the fin tips were wetted; however they dried out at high heat flux. The bubbles tended to remain in the channels and flowed down to the bottom of the tube. This boiling behavior is similar to that observed by Stephan and Mitrovic [39] in flooded boiling with GEWA-T tubes, except that the direction of circulation is reversed. Even though the bubble generation was evident, apparently it was not intense enough to significantly upgrade the already

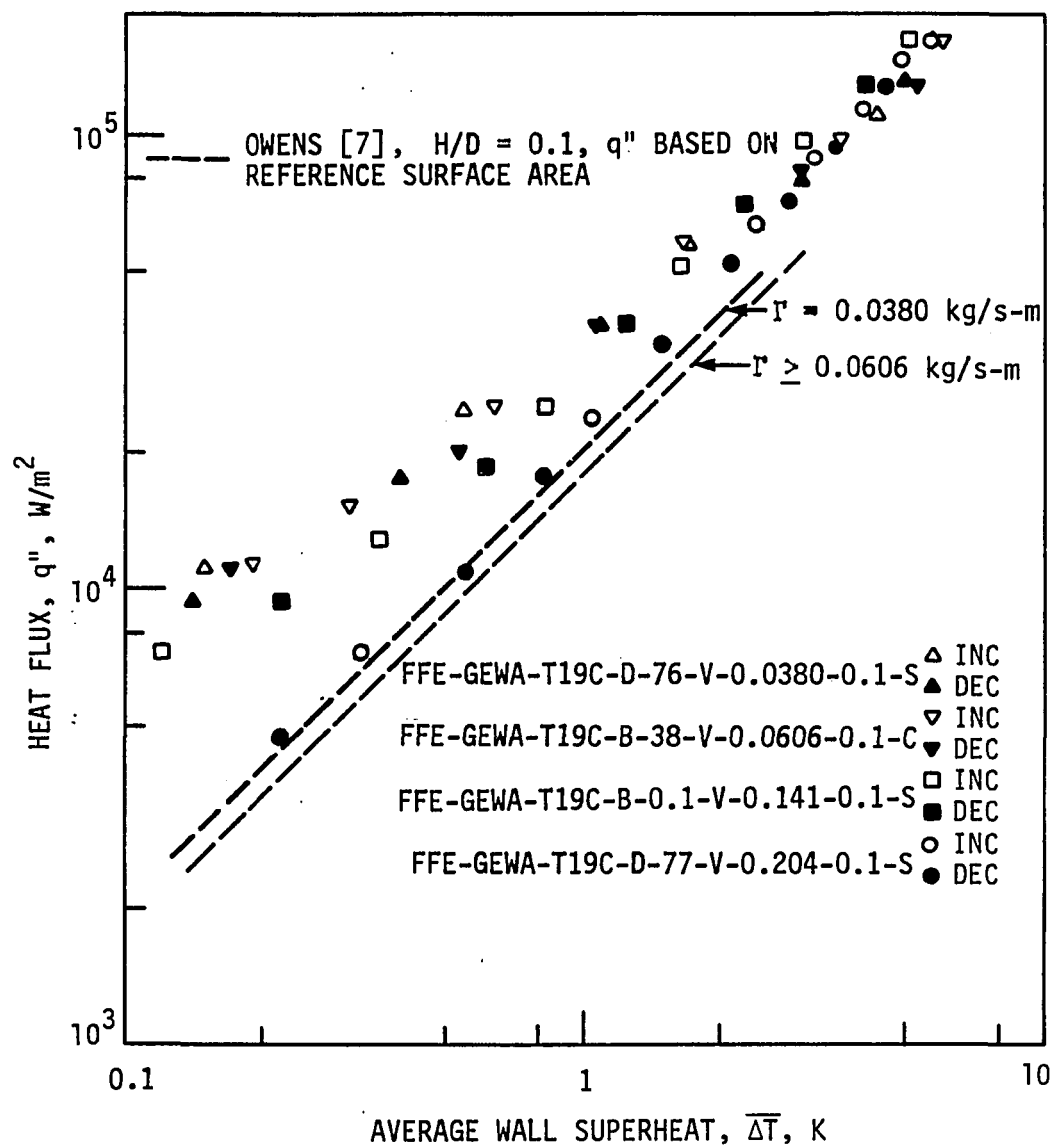


Fig. 20. q'' vs. ΔT curves of FFE-GEWA-T19C tests

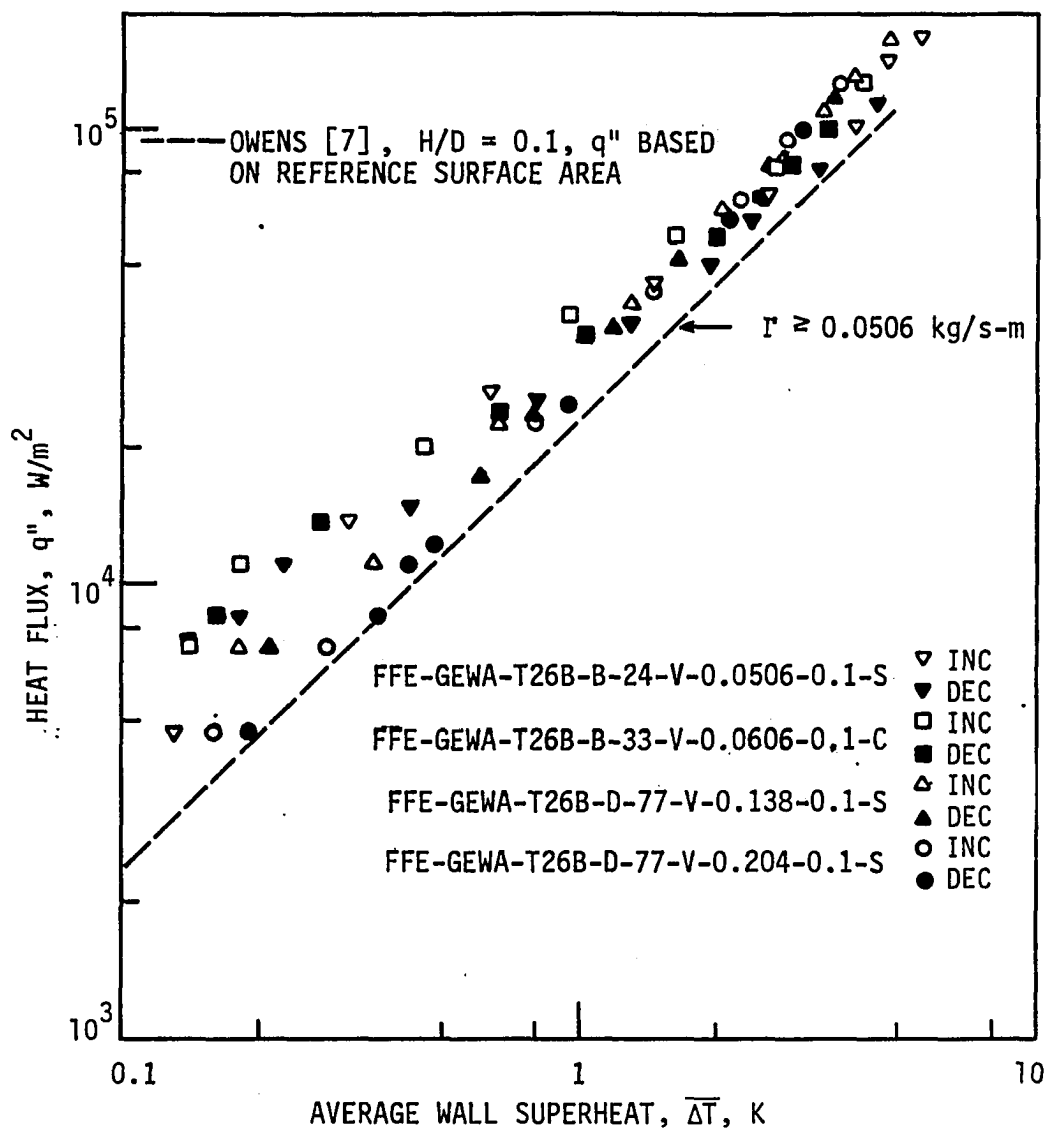


Fig. 21. q'' vs. $\bar{\Delta T}$ curves of FFE-GEWA-T26B tests

high heat transfer coefficient.

As shown by the data in Figs. 20 and 21, there is no particular effect of surface aging, surface subcooling, or way in which the heat flux is changed. Based on the total surface area of the GEWA-T surface, as provided by the manufacturer, the predicted performances were calculated according to the Owens correlation [7]. The data of both test sections lie above the predictions, particularly for the lower flow rates in the low heat flux region. This could be due to channeling of the liquid into the grooves because of surface-tension effects. The tips of the deformed fins are covered with thinned films which results in efficient heat transfer. With higher flow rates, the grooves are flooded and the outer surface has a thicker film. The decrease in heat transfer coefficient at higher heat flux is likely due to more vapor contact in the internal surface.

There is no significant difference in the performances of GEWA-T19C and GEWA-T26B, despite the difference in geometry involved. GEWA-T19C has a total surface area of $0.21 \text{ m}^2/\text{m}$ tube length, while GEWA-T26B has $0.27 \text{ m}^2/\text{m}$ tube length.

2. Effect of film flow rate

The effect of film flow rate on the falling film evaporation coefficient of a GEWA-T surface was investigated in more detail. Figure 22 presents three h vs. Re curves with constant heat fluxes. At the lowest heat flux, h decreases slightly with Re (see FFE-GEWA-T26B-0- 2.000×10^4 -V-1.0-S data) because the thickness of the film covering the surface increases with flow rate. However, contrary behavior is shown by the data at the higher heat fluxes (FFE-GEWA-T26B-B-0-1. 269×10^5 -V-1.0-S). At low flow rates, the heat transfer coefficient decreases as the heat flux

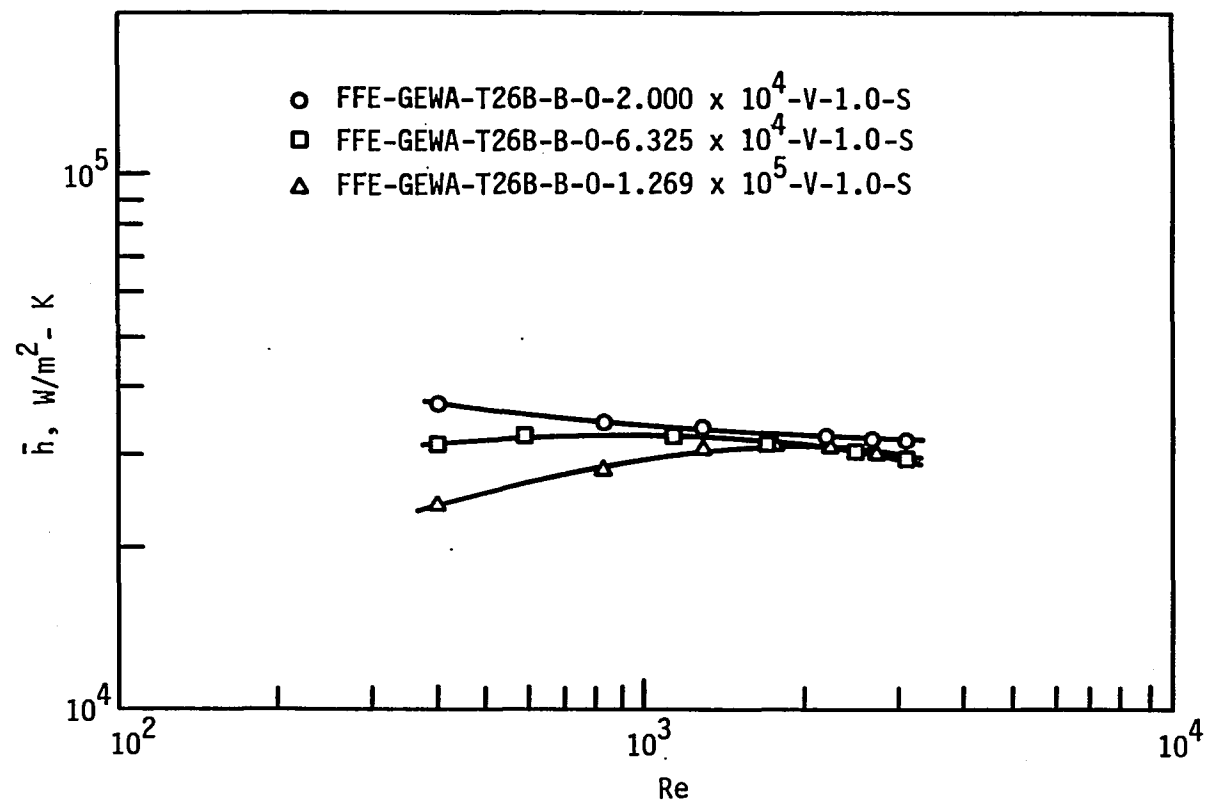


Fig. 22. Effect of film Reynolds number on the falling film evaporation heat transfer coefficient of the GEWA-T26B surface

increases. This is likely because of partial dryout of the surface due to evaporation; such dryout would first occur at the exterior surface or gaps of the T's. At high Re, there is sufficient liquid and no dryout occurred, and all the data converge to the same value of h despite the differences in q".

3. Effect of liquid feed height

The liquid feed height has a rather weak influence on the heat transfer performance of the GEWA-T surface. The data in Fig. 23 suggest that $h \sim (H/D)^{0.06}$. The bubbles formed between the distributor and the test section at small H didn't seem to affect heat transfer in the same way as in the case of the plain tube.

4. Comparison of falling film evaporation and pool boiling

Falling film evaporation and pool boiling data for the GEWA-T19C surface are compared in Fig. 24. The FFE-GEWA-T19C-B-38-V-0.0606-0.1-C data are identical to those shown in Fig. 20. The PB-GEWA-T19C-D-77-S test [70] was obtained by a test facility designed for flooded boiling tests [51]. The falling film evaporation has a higher heat transfer coefficient at low superheat due to gravity driven film convection. There seems to be a tendency for the FFE and PB data to merge at high heat flux. However, this could not be confirmed due to lack of heater power.

C. Test Section TE - Thermoexcel-E Surface

1. General heat transfer behavior

The Thermoexcel-E surface is characterized by unstable nucleate boiling at low superheat before the normal bubbling process takes place. The first-stage nucleate boiling makes the falling film evaporation data

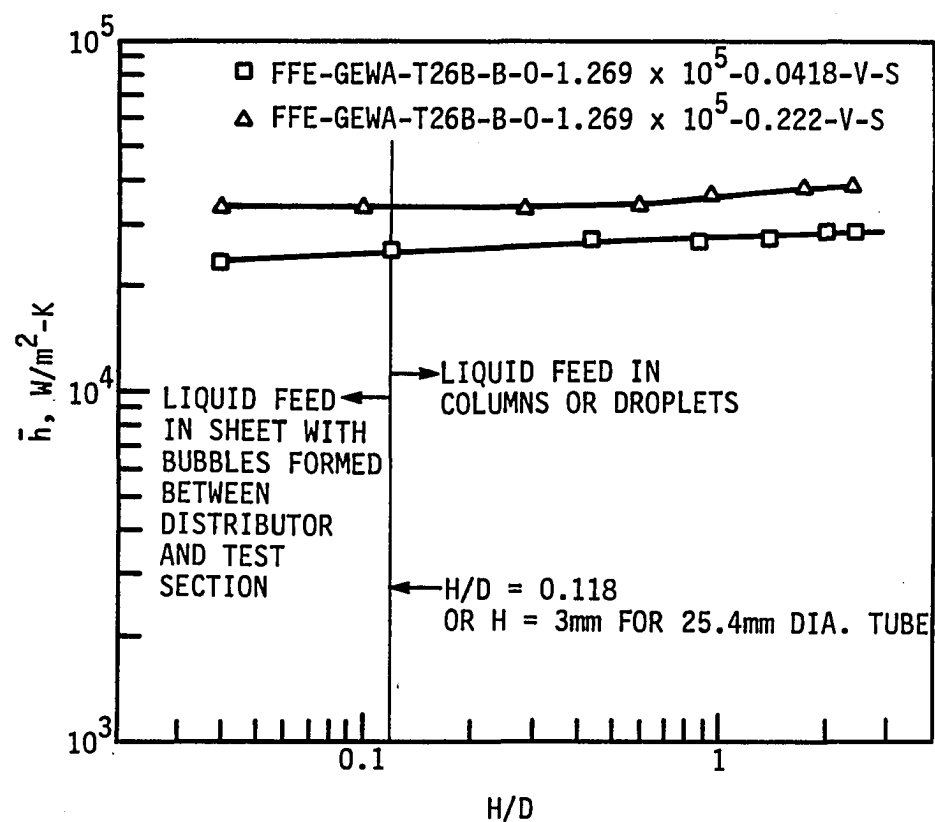


Fig. 23. Effect of liquid feed height on the falling film evaporation heat transfer coefficient of the GEWA-T-26B surface

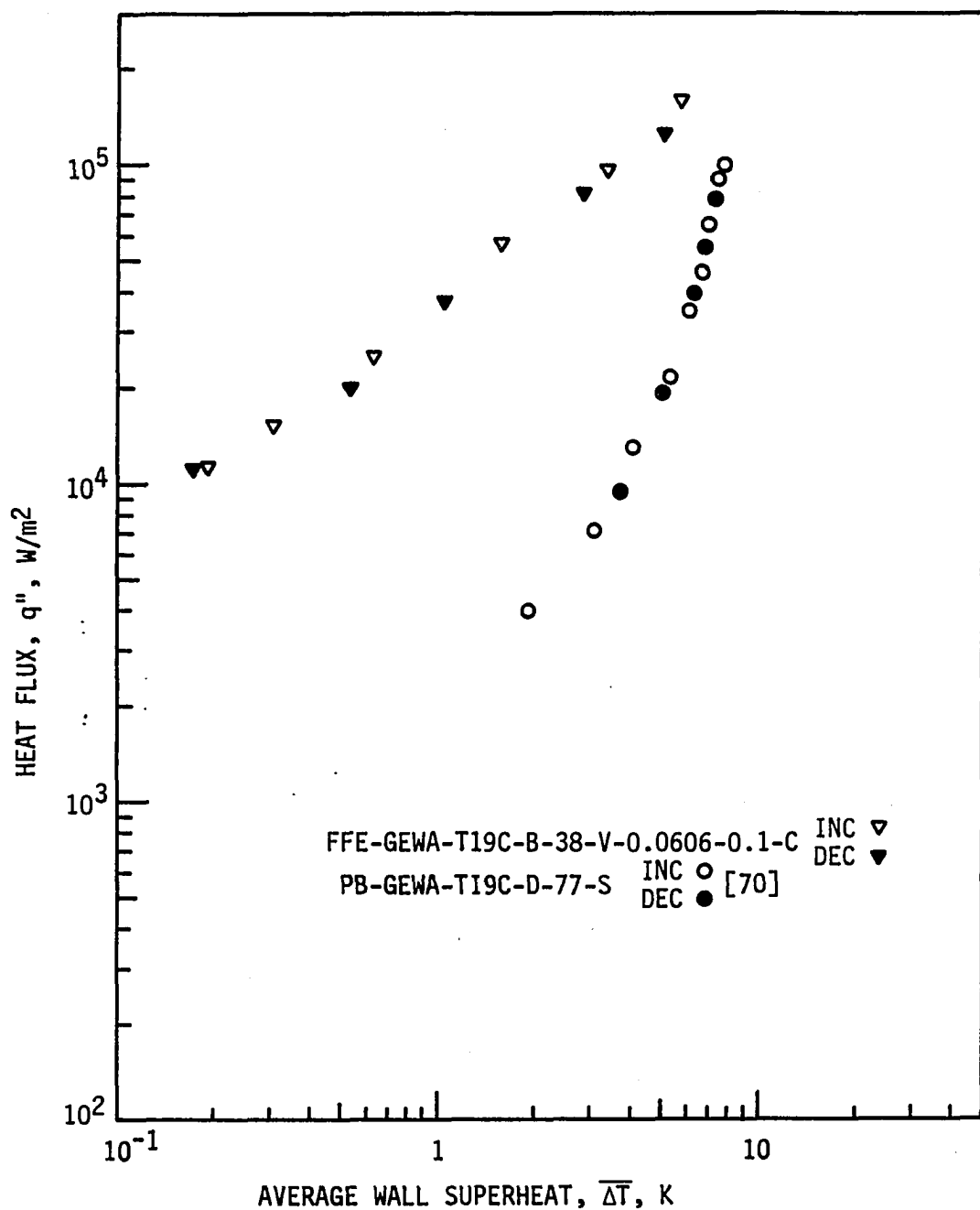


Fig. 24. Comparison of falling film evaporation and pool boiling data for the GEWA-T tube

present a steep curve at low ΔT on a q'' vs. ΔT plot. Numerous tiny bubbles were generated from the pores in the surface. Counting the bubbling sites was very difficult because of the small size and the flowing liquid film. It was estimated about 100 bubbling pores were scattered over the surface of the 152.4 mm long, 25.4 mm diameter test section. The nucleate boiling then ceased at higher heat flux, and the superheat shifted to a higher value. This was followed at higher fluxes by the generation of bubbles of larger sizes and lower frequencies, emitted also from the pores. Data then followed a stable curve for both increasing and decreasing heat flux.

As illustrated by the FFE-TE-B-65.2-V-0.0606-1.0-C data in Fig. 25, the inception of the first-stage nucleate boiling was observed at superheat as low as 0.27 K and heat flux 3.360×10^3 W/m² (point A). The data then followed a steep curve to point B, where the heat transfer coefficient was as high as 3.692×10^3 W/m²-K. The first-stage nucleate boiling persisted through point B, but died out before it reached point C. At this point, hardly any bubbles were observed and the film appeared smooth. Heat flux was increased slowly and continuously from B to C. However, no data were recorded between these two points. The temperature overshoot was carefully traced in a test to be presented in Fig. 26. Bubbles of larger sizes were not evident until $q'' = 5 \times 10^4$ W/m² or higher. After reaching the power limit at point D, the data bypassed point B and followed a different curve down to point E. The curve DE could be repeated to within ± 0.01 K by increasing or decreasing power. The FFE-TE-B-20.0-V-0.0606-1.0-S test also presented similar behavior, following the same first-stage boiling curve and decreasing traverse, but with a slightly lower point of temperature overshoot.

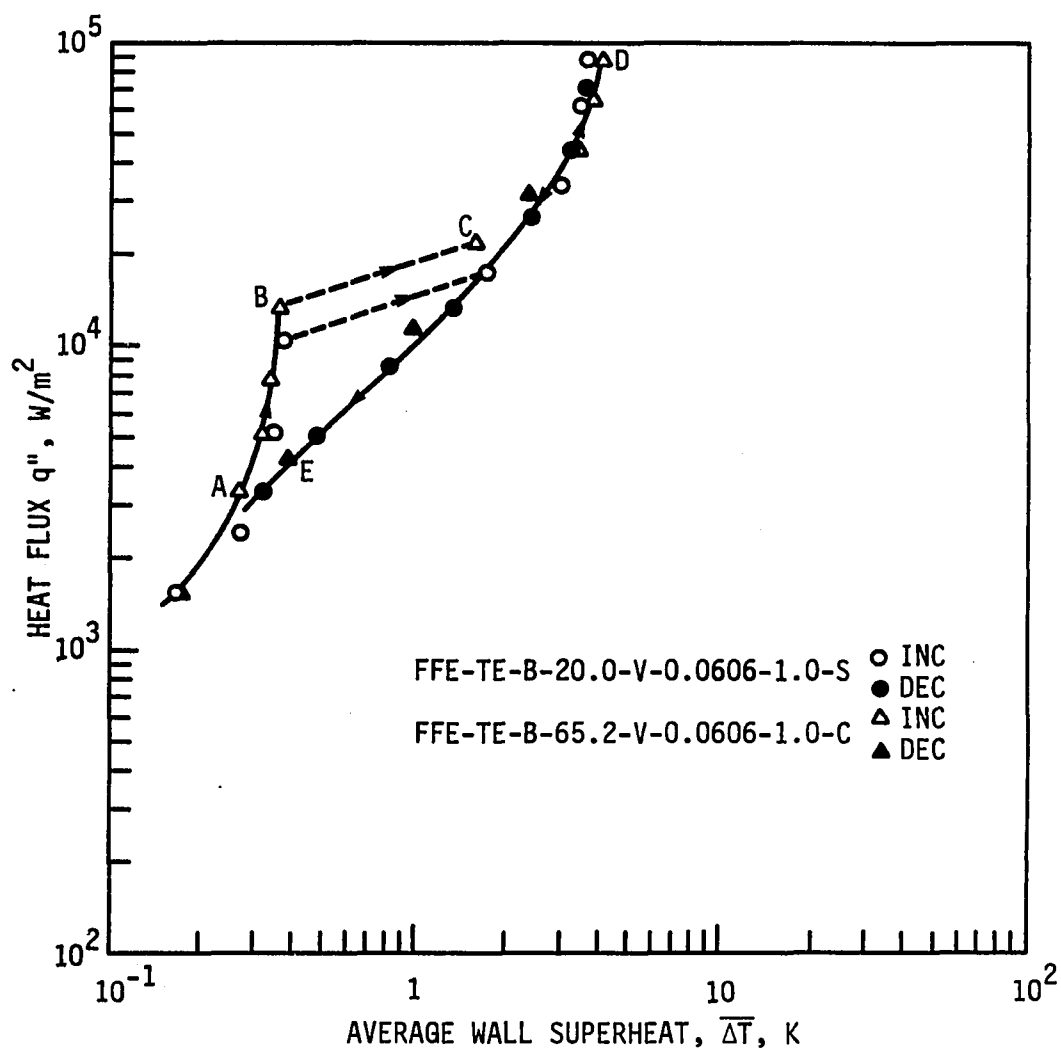
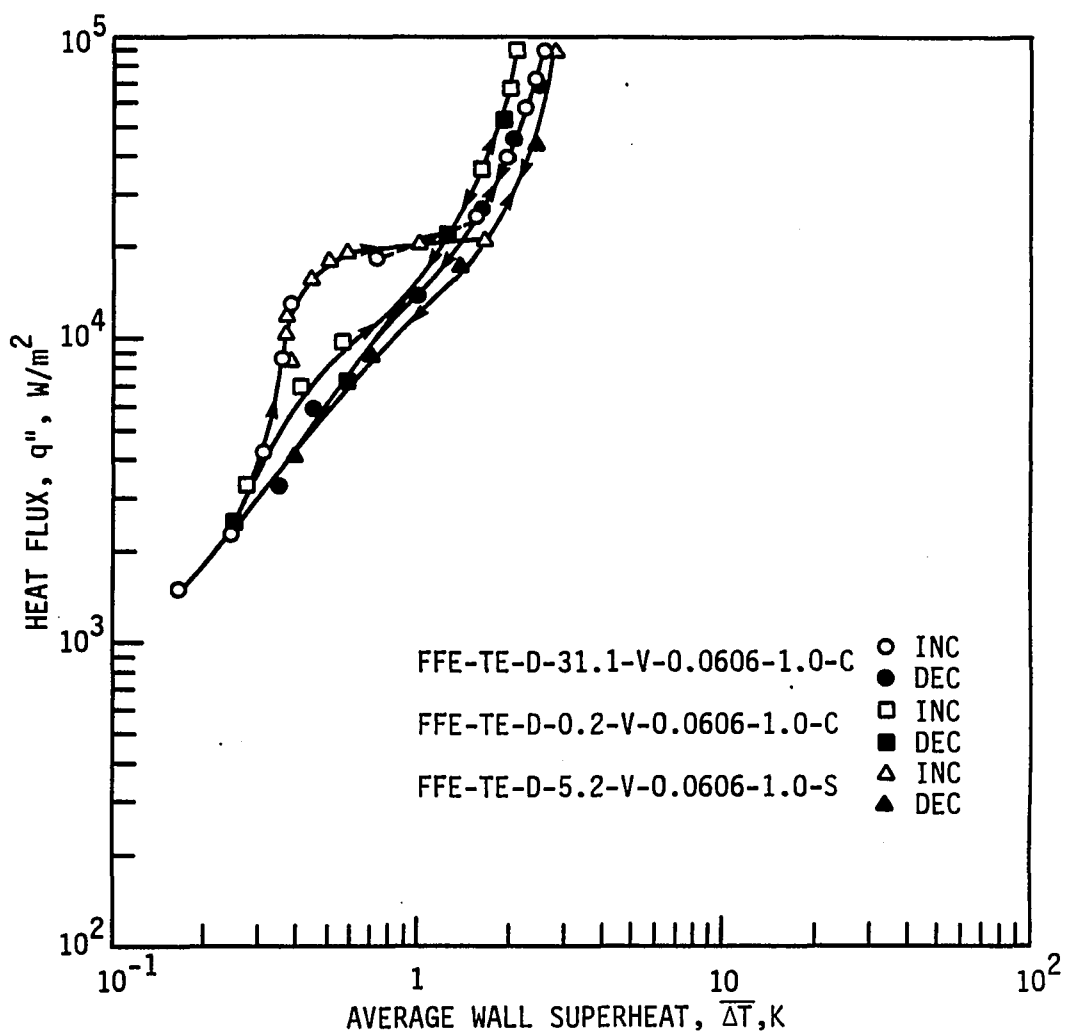


Fig. 25. q'' vs. $\overline{\Delta T}$ curves of FFE-TE-B tests

Fig. 26. q'' vs. $\overline{\Delta T}$ curves of FFE-TE-D tests

Among the FFE-TE-D tests shown in Fig. 26, the FFE-TE-D-5.2-V-0.0606-1.0-C test traced in detail the temperature overshoot due to the termination of first-stage nucleate boiling. The first-stage nucleate boiling is not affected by the methods of surface preparation, i.e., the D and B procedures. The FFE-TE-D-31.1-V-0.0606-1.0-C data follow the same first-stage nucleate boiling curve, but shift to a slightly different normal curve after the termination of nucleate boiling. The FFE-TE-D-0.2-V-0.0606-1.0-C data present a gradual drift to the normal curve during the increasing traverse, with only weak first-stage nucleate boiling observed. The population of nucleation sites was significantly smaller than the other tests. The data of each D-test follow different normal curves after first-stage nucleate boiling. The difference among the normal heat transfer coefficients evaluated at constant q'' for the D-tests can be 27 percent, as shown by the data of FFE-TE-D-0.2-V-0.0606-1.0-C and FFE-TE-D-5.2-V-0.0606-1.0-S tests, while comparing Figs. 25 and 26, the difference between those of the D and B tests can be as great as 80 percent. It is clear that the D preparation provides higher normal heat transfer coefficients than the B preparation.

2. Flooded tests

Owing to the extraordinary behavior of the Thermoexcel-E surface, further tests were performed in the flooded mode. The pool boiling curves for Test Section TE are shown in Figs. 27 and 28. The first-stage nucleate boiling was evident in all the tests. High frequency, tiny bubbles were observed at heat fluxes above $6.509 \times 10^2 \text{ W/m}^2$. In the PB-TE-D-51.4-C test, the increasing data depart from the first-stage nucleate boiling curve at lower heat flux, and proceed gradually toward the normal boiling

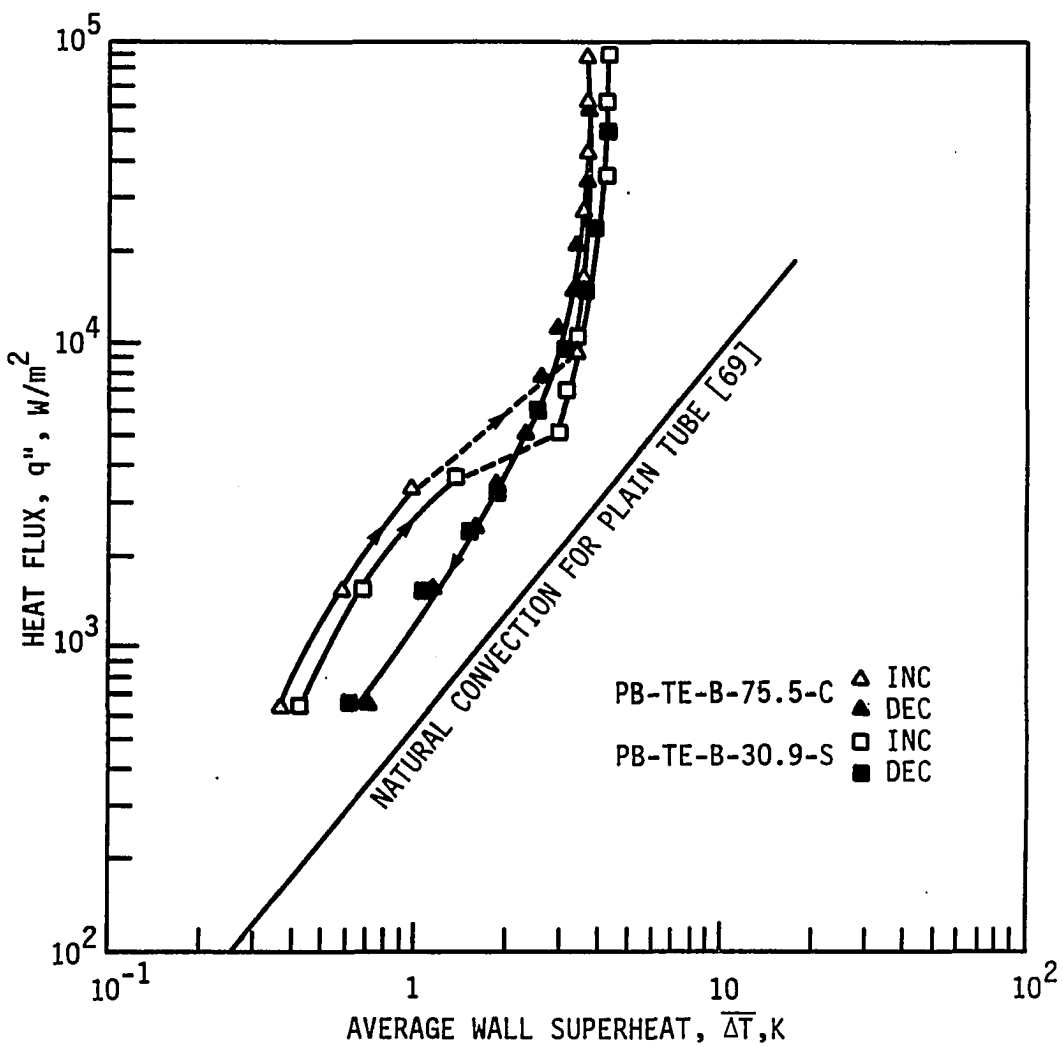


Fig. 27. PB-TE-B curves

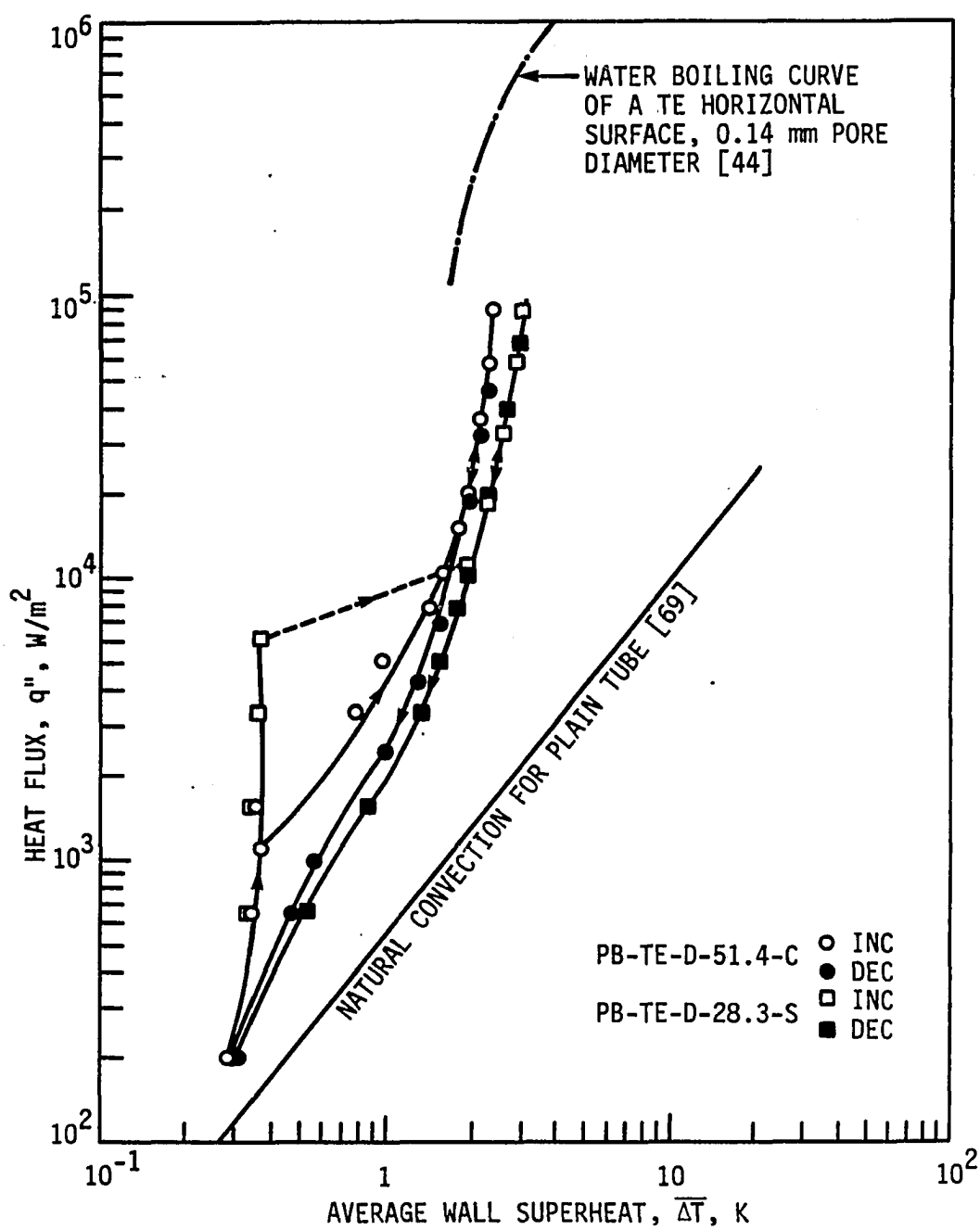


Fig. 28. PB-TE-D curves

curve. The PB-TE-D-28.3-S data show that the first-stage nucleate boiling was sustained through $q'' = 6.068 \times 10^3 \text{ W/m}^2$ before it shifted to the normal curve. The first-stage nucleate boiling in the B-tests appeared to be weaker than in the D-tests, and the approach to the normal boiling was more gradual. For all the PB tests, bubbles of larger size and lower frequency were observed immediately after the termination of first-stage nucleation. The number of bubbling sites on the surface increased with heat flux. Bubbling did not completely terminate until q'' dropped to 10^3 W/m^2 or lower. As for the falling film evaporation, the D preparation provided higher normal boiling coefficients than the B preparation. Also, the C-tests showed higher coefficients than the S-tests. The tests with higher surface subcooling resulted in higher normal coefficients in the pool boiling tests. The difference in coefficients due to the combination of these effects can be as great as 80 percent.

Also presented in Figure 28 is a pool boiling curve of water of a Thermoexcel-E surface [44] for the purpose of comparison. The curve is close to the present normal boiling curves even though it is based on the data of a horizontal surface with larger pore diameter. The procedure of surface preparation and heat flux increase rate for this boiling curve is not clear.

An additional test was run to ascertain that the first-stage nucleate boiling was not due to the gas content in the water. The water pool was degassed by boiling with auxiliary heaters for three hours (two hours longer than the ordinary procedure) before the PB-TE-D-71.1-C test began. The first-stage nucleation at low heat flux was observed as usual. By setting the flux at $1.329 \times 10^4 \text{ W/m}^2$, the wall superheat kept constant at

0.38 K for four hours until the test terminated. Long-term falling film evaporation tests also showed no change in the first-stage nucleate boiling data.

Based on the data for both FFE and PB tests so far, generally it can be concluded that D-tests show higher normal heat transfer coefficients than B-tests, and C-tests higher than S-tests. Greater surface subcooling results in higher coefficients in flooded tests; however this is not necessarily true for falling film evaporation tests.

3. Mechanism

A qualitative model of the heat transfer mechanism was developed in order to explain the behavior of the Thermoexcel-E surface. The normal mechanism of boiling heat transfer on porous surfaces with continuous cavities and intermittent openings such as thermoexcel-E has been studied by Nakayama et al. [44,47,48]. Evaporation of liquid films inside the tunnels, which have a large internal surface area, is the major contribution to the heat transfer enhancement. The dynamic cycle includes bubble ejection through the pores and suction of liquid into the tunnels. However, as the power is first raised, there must be some different mechanism involved to account for the first-stage nucleate boiling observed in the present study.

It is probable that there are numerous good cavities entrapping inert gas or vapor on the internal walls of the tunnels, shown in the cross-sectional view of the surface in Fig. 3. Nucleate boiling can start at very low superheat as these cavities or recesses are likely to be relatively large in size. At this time bubbles are generated somewhere inside the tunnels and escape through the pores. The tunnels are pretty

much saturated with liquid, and there is no internal film evaporation taking place. As the heat flux rises, the bubble generation rate increases, as does the vapor volume or void fraction inside the tunnels. Gradually the bubbles agglomerate into large vapor pockets. The large vapor pockets stay in the tunnels and only small bubbles can escape out of the tunnels through the pores. As more bubbles join the vapor pockets, fewer bubbles are observed to emerge through the pores. Eventually, the vapor pockets coalesce into a vapor core surrounded by a liquid film on the internal wall of the tunnel. All the vapor phase generated goes to the vapor core and no bubbles are observed from outside. An energy balance is reached among film vaporization, condensation near the tunnel openings, and conduction through the structure. This illustrates the situation when first-stage nucleate boiling terminates. This is supported by the higher heat transfer coefficient than that for a plain tube. If it were a case of cavities saturated with vapor without latent heat transport, the heat transfer coefficient would be similar to, or perhaps even lower than those for the plain tube.

As the heat flux is further increased, the internal pressure of the vapor core increases due to high vapor generation rate and overcomes the surface tension. Bubbles larger than those observed in the first-stage boiling are pushed out through some of the pores at a low frequency, while liquid is sucked into the tunnels through the other pores to replenish the film. This is the normal heat transfer mechanism of the Thermoexcel-E surface.

It is believed that nucleate boiling inside the tunnels still plays a role in the normal mode of heat transfer. The nucleation sites in the

first-stage nucleate boiling can persist through the change of heat transfer mode, and there must be nucleate boiling in the liquid film. The vapor generated through internal nucleate boiling joins the vapor core inside the tunnel. The D preparation dries out the surface and saturates cavities with air, while the B preparation depletes the air entrapped in the cavities before the tests. Hence, the D preparation provides the surface with more active nucleation sites of all sizes, and higher heat transfer coefficients are observed than with the B preparation.

The way of changing heat flux affects the normal coefficient by preserving or snuffing out nucleation sites. As noted above, the normal heat transfer mechanism includes vapor mass ejection through some of the pores and liquid suction into the tunnels through the others. If the heat flux is increased slowly and continuously, the vapor generation rate inside the tunnels rises slowly, and a drastic change in the suction flow rate is less likely to happen. However, if the flux is changed stepwise, the vapor generation rate must rise steeply, and causing a surge of cold flow rushing into the tunnels which snuffs out some active or potential nucleation sites. Therefore, in the C tests for both FFE and PB, more nucleation sites are preserved and higher normal heat transfer coefficients are observed than in the S tests.

4. Comparison of falling film evaporation and pool boiling

Pool boiling tests were performed immediately following the falling film evaporation tests to examine the relationship between the two modes of heat transfer. Fig. 29 presents two series of curves, each having a complete increasing-decreasing FFE curve, followed by a decreasing PB curve. The PB tests were run by raising the power to the limit immediately

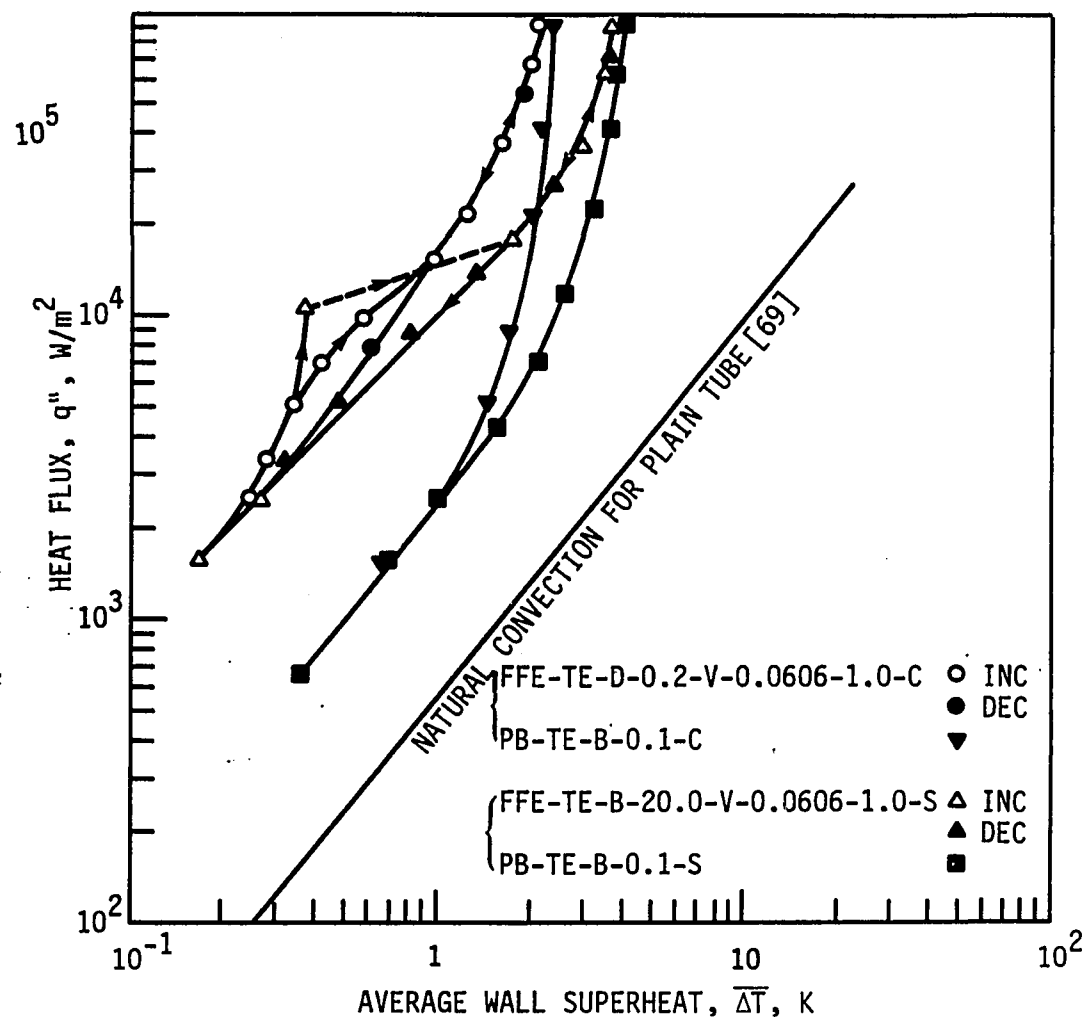


Fig. 29. Comparison of the falling film evaporation and pool boiling for the Thermoexcel-E surface

following the FFE tests, shifting to the PB mode, and then taking data as the power decreased. Therefore, basically, the FFE and PB data are compared with the same number of nucleation sites on the surface because all the nucleation sites had not been snuffed out or quenched during the FFE-PB transfer. The relative positions of the FFE and PB normal curves in each series are about the same. The PB curves are always to the right of the FFE curves, and the tendency to converge at high heat flux is clear. This agrees with the qualitative results with a vertical plate with Thermoexcel-E surface [49]. The pool boiling heat transfer coefficients at low heat fluxes are higher than the other PB tests because the auxiliary heater beneath the test section was not completely shut off during the test. Heat transfer was promoted by the upward convection currents.

5. Effects of film flow rate and liquid feed height

The effects of changing flow rate and liquid feed height on the heat transfer performance of the Thermoexcel-E surface were also investigated. Tests were run by varying film flow rate and feed height at several heat flux levels. Figs. 30 and 31 each contain three curves, two at a low heat flux and the other at a high flux. The two low flux curves show differences in the heat transfer coefficient because they correspond with two regimes, the first-stage nucleate boiling and the normal boiling, respectively. The high flux curve is, of course, obtained in the normal boiling mode.

Both Re and H/D have rather weak influences on the heat transfer when boiling is significant, as shown by the low flux curves at the first-stage boiling and the high flux curves at the normal boiling. It was reported that the heat transfer coefficient was nearly independent of the film flow

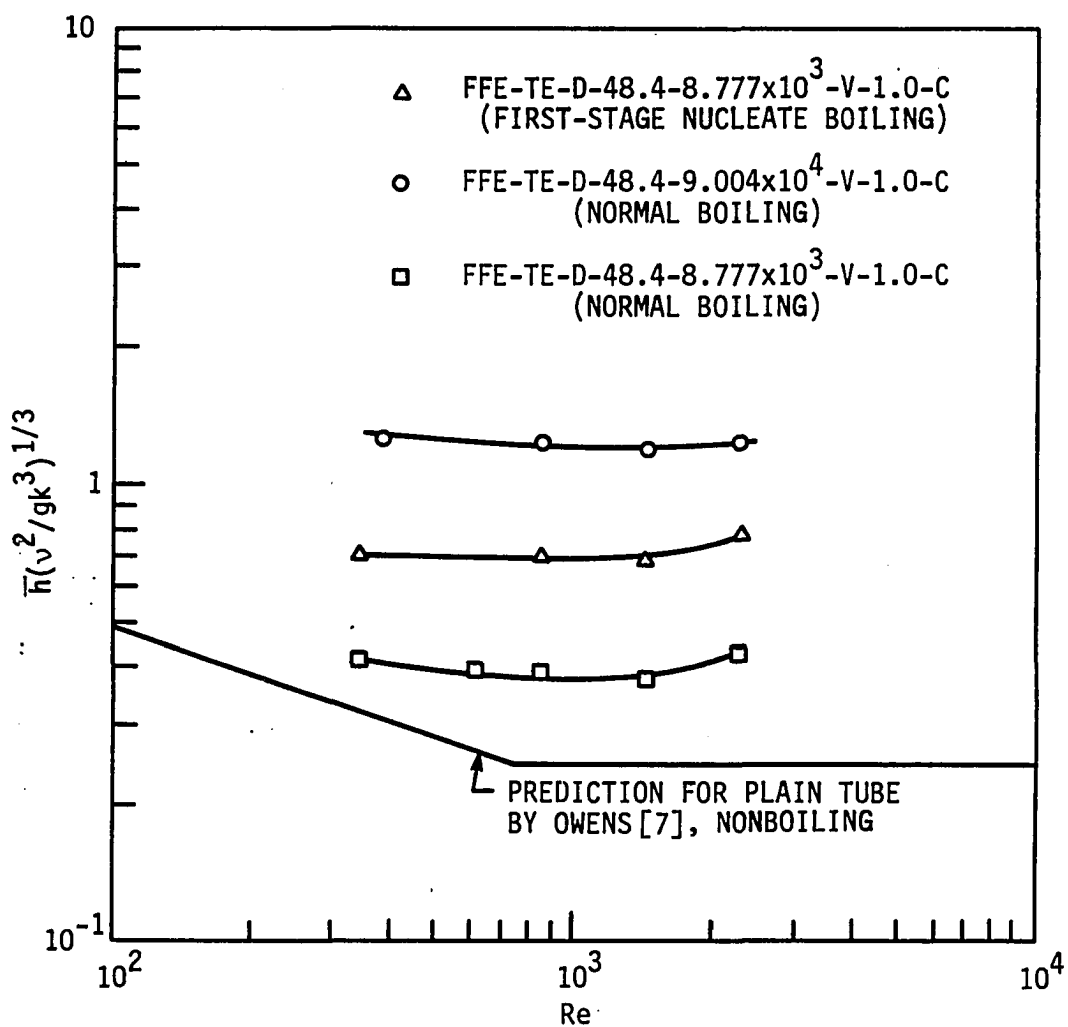


Fig. 30. Effect of film Reynolds number on the falling film evaporation coefficient of the Thermoexcel-E tube

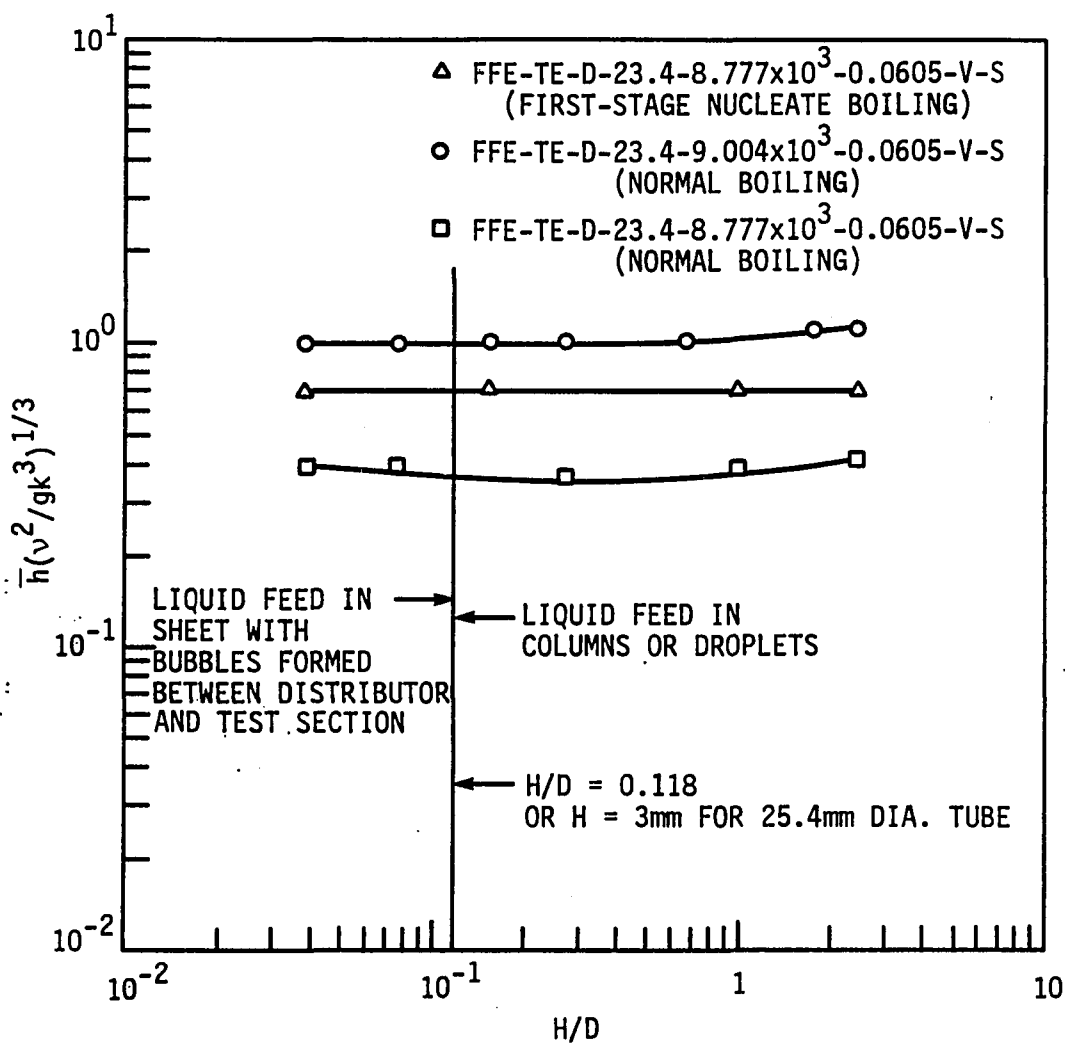


Fig. 31. Effect of liquid feed height on the falling film evaporation coefficient of the Thermoexcel-E tube

rate on a vertical plate with the similar structured surface [49]. The influences are stronger at low heat flux when boiling is minor, as shown by the other low flux curves in the normal mode. The bubbles generated between the distributor and the test section have little effect on film flow over the Thermoexcel-E tube.

6. Summary

Based on the data and the understanding of the characteristics of the Thermoexcel-E surface so far, a semi-schematic summary plot can be put forward. As shown in Fig. 32, there are a first-stage nucleate boiling curve, a group of FFE curves, and a group of PB curves. The solid curves are duplicated from some of the data curves presented in Figs. 25-28, while the dotted curves are speculative and must be verified by further experiments. The first-stage boiling data of both FFE and PB were found to follow the same curve. This serves as evidence that the first-stage nucleation is not influenced by the mode of heat transfer. The nucleate boiling accounts for most of the heat transfer, and is not affected by the way liquid is fed to the surface. The groups of FFE and PB curves are each bounded by a pair of curves representing the highest and the lowest heat transfer coefficients, based upon the data obtained in the present study. However, still higher or lower data might be realized through different manipulations of the surface. Normal curves can be observed anywhere within the boundaries, depending on the nucleation characteristics of the surface. The D and C curves tend to lie more to the left, while the B and S curves lie more to the right. Data can shift from any point on the first-stage nucleate boiling curve to one of the normal curves during the increasing traverse, with the mechanism discussed before. For each FFE

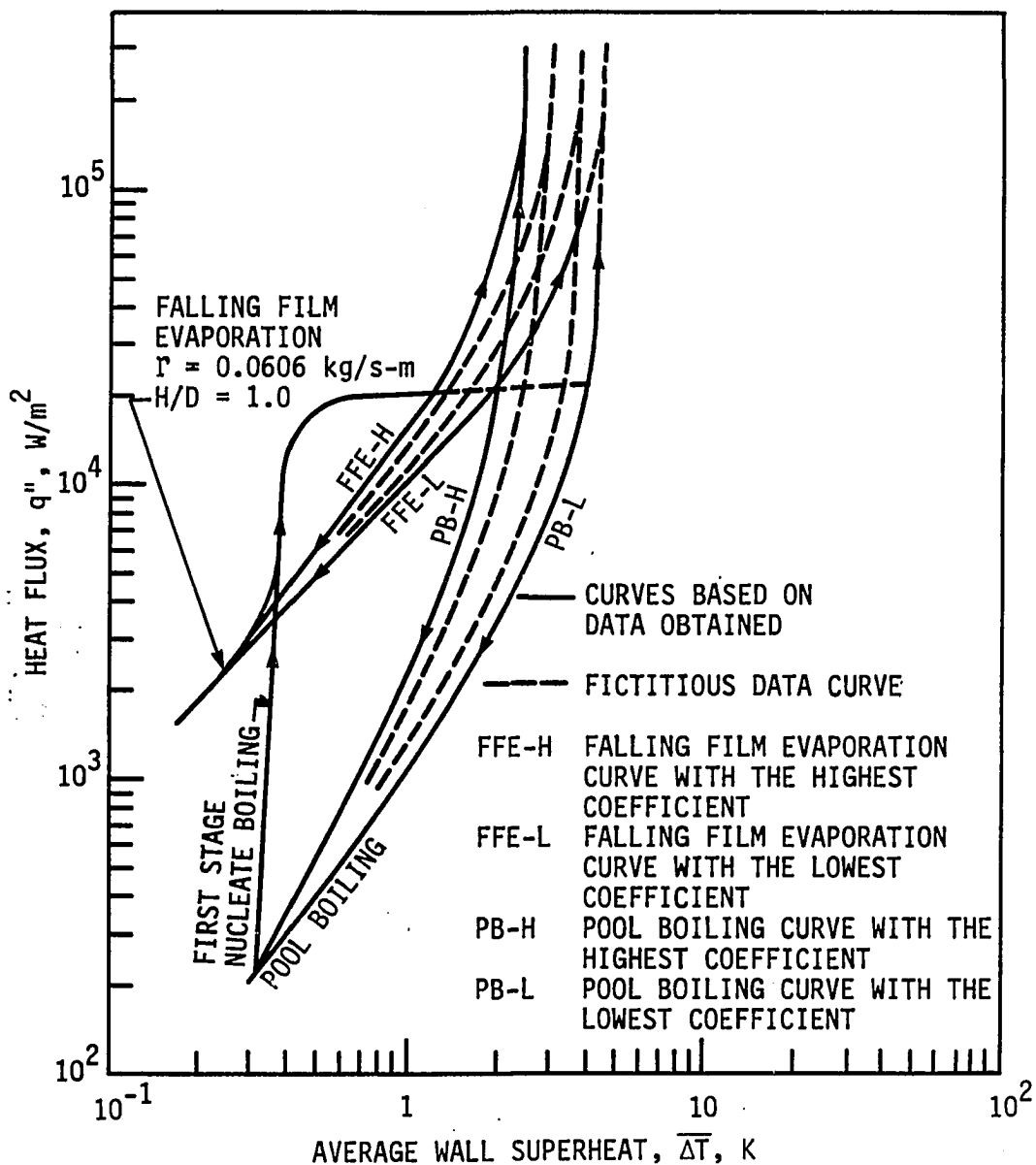


Fig. 32. Summary plot for the Thermoexcel-E surface

curve, there is a corresponding PB curve. It is expected that the pair converges to the same curve at higher heat flux when boiling is fully established and dominant.

The FFE curves presented here are obtained at $\Gamma = 0.0606 \text{ kg/s-m}$ and $H/D = 1.0$. Curves are subject to change at different Γ 's or H/D 's. However, as it was shown in Figs. 30 and 31, the change will be minor and only in the low heat flux range. The data at high heat flux will remain the same.

D. Test Section HF - High Flux Porous Surface

1. General heat transfer behavior

As shown in Figs. 33 and 34, the convective portions of the FFE-HF curves are quite similar to those of the smooth tube curves given in Figs. 14 and 16. The heat transfer coefficients are slightly lower, however, because the heating surface is covered by a layer of porous matrix saturated with stagnant liquid. This layer constitutes an extra thermal resistance, that apparently compensates for the increased surface roughness. At higher heat fluxes, tiny bubbles were generated at high frequency from the many nucleation sites provided by the porous coating. A similar observation was made in previous pool boiling tests [51]. The water film was smooth in appearance, because the small bubbles did not disrupt the film as much as the large bubbles generated on the other structured surfaces.

The boiling curves of the High Flux porous surface treated with the B aging procedure show significant hysteresis, irrespective of flow rate, as depicted in Fig. 33, while the data of the D-tests shown in Fig. 34 present

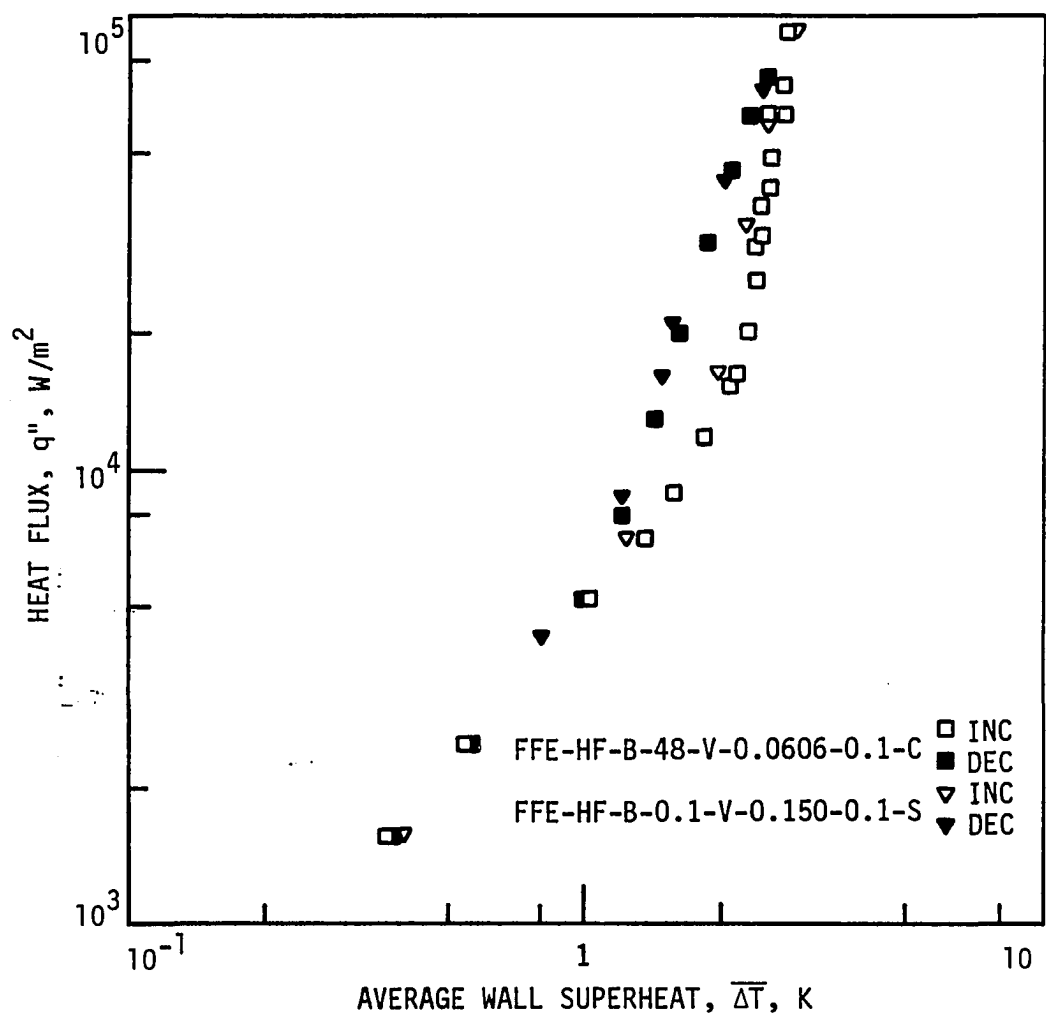


Fig. 33. q'' vs. $\bar{\Delta T}$ curves of FFE-HF-B tests

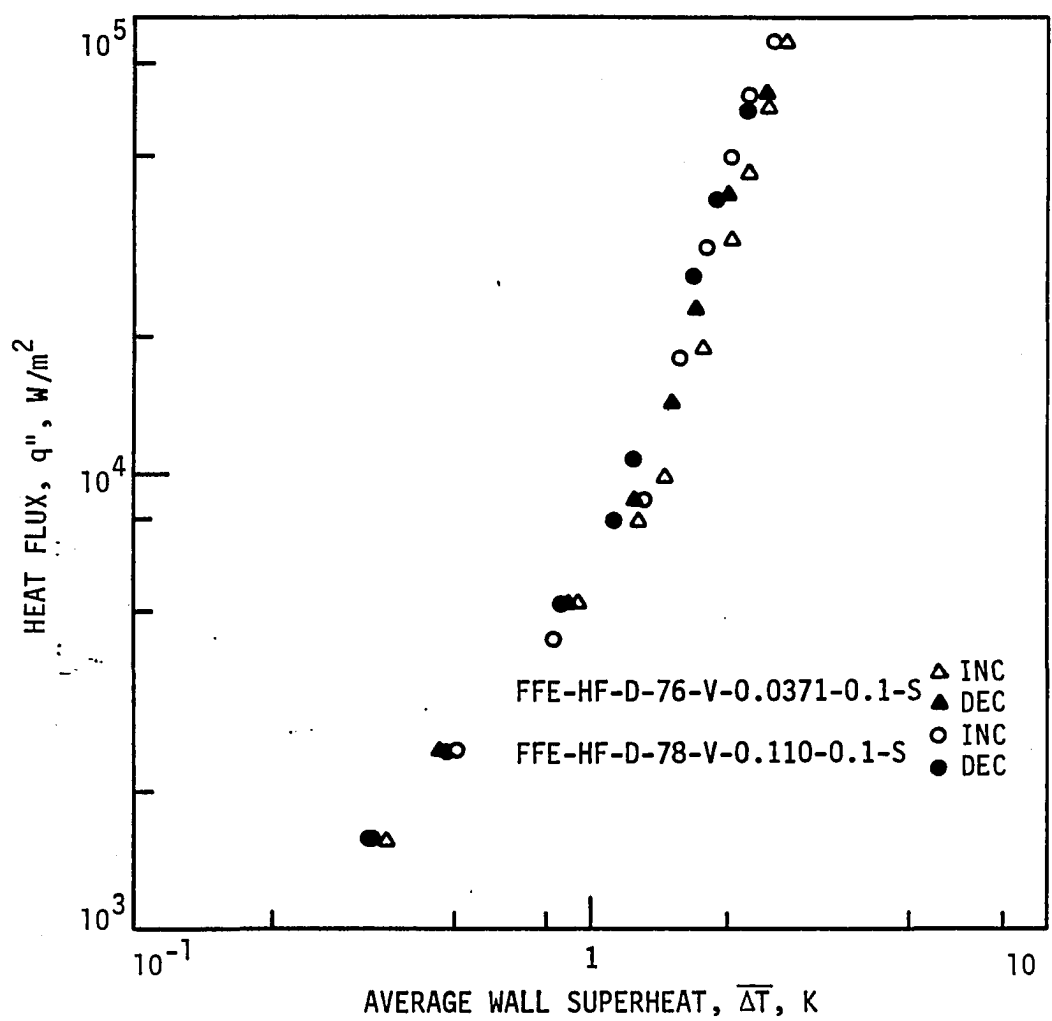


Fig. 34. q'' vs. $\bar{\Delta T}$ curves of FFE-HF-D tests

a much smaller hysteresis. Subcooling does not appear to be an important variable. The B-tests show an upswing in the increasing traverse at about 2 K superheat which is considered as the point of incipient boiling. The points of incipient boiling at lower superheats of about 1.3 K in the D-tests suggest that more and larger nucleation sites are available than in the B-tests.

When the porous surface is pre-boiled and subcooled, the inert gas content of pores within the metallic matrix is depleted and vapor is condensed. The number of active nucleation sites available is thus reduced. As the heat flux increases, nucleation is triggered at a higher than expected superheat. There is, however, no reduction in superheat, as was observed in the case of pool boiling with the High Flux surface [51]. The data simply exhibit a change in slope due to the high h 's realized by nucleate-boiling. Apparently, inactive sites are quickly activated once vapor is generated in the matrix. The nucleation sites tend to remain active; therefore, the decreasing curve has lower superheats than the increasing curve. This explanation is supported by the visual observation of the bubble generation during the tests. The D aging procedure can saturate with air every cavity that serves as a nucleus for bubble generation. Since the air cannot be condensed at lower temperature, the surface subcooling does not affect the performance. During the increasing traverse, the surface has more active nucleation sites than in the B-tests; however, the number of sites may be still less than in the case of the normal decreasing curve. In any case, the hysteresis is greatly reduced by having more active nucleation sites available in the increasing traverse in the D-tests. The established boiling curves in which the heat flux is

decreasing are very close for all the B- and D-tests as shown in both Figs. 33 and 34, because the density of nucleation sites for the decreasing curves is about the same.

2. Effect of film flow rate

The flow rate seems to have little effect on heat transfer performance judging from the low heat flux data in Figs. 33 and 34. This effect was further investigated by varying the flow rate in the range from 0.0210 to 0.163 kg/s-m (film Reynolds number from 297 to 2303). Several heat fluxes were considered and the feed height was fixed. As shown in Fig. 35, the heat transfer coefficient is insensitive to Re at high heat fluxes where nucleate boiling takes place. The influence is more significant at low heat flux where heat transfer is dominated by convection.

3. Effect of liquid feed height

The influence of liquid feed height on the heat transfer performance again depends upon the dominant mode of heat transfer. As shown in Fig. 36, the heat transfer coefficient is essentially constant throughout the range of H/D at high heat flux, while it behaves more like a non-boiling smooth tube at low heat flux. The same relationship as for the smooth tube is observed, i.e., $h \sim (H/D)^{0.1}$.

4. Comparison of falling film evaporation and pool boiling

In order to compare the performances of the two modes of heat transfer, pool boiling tests were performed immediately following the falling film evaporation, with the procedure as described in section V-A-4. As shown in Fig. 37, FF data merge into the PB fully-established curve at medium heat flux. Nucleate boiling apparently dominates the heat transfer for heat flux higher than that point, and the performance is no longer

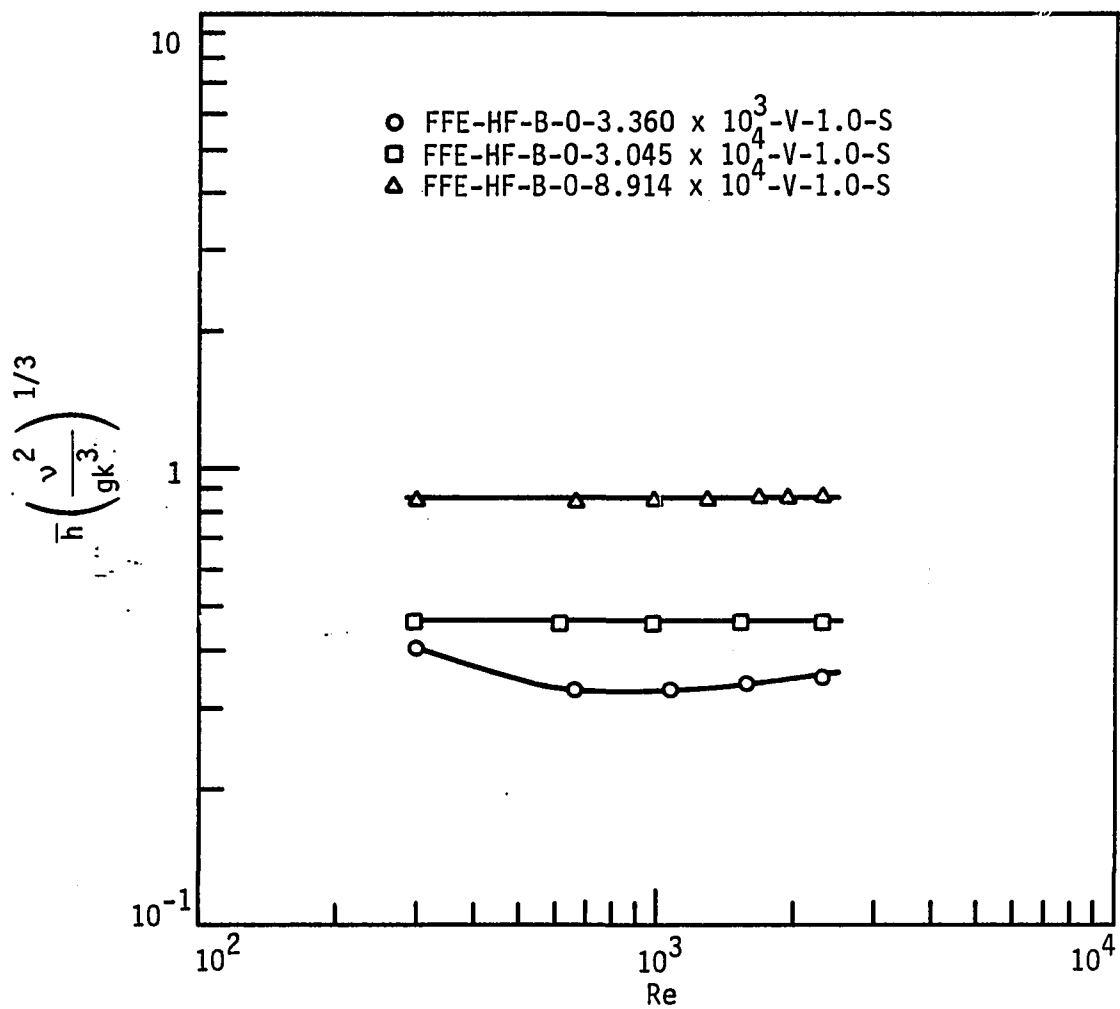


Fig. 35. Effect of film Reynolds number on falling film evaporation coefficient of the High Flux surface

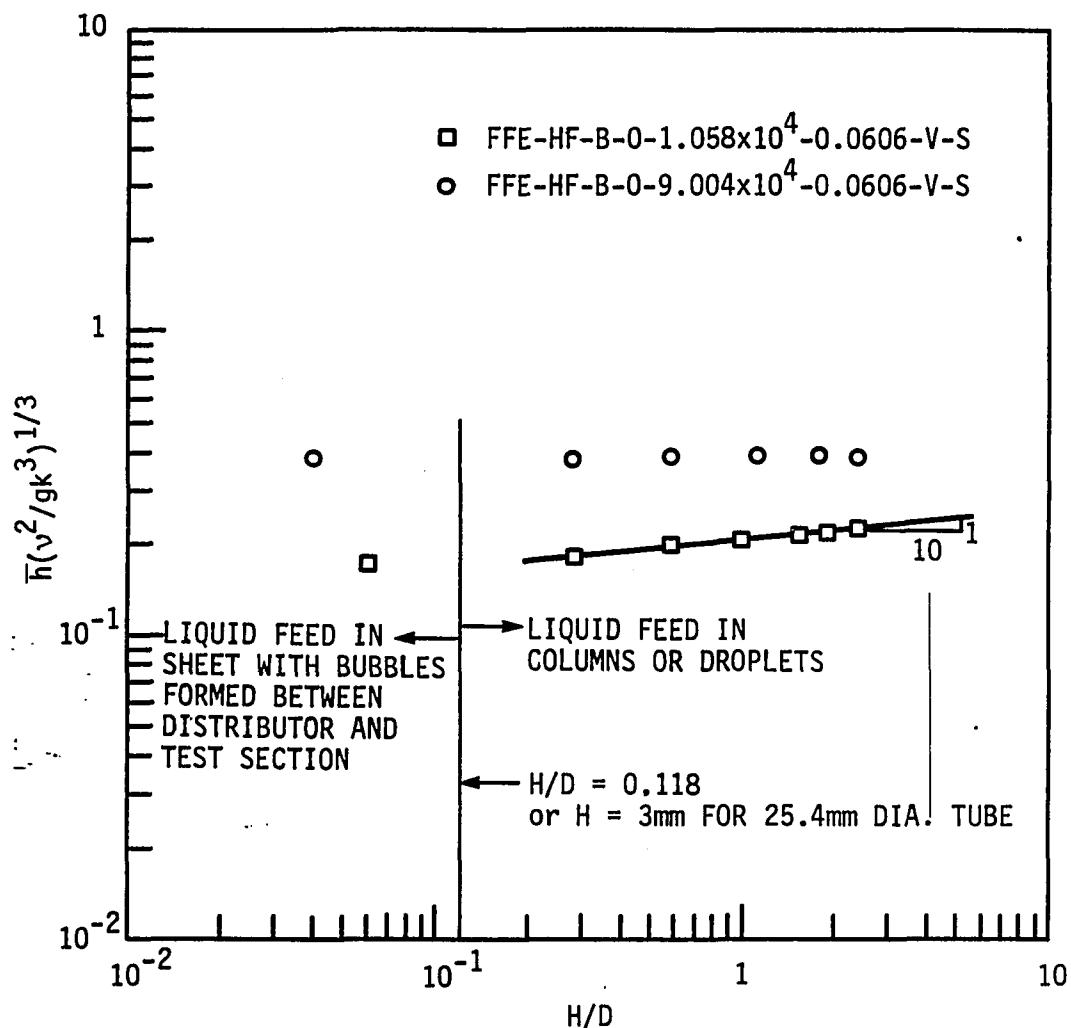


Fig. 36. Effect of liquid feed height on the falling film evaporation coefficient of the High Flux surface

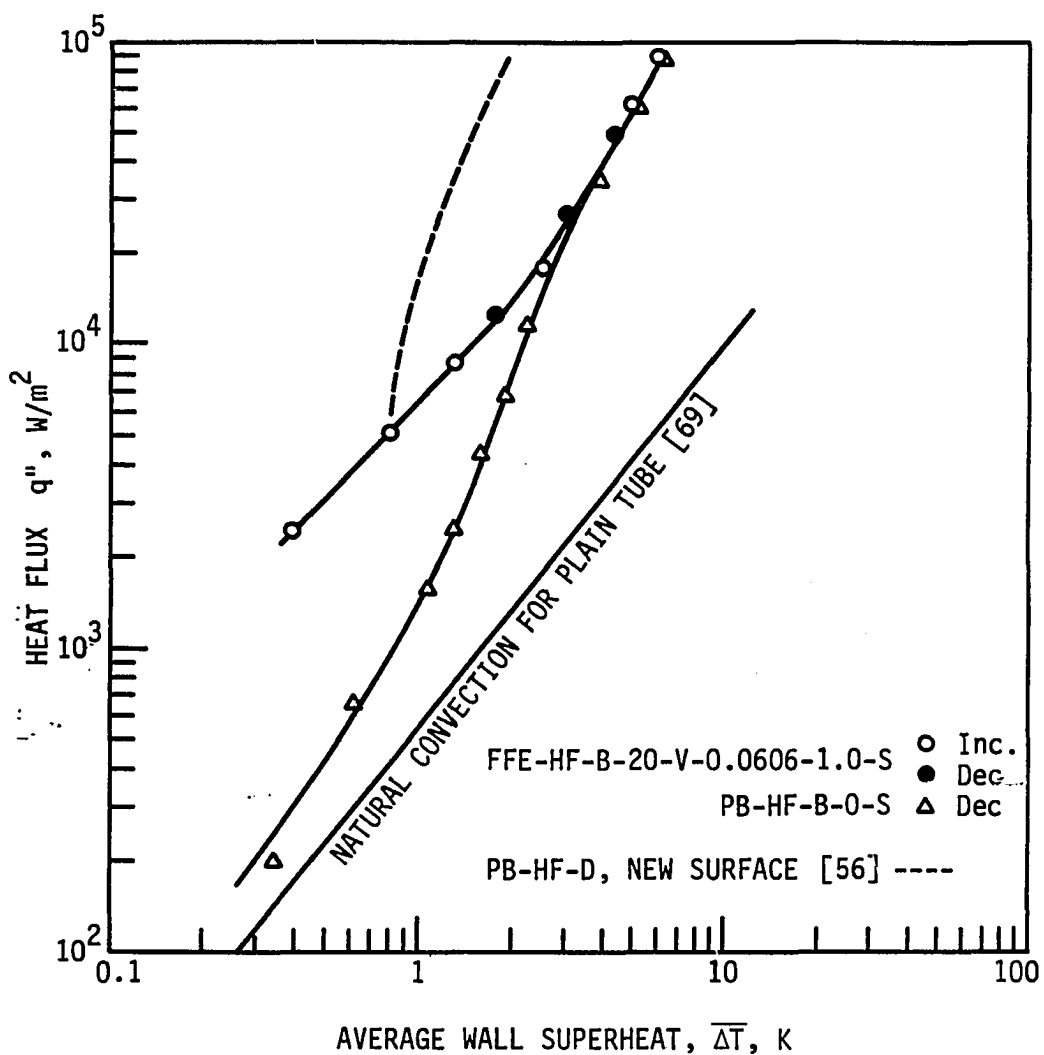


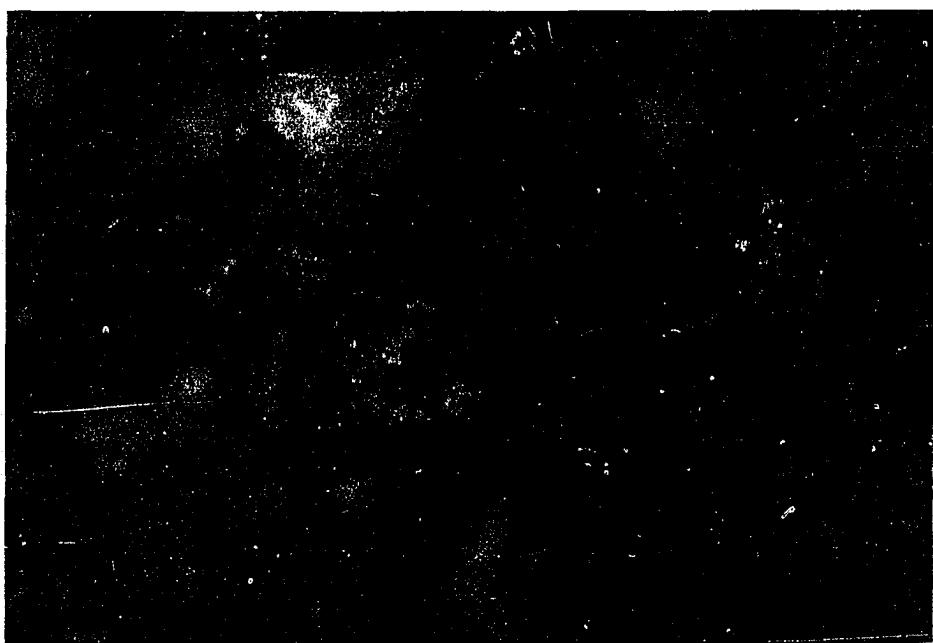
Fig. 37. Comparison of the falling film evaporation and the pool boiling performances of the High Flux surface

affected by the way liquid is supplied to the surface.

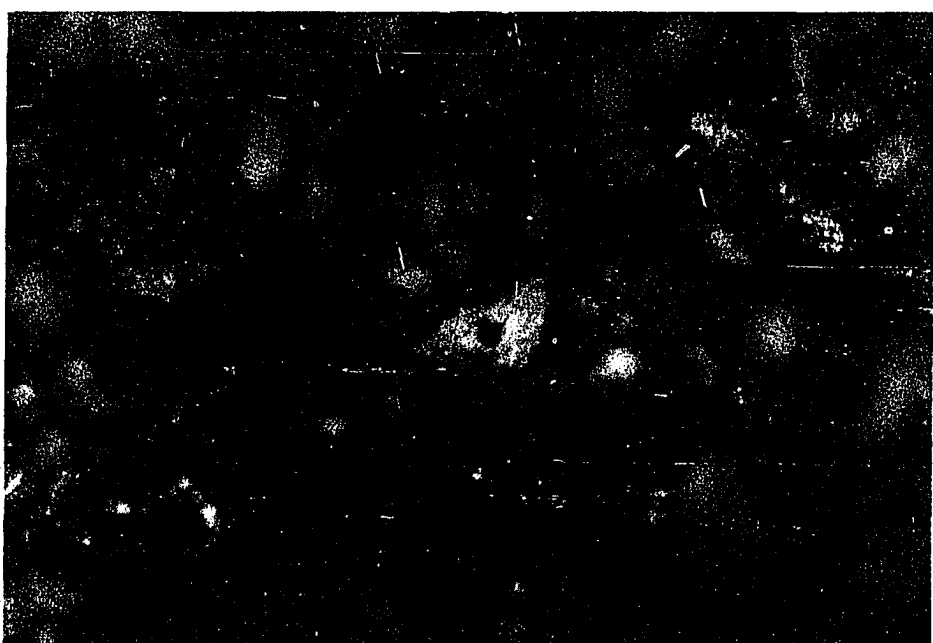
5. Fouling

Also compared in Fig. 37 is the PB curve obtained when the tube was new [56]. The present data show a substantial degradation in the performance. This reveals a vulnerability of the porous heat transfer surfaces. As examined through a microscope, crystals were observed in almost every pore on the porous surface. The internal surfaces of the pores were literally covered by white crystals, such as the pore shown at the center of Fig. 38 (a). The mouth of this pore is apparently restricted. The crystals were observed to cover the entire internal surface down to the bottom as the focus plane moved deep down. Some pores were observed to have more crystals than the others. The pore shown in Fig. 38 (b) has so much crystal build up that only a narrow passage can be seen, while the pore at the center of Fig. 38 (c) is completely clogged.

A degradation in coefficient of falling film evaporation with boiling on a plain tube to approximately 30 percent of the initial value in seven hours was observed by Parken [12]. Fouling of a High Flux surface has been observed in a spray evaporator intended for an ocean thermal energy conversion (OTEC) power system [32]. White crystalline material identified as bayerite or hydrated beta aluminum hydroxide Al(OH)_3 , with a small amount of iron oxide, was found embedded in the porous surface nucleation sites. The deduced ratio of boiling coefficients (fouled/clean) was 0.45, compared with the present data of from 0.33 to 0.41, depending upon the superheat. It was suspected that the fouling was produced by prolonged exposure of the unprotected tubes to a warm humid marine atmosphere. An alternative possibility was a chemical reaction between aluminum and



(a)



(b)

Fig. 38. Fouled High Flux porous surface (160X)



(c)

Fig. 38. (continued)

ammonia in the presence of a small amount of sea water. To do a complete analysis of the problem, it was suggested that the entire history of the surface, from initial fabrication through final employment and testing, must be taken into account. In the present tests, five test sections of the same material were tested in the same system. Why was noticeable scaling observed only with the High Flux surface?

In order to approach the problem, the scale itself had to be analyzed. However, as shown in Fig. 38, most of the crystals were within the pores. An attempt was made to pick up a sample with a piece of adhesive tape, but an insufficient amount for analysis could be collected in this way. An adequate sample was finally acquired by washing the tube in an ultrasonic cleaner filled with distilled water. The water was maintained at 65°C by the built-in side heater. The aqueous solution was then concentrated by vaporization in a drying oven. The residue analyzed by the X-ray diffraction technique was found to consist of both water-soluble and water-insoluble components. The major compound in the soluble compounds was sodium zinc chloride trihydrate ($\text{Na}_2\text{ZnCl}_4 \cdot 3(\text{H}_2\text{O})$). Some unidentified chlorine compounds were also found as minor soluble components. The insoluble portion consisted of lead chloride (PbCl_2) as the major compound, lead chloride fluoride (PbClF), which is isostructural with the PbCl_2 , and quartz (SiO_2). The X-ray diffraction analysis was done in the Material Analysis Lab, Engineering Research Institute, ISU.

It was suspected that the water used in the tests was the major source of the contaminants. The distilled water was the product of a Barnstead water still (Cat. No. SMO-5S, capacity 5 gal/hr) located in the basement of the Mechanical Engineering Building. Twenty-five liters of a water sample

from the still (single distillation) were concentrated by vaporizing. The result was 35 mg of solid residue. This corresponded to an impurity concentration of 1.4 ppm. Energy dispersive X-ray analysis also performed in the Material Analysis Lab confirmed that the major elements in the residue were silicon (Si), chlorine (Cl), and lead (Pb).

Comparing the surface and water analyses, it is noted that sodium and zinc are not included in the latter. It is recalled that the surface was cleaned with commercial cleanser, Comet (Procter & Gamble, EPA Reg. No. 3573-36AA), as suggested by the manufacturer of the High Flux surface. This was done at the onset of the falling film evaporation tests about one and a half years after the pool boiling tests. At that time, the surface was greenish, dark brown. The cleanser and a brush did restore the appearance to its original bright copper finish. However, the cleanser might very likely have penetrated deep down into the porous structure and not been removed by the routine cleaning method before each test, i.e., brushing with acetone. The surface was cleaned with Comet from time to time afterwards.

According to the label, the active ingredients of Comet are trisodium phosphate (Na_3PO_4 , 14.50 percent), sodium dodecyl benzene sulfonate ($\text{C}_{12}\text{H}_{25}\text{C}_6\text{H}_4\text{SO}_3\text{Na}$, 1.90 percent) and sodium hypochlorite (NaClO , 0.45 percent). Silica (SiO_2), sodium tripolyphosphate ($\text{Na}_5\text{P}_3\text{O}_{10}$), sodium sulfate (Na_2SO_4), sodium sulfamate ($\text{NH}_2\text{SO}_3\text{Na}$), perfume, and color are inert ingredients (83.15 percent). It was concluded that the sodium found in the scale was due to the cleanser.

As for the zinc, it was traced back to the surface contamination when the cartridge heater was soldered in the test section. Caution was

exercised to keep the porous surface from the solder during soldering. However, the surface was contaminated by the cleaning flux which contained zinc chloride.

It is believed that the surface contaminants, especially the residual cleanser, were responsible for the formation of the crystalline deposit. To confirm this, a test was run with distilled water from another water still, in the ISU Chemical Engineering Department. That still was used in the original test generating the PB-HF-D curve shown in Fig. 37, when the surface was new. Fouling was not observed at that time; however scale was found to grow in this test. This meant that when there were nuclei in existence, crystals could grow favorably. In the present case, nuclei were provided by the surface contaminants, especially the residual cleanser. Without them, distilled water alone could not foul the surface as significantly; otherwise fouling should have been observed on the new porous surface.

Fouling continuously degraded the performance of the porous surface, both in pool boiling and falling film evaporation, ever since it was noticed. Data of a long term FFE test with High Flux surface are shown in Fig. 39. It is noticed that at the beginning of the test the data were still quite close to that of the new surface presented in Fig. 37. The superheat increased steadily from the initial value of 2.45 K during the test. The most rapid rise occurred within the first hour after the test started, and then slowed down, but it never reached a steady value and the increasing trend was still evident even after about 32 hours of testing. After changing water, the test was repeated. This time the superheat increased from an initial value of 2.77 K which is 0.32 K higher than that

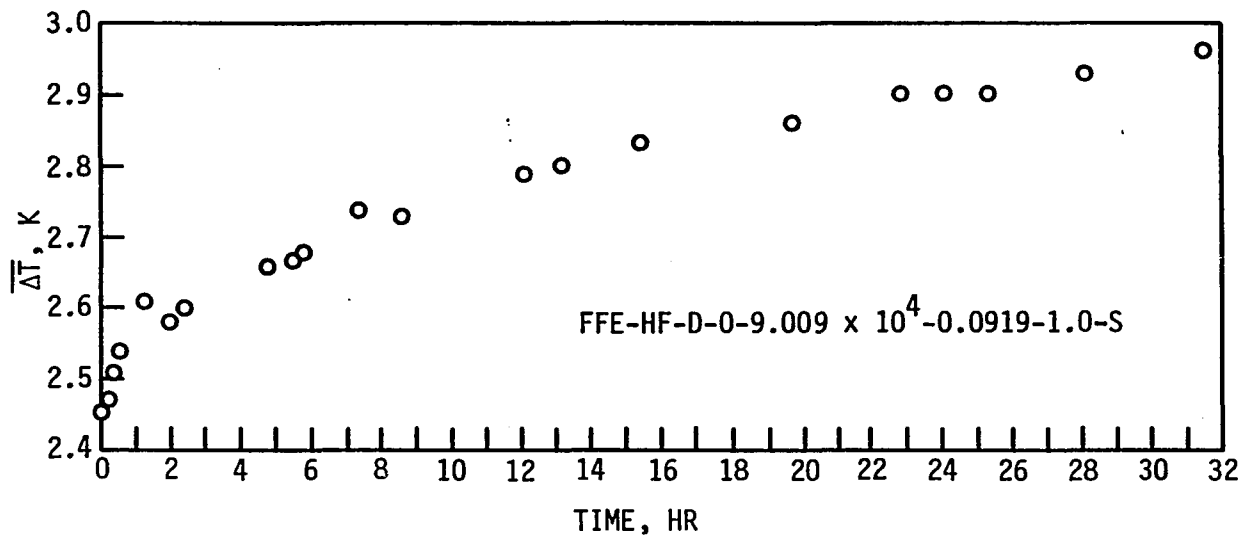


Fig. 39. Degradation of porous surface performance with time due to fouling

in the last test, to 3.30 K in about 10 hours. Also supported by other test results, it was evident that the performance of the porous surface degraded with test time. Better performance could be restored to a certain extent at the beginning of the next test, but degradation was observed right after the test started.

The mechanism of fouling can be sketched at this point. The scale originated from the contaminants, such as the residual Comet cleanser left inside the porous structure. It reacted with the ions in the water and other contaminants already on the surface. The thin film evaporation process on the internal surfaces of the pores accelerated the formation of the crystals. The concentration was high within the liquid film due to the high evaporation rate of water. Crystallization occurred when the concentration was above saturation. Once the nuclei were formed, crystals could grow continuously. Thus, crystals were found inside the pores.

When the fouled tube was tested, fresh distilled water dissolved part of the soluble portion of the scale before boiling started, while the insoluble portion stayed on the surface. At the beginning of the test, heat transfer performance presented a temporary improvement because the pores had been partially cleaned by the water. However, since the nuclei were still there, the soluble crystals immediately started growing in the high-concentration, evaporating internal film by retrieving the ions dissolved in the water. In the meantime, the insoluble crystals also started to grow. The growth of both the soluble and insoluble crystals would have been asymptotic if the system were closed. However, water needed to be replenished from time to time for the long-term tests. The ion concentration of the water was renewed each time after adding fresh

distilled water. Consequently, the growth of scale was fast at the beginning of the test, and slowed down when the ion concentration in the water dropped. Then the growth rate became steady when the concentration level was maintained by replenishment, and the crystals grew continuously. This was reflected by the long-term test data shown in Fig. 39. This is why the fully-established boiling data in Fig. 37 drifted.

The High Flux data presented in this section were all influenced by fouling. Comparing with the new surface data in Fig. 37, it can be seen that data in Figs. 33 and 34 were taken when the surface was slightly fouled, while the data in Figs. 35, 36 and 37 were obtained later with thicker internal surface scale. However, for each test, care was taken not to take data before its change with time due to fouling slowed down to a tolerable rate. Usually, it took about four hours for the rate of change of superheat to drop to 0.2 K/hr. Each test run took about one hour. A second test always followed immediately to double check the repeatability. As shown in Figs. 33 and 34, there was actually little discrepancy between the increasing and decreasing data at low heat fluxes, which, respectively, corresponded to the first and last parts of the data taken in the tests. Therefore, each test curve presented accurately reflects the up-to-date condition of the porous surface. All the analysis, discussion, and conclusions based on the data are, of course, valid.

The problem presented here is uniquely associated with the porous boiling surfaces and water. Although the porous surface often realizes heat transfer performances several or even ten times better than the normal surface, the advantages can be substantially discounted due to fouling. To make things worse, because of the delicate, small-scale, re-entrant

structure, cleaning is virtually impossible. No effective rejuvenating method was developed by the manufacturer of High Flux surface for the OTEC case as of the time the report was prepared [32].

In the present study, an attempt was made to quench the hot surface with cold water in the hope that the scale would peel off from the matrix; however, no change was observed. Extended ultrasonic cleaning has proved to be effective, at least to a certain extent. Heat transfer performance was improved 15 percent after ultrasonic cleaning with distilled water at 65°C for twenty-two hours. It is suggested that combination of ultrasonic and chemical solvent should do the job. However, the selection of the solvent must be determined only after a thorough chemical analysis of the scale substances. Fouling is most effectively controlled by identifying and eliminating the sources of contamination.

6. Summary

In summary, the performance of the High Flux porous surface under the influence of fouling is described in Fig. 40. In addition to the data obtained in the present study, fictitious curves based on the understanding of the behavior of the surface are presented. Start-up behavior as illustrated by the increasing curves in the B-tests is not considered here. There are a common non-boiling falling film evaporation curve and a common flooded non-boiling curve. The non-boiling FFE curve is subject to change at different Γ and H/D according to the data presented before (Figs. 35 and 36). Data always follow one of the common curves, depending on whether the tube is sprayed or flooded, then merge in one of the fully-established boiling curves, depending on how much the surface is fouled: The four fully-established curves presented here correspond with different surface

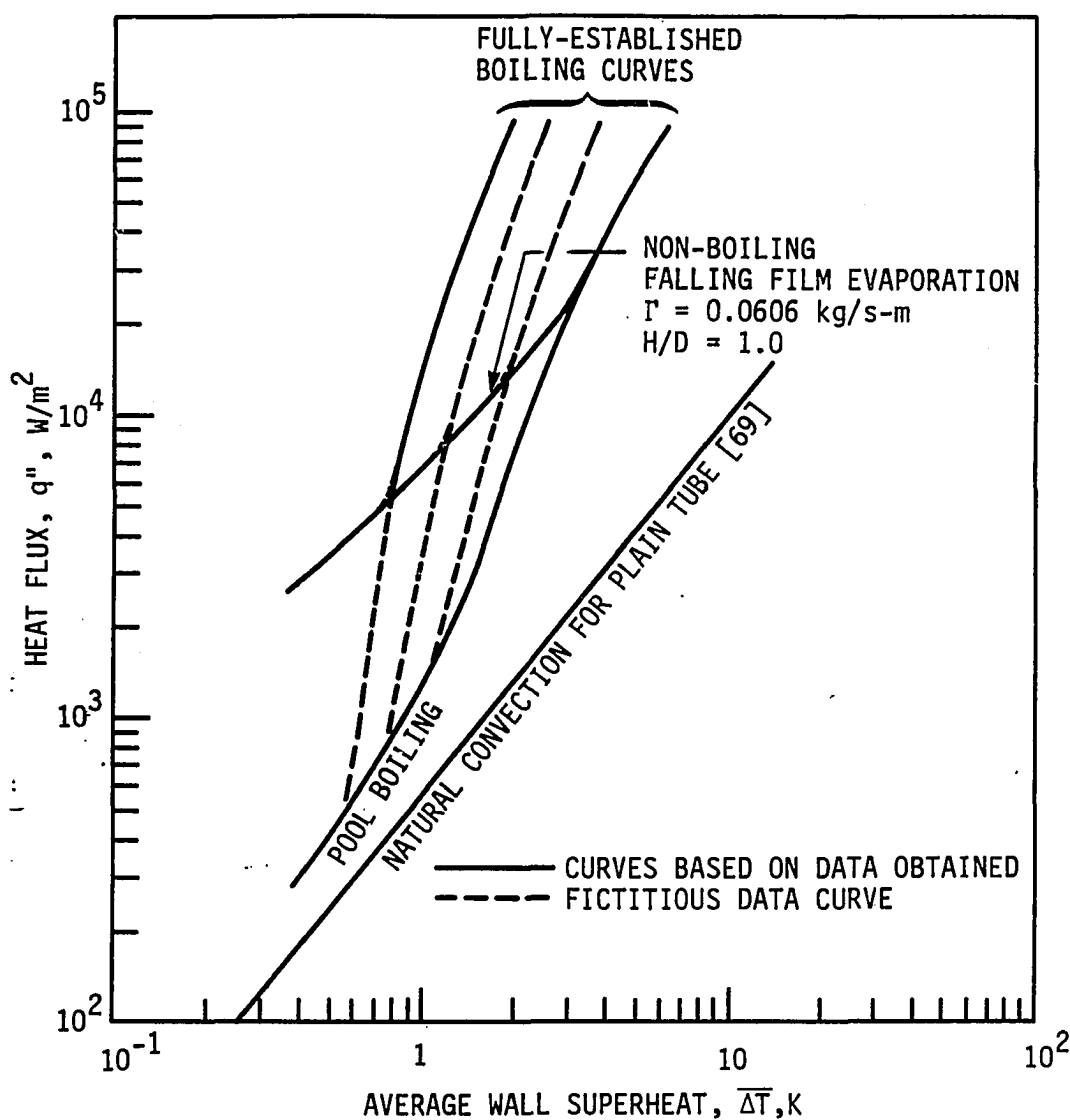


Fig. 40. Summary plot for the performance of High Flux porous surface

conditions during the process of fouling. The one to the left was obtained when the surface was clean (Fig. 37). The boiling curve could move even further right to get close to the plain surface curve when the surface is very much fouled.

E. Summary of Results and General Discussion

1. Liquid supply mode

The heat transfer performances in sprayed and flooded modes are compared in Figs. 19, 24, 29 and 37. The advantage of the sprayed mode at low temperature difference is significant. However, this reduces as the heat flux (or superheat) increases. For those boiling-enhancing surfaces such as Thermoexcel-E and High Flux, boiling starts to be the dominant mode of heat transfer at lower superheat, and the falling film evaporation data merge into the fully-established nucleate boiling curve. The merging takes place at lower heat fluxes with High Flux than with Thermoexcel. Nucleate boiling has never been dominant throughout the test range on the plain surface in the sprayed mode. However, established nucleate boiling could be obtained with a heater of higher power density or by using direct electric heating of a thin walled tube. The present data suggest that the fully-established boiling curve of falling film evaporation should lie to the right of the PB curve for the smooth surface. There appears to be a tendency of merger of FFE and PB data at high heat flux for the GEWA-T surface. However, this is again subject to verification by experiment using a high power heater.

2. Heat transfer surface

Among the heat transfer surfaces tested, High Flux and Thermoexcel-E

are characterized by incipient boiling at low superheats and high boiling coefficients realized by internal thin film evaporation. The boiling curves feature departures from convection or the "knees" at low superheats and steep fully-established boiling curves (Figs. 25-29, 33, 34 and 37). The Thermoexcel-E curves feature a unique first-stage nucleate boiling before the fully-established boiling. Before incipient boiling, these surfaces behave pretty much the same as the plain surface (Figs. 14, 16, 18 and 19). The advantages are significant only after the enhanced boiling becomes the dominant mode of heat transfer. Thermoexcel-E and High Flux are therefore classified as boiling-enhancing surfaces.

One of the main differences between HF and Thermoexcel-E surfaces is in the way in which the FFE and the PB curves merge. A High Flux FFE curve presents a drastic change in slope and enters the fully-established PB curve in a narrow range of transition at low heat flux (Fig. 37). This is because of the simultaneous activation of populous nucleation sites of the same size at a certain power level. On the other hand, the FFE data of the Thermoexcel-E approach the fully-established PB curves in a more gradual fashion (Fig. 29), and the merging takes place at higher heat fluxes. Apparently the mechanism associated with the two-phase flow in the minute tunnels in the surface makes the boiling develop gradually during the process of increasing power.

The Thermoexcel-E surface is characterized by unstable nucleate boiling at low superheat before the normal boiling process takes place. It is speculated that the first-stage nucleate boiling is provided by the internal nucleation sites in the surface structure; this terminates when cooler ambient liquid is sucked into the tunnels.

The High Flux porous surface was found vulnerable to fouling.

Crystals deposit inside and clog the pores due to internal evaporation of the liquid film. The enhancement in heat transfer can be substantially reduced.

The GEWA-T surface presents FFE boiling curves without significant slope changes or "knees" within the present test range. Although bubbles were observed at higher heat fluxes, boiling was never a dominant mode of heat transfer in the heat flux range tested. However, this may change if the surface is tested at even higher heat flux. The advantage appears to be mainly in the low superheat region, where convective heat transfer is enhanced by the extended surface as well as surface-tension effects at low film flow rate.

The heat transfer performances of all the surfaces tested are compared in Fig. 41. Among numerous test curves presented in this chapter, only the normal curves with the best performance for different surfaces under different liquid feed modes are shown. The start-up curves for Thermoexcel-E and High Flux surfaces are not shown in this figure. All the FFE curves for different surfaces are obtained under the condition that $\Gamma = 0.0606 \text{ kg/s-m}$ and $H/D = 1.0$. The FFE-1 curve shown in Fig. 41 is actually the FFE-a-B-0-V-0.0606-1.0-S curve presented in Fig. 19. The PB-1 curve is the PB-1-D-0.3-C curve obtained when the surface was new [56]. The FFE-GEWA-T19C curve is based on the FFE-GEWA-T19C-D-75-V-0.0606-1.0-S test data. The PB-GEWA-T19C curve is from the PB-GEWA-T19C-D-77-S data in Fig. 24. The TE curves presented are FFE-TE-D-0.2-V-0.606-1.0-C and PB-TE-D-51.4-C, because tests with D treatment and continuous increasing heat flux yielded the highest coefficients. The FFE-HF and PB-HF curves

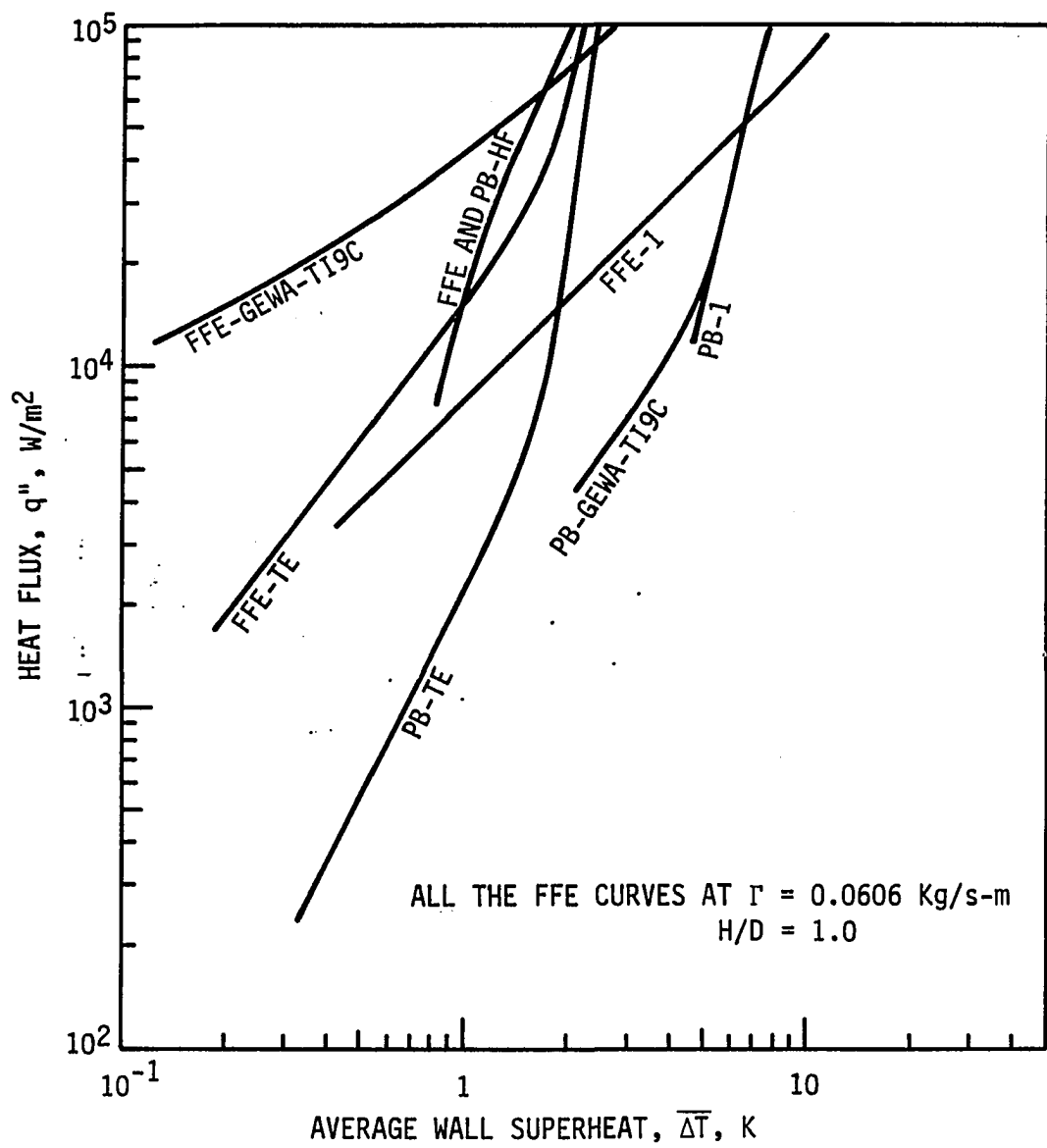


Fig. 41. Comparison of heat transfer performance of different surfaces

are from Fig. 40. The normal curves of falling film evaporation and pool boiling merge into a single curve. The normal boiling curve presented for the High Flux surface is a PB-HF-D curve obtained when the surface was new [56].

All the structured surfaces show significant enhancement in heat transfer over the plain surface. The extent of enhancement depends upon the level of heat flux or wall superheat. For a heating surface where heat flux is the control variable, such as one with an electric or radiative heating source, the GEWA-T surface shows the smallest temperature differential at low heat fluxes due primarily to extended-surface and surface-tension effects, while Thermoexcel-E and High Flux yield lower temperature differential at heat flux close to 10^5 W/m^2 , due to enhanced generation of vapor phase. For a surface of which the temperature is the control variable, such as condensing vapor, GEWA-T results in greater heat flux at low superheat, while Thermoexcel-E and High Flux yield greater heat flux at higher superheat.

3. Surface aging

As expected, surface aging was only a factor with the boiling-enhancing surfaces. The drying procedure removes any liquid trapped in the surface structure, and saturates every cavity with air. These cavities then serve as nuclei for nucleate boiling. In contrast, most of the air content in the cavities is depleted during preboiling. It was concluded that the D-treatment provided higher normal heat transfer coefficient than B in both the falling film evaporation and pool boiling tests for the Thermoexcel-E surface (Figs. 25-29).

The surface aging did not affect the normal boiling coefficient of the

High Flux porous surface; however, significant hysteresis was observed in the B-tests (Fig. 33), due to difference between the numbers of nucleation sites available during increasing and decreasing power traverses. The number of nucleation sites available was minimal after surface preboiling and subcooling, thus resulting in a lower heat transfer coefficient than the normal value. Therefore, drying the surface in the air can reduce the hysteresis for High Flux and enhance the normal falling film evaporation and pool boiling coefficient of Thermoexcel-E.

4. Surface subcooling

The surface subcooling treatment was implemented with the intention of snuffing out the potential nucleation sites. This treatment, in combination with the preboiling treatment, is particularly effective with the boiling-enhancing surfaces [55]. The vapor saturated in the cavities after preboiling is readily condensed by the subcooling treatment. It is clear that the combination of B-treatment and substantial surface subcooling did result in lower normal heat transfer coefficients for the Thermoexcel-E surface (Figs. 25, 27, and 29) and hysteresis for the High Flux surface (Fig.33). However, it seems that the degree of surface subcooling does not play a decisive role. Greater surface subcooling results in higher coefficients in flooded tests for the Thermoexcel-E surface; however this is not necessarily true for falling film evaporation tests.

5. Heat flux

Since the test sections were heated by electric power controlled by a powerstat, the heat flux is considered as an independent variable in the present tests. Heat transfer coefficient is independent of heat flux in

the convective or non-boiling region, and the q'' vs. ΔT curve has unity slope. This was shown in almost the entire test range in the plain tube and GEWA-T tube test curves (Figs. 14, 16, 18 and 20). Heat flux plays a more important role on the boiling-enhancing surfaces when boiling takes place. Very high coefficients (maximum observed of 3.7×10^4 W/m²-K) can be obtained on the Thermoexcel-E surface if the heat flux does not exceed the limit of the first-stage nucleate boiling (Fig. 32). On the other hand, it takes a high heat flux (or great superheat) to activate the nucleation sites on a preboiled High Flux surface and establish the boiling in the normal mode (Fig. 33). The boiling-enhancing surfaces are characterized by much higher heat transfer coefficients at high heat fluxes, because of the steep fully-established boiling curves. For all surfaces in the high heat flux region, when boiling is dominant, heat transfer is not affected by the change of film flow rate and liquid feed falling distance (Figs. 15, 17, 23, 30, 31, 35, and 36), except that heat transfer coefficient of the GEWA-T surface decreases at low flow rate due to internal surface dryout.

6. Film flow rate

Film flow rate is influential only in the convective regions. The non-boiling data of plain tube were in fair agreement with the present analysis and predictions reported (Fig. 14). It is noted, however, that a range of predicted curves is found in the literature. No predictions or data were available for comparison with the present non-boiling falling film evaporation data for the structured surfaces. Heat transfer with the Thermoexcel-E and High Flux surfaces is independent of the flow rate at

high heat fluxes (Figs. 30 and 35), because boiling dominates the heat transfer.

7. Liquid feed height

Like film flow rate, the feed height is influential only in the convective regions. For the plain tube at low heat flux, the relationship between the heat transfer coefficient and the non-dimensional feed height shown by the present data is exactly what was predicted by Owens' correlation [7] (Fig. 17). This relationship is overridden at high heat fluxes when nucleate boiling dominates; and heat transfer coefficient is constant with respect to the change of feed height. The influence is weaker for the GEWA-T surfaces even though heat transfer is not boiling-dominant in nature (Fig. 23). This is likely because the channel flow is sheltered by the restricted geometry from the influence of the impacting feed liquid. The heat transfer of Thermoexcel-E and High Flux is independent of H/D, except at low heat fluxes when convection is still dominant (Figs. 31 and 36).

8. Rate of heat flux change

The rate of heat flux change has been shown to affect the boiling heat transfer on High Flux surface by motivating the metastable bubbles whose growth is limited by the cooler liquid surrounding the heating surface [55]. The result is the inception of boiling occurs at lower superheat if heat flux is changed stepwise. The trend is not that clear in falling film evaporation on the High Flux surface (Fig. 33). However, the influence is more significant on the Thermoexcel-E surface (Fig. 25). A surge of ambient cold liquid can be induced by step-change of heat flux, which rushes into the tunnels and snuffs out active or potential nucleation

sites. If the heat flux is changed slowly and continuously, more nucleation sites are preserved and a higher normal heat transfer coefficient is obtained. Therefore, a slow, continuous increase of heat flux yields high normal falling film evaporation and pool boiling coefficients on Thermoexcel-E surface, while step increase of heat flux results in better pool boiling performance with the High Flux surface. The influence of rate of heat flux change on the plain and GEWA-T tubes is not evident.

VI. CONCLUSIONS AND RECOMMENDATIONS

A model for saturated falling film evaporation on a horizontal plain tube was developed. The model defines heat transfer in three distinct regions: the jet impingement region, the thermal developing region, and the fully developed region. It is assumed that the situation at the apex of the tube is a two-dimensional liquid jet impinging on a flat heating plate. In the thermal developing region, the film is superheated from saturation to a fully developed linear temperature profile. The developing length was estimated by considering the distance required for the fully-developed linear temperature profile to develop. In the developed region, the entire heat transfer produces evaporation at the liquid/vapor interface. The developed heat transfer coefficient was calculated by solving the Nusselt's problem for film evaporation. Compared with experimental data, the present model yielded good predictions.

The enhancement of falling film evaporation on commercial structured heat transfer surfaces was studied. Experiments using electrically heated test sections with smooth, GEWA-T, Thermoexcel-E, and High Flux surfaces were conducted to investigate the effects of liquid supply mode, surface structure, surface aging, surface subcooling, heat flux, film flow rate, liquid feed height, and rate of heat flux change. Complementary pool boiling experiments were also conducted. An experimental facility and an accurate test procedure were developed for study of evaporation and boiling from structured heat transfer surfaces.

Heat transfer within the test cylinders was analyzed. The local surface heat flux of the test cylinder under the influence of inactive

zones in the commercial heater soldered in the cylinder was determined. The averaging method was legitimized by conducting analyses for the effects of non-uniform inside heat flux distribution and outside heat transfer coefficient variation.

The major conclusions that can be drawn from the present investigation are as follows:

1. The falling film evaporation provides heat transfer coefficients higher than the natural convection which characterizes pool boiling at low superheats. The advantage becomes less significant at higher heat fluxes (or superheats). The falling film evaporation data for the structured surfaces merge with the respective pool boiling curves; however, this merging is not observed with a plain surface.

2. High Flux and Thermoexcel-E surfaces are characterized by incipient boiling at low superheats and high boiling coefficients, realized by internal thin film evaporation. They are effective boiling-enhancing surfaces.

3. The first-stage nucleate boiling on the Thermoexcel-E surface before normal boiling was described for the first time. The vapor appears to be generated by the internal nucleation sites of the surface structure.

4. GEWA-T surfaces enhance convective heat transfer through extended surface and surface tension effect at low heat flux. Boiling does not play an important role on this surface except at very high heat flux.

5. In both falling film evaporation and pool boiling on Thermoexcel-E, a pre-dried surface presents higher normal heat transfer coefficients than a preboiled surface. Also, slowly increasing the heat flux results in normal coefficients higher than those obtained with

step changes in power.

6. Film flow rate and liquid feed height have small effects on non-boiling convection. The heat transfer is not affected by these variables when boiling is dominant.

7. Fouling is a serious problem with the High Flux porous surface when boiling water. When certain contaminants are present, crystals can grow on the internal surface of the matrix and clog the pores. The small-scale, re-entrant surface structure makes cleaning virtually impossible.

The falling film evaporation always yields no lower heat transfer coefficients than pool boiling for GEWA-T, Thermoexcel-E and High Flux surfaces. The FFE and PB curves merge at medium heat flux level for High Flux surface. As for the GEWA-T and Thermoexcel-E, the tendency of merging at high heat flux is evident. The present data for smooth surface suggest that the fully-established FFE boiling curve lies to the right of the fully developed PB curve. However, this is subject to verification by performing tests at heat flux beyond the present test range.

In the present study, the performances of the structured surfaces in falling film evaporation have been investigated in detail for the first time. Besides the effects investigated in the present study, fluid properties may be the next to be considered. Fluids of different wetting abilities are particularly interesting in that the boiling performances of individual surfaces may be influenced. The enhancement of pool boiling performance with GEWA-T surface might be significant in different boiling liquids. The data obtained in this study can be directly used for design of water spray film evaporation.

The present tests disclosed the vulnerability of the porous heat transfer surface to fouling. It is very important to keep the surface from contamination and to operate in a well controlled condition. This problem must be also closely watched with other structured surfaces.

Two distinct characteristics of structured heat transfer surfaces were proposed in this study. A structured surface can be either convection-enhancing such as GEWA-T, or boiling-enhancing such as Thermoexcel-E and High Flux. A convection-enhancing surface is usually advantageous when operating at low superheat; whereas a boiling-enhancing surface has better performance at high superheat. It is suggested that a convection-and-boiling-enhancing surface might be developed which has good performance throughout the range of operating superheat. A surface incorporated with both large and small scale structures, such as fins coated with a porous layer, may yield outstanding performance.

In the present study, a single tube spray film evaporator was tested. Care has been taken to set the environment and the feed hydrodynamics as close to the real situation in a multiple-tube spray film evaporator as possible. Both analytical and experimental results presented are valid for all the tubes at different locations in a tube bundle. However, in order to predict heat transfer performances of individual tubes, distribution of feed flow rate in the bundle needs to be determined. The feed flow rate decreases as the liquid travels from the top toward the bottom level of the tubes. The decrease in the flow rate of the liquid is due to the vaporization as it flows along the tube surface and flash between two levels of tubes. The feed flow rate distribution in a tube bundle may be also influenced by the vapor cross flow and misalignment of tubes. The

overall performance of a multiple-tube spray film evaporator can be evaluated after the performance of each tube is predicted based on the local feed flow rate.

VII. REFERENCES

1. Yundt, B. and Rhinesmith, R. "Horizontal Spray-Film Evaporation." Chemical Engineering Progress #77 (September 1981); 69-74.
2. Czikk, A. M., Fricke, H. D., Ganic, E. N., and Sharma, B. I. "Fluid Dynamic and Heat Transfer Studies of OTEC Heat Exchangers." Proceedings of the Fifth Ocean Thermal Energy Conversion Conference. Miami Beach, Florida 1978: VI-181-236.
3. Seban, R. A. "Transport to Falling Films." Proceedings of 6th International Heat Transfer Conference. Toronto, Canada, 417-428, 1978.
4. Chun, K. R., and Seban, R. A. "Heat Transfer to Evaporating Liquid Films." J. Heat Transfer 93 (1971): 391-396.
5. Liu, P. J. P. "The Evaporating Falling Film on Horizontal Tubes." Ph.D. Thesis, University of Wisconsin, Madison, Wisconsin, August, 1975.
6. Lorenz, J. J., and Yung, D. "A Note on Combined Boiling and Evaporation of Liquid Films on Horizontal Tubes." J. Heat Transfer 101 (1979): 178-180.
7. Owens, W. L. "Correlation of Thin Film Evaporation Heat Transfer Coefficients for Horizontal Tubes." ASME Paper 78-WA/HI-67, 1978.
8. Cannizzaro, C. J., Karpf, J. Z., Kosowski, N. and Pascale, A. S. "Fourth Report on Horizontal Tube Multiple-Effect (HTME) Process Pilot Plant Test Program." Office of Saline Water Research and Development Progress Report No. 74-967, May 1974.
9. Standiford, F. C. "Heat Transfer Performance and Design Problems of Horizontal Tube Evaporators." Office of Saline Water Report No. 521, November 1972.
10. Fletcher, L. S., Sernas, V., and Galowin, L. S. "Evaporation from Thin Water Films on Horizontal Tubes." ASME Paper 73-HT-42, 1973.
11. Fletcher, L. S., Sernas, V., and Parken, W. H. "Evaporation Heat Transfer Coefficients for Thin Sea Water Films on Horizontal Tubes." Ind. Eng. Chem. Proc. Des. Dev. 14 1975: 411-416.
12. Parken, W. H., Jr. "Heat Transfer to Thin Water Films on Horizontal Tubes." Ph.D. Thesis, Rutgers University, 1975.

13. Sernas, V. "Heat Transfer Correlation for Subcooled Water Films on Horizontal Tubes." Journal of Heat Transfer, 101 (1979): 176-178,
14. Rohsenow, W. M. "A Method of Correlating Heat Transfer Data for Surface Boiling of Liquids." Transaction of ASME 74 (1952): 969-976.
15. Nusselt, W. "Die Oberflaechenkondensation des Wasserdampfes." Zeitschrift des Vereines Deutscher Ingenieure, 60, 27, (1916): 541-546 and 569-575.
16. Sabin, C. M. and Poppendiek, H. F. "Film Evaporation of Ammonia Over Horizontal Round Tubes." Proc. of the Fifth Ocean Thermal Energy Conversion Conf., Miami Beach, FL. 1978: VI 237-260.
17. Nakazatomi, M. and Bergles, A. E. "Film Evaporation Model on Horizontal Tubes." Research Report of Ube Technical College, No. 27 (1981): 63-70.
18. Conti, R. J. "Experimental Investigations of Horizontal Tube Ammonia Film Evaporators with Small Temperature Differentials." Proc. of the Fifth Ocean Thermal Energy Conversion Conf. Miami Beach, FL. 1978: VI 161-180.
19. Schultz, V. N., Edwards, D. K.; and Catton, I. "Experimental Determination of Evaporative Heat Transfer Coefficients on Horizontal, Threaded Tubes." AICHE Symposium Series 73, 164, (1977): 223-227.
20. Moalem-Maron, D., Semiat, R. and Sideman, S. Technician R & D Foundation Project 071-082, Report No. 53 to Israel Nat. Council for R&D, April 1978.
21. Cox, R. B. "Some Factors Affecting Heat Transfer Coefficients in the Horizontal Tube Multiple Effect (HTME) Desalination Process." 3rd Int. Symp. on Fresh Water from the Sea, Vol 1, (1970): 247-263.
22. Newson, I. H. "Heat Transfer Characteristics of Horizontal Tube Multiple Effect Evaporators." Final Report INCRA Project No. 267, Chemical Engineering Div., Atomic Energy Research Establishment, Harwell, England, February 1976.
23. Prince, W. J. "Enhanced Tubes for Horizontal Evaporator Desalination Processes." M. S. Thesis, University of California at Los Angeles, School of Engineering, 1971.
24. Edwards, D. K., Gier, K. D., Ayyaswamy, P. S., and Catton, Ivan. "Evaporation and Condensation in Circumferential Grooves on Horizontal Tubes." The American Society of Mechanical Engineers, Paper 73-HT-25, 1973.

25. Newson, I. H. "Heat Transfer Characteristics of Horizontal Tube Multiple Effect (HTME) Evaporators--Possible Enhanced Tube Profiles." Proc. 6th International Symposium Fresh Water from the Sea, Vol. 2, (1978): 113-124.
26. Sideman, S. and Levin, A. "Effect of the Configuration on Heat Transfer to Gravity Driven Films Evaporating on Grooved Tubes." Desalination 31 (1979): 7-18.
27. Sideman, S., Moalem, D., and Semiat, R. "Theoretical Analysis of Horizontal Condenser-Evaporator Conduits of Various Cross-Sections." Desalination 17 (1975): 167-192.
28. Sideman, S., Moalem, D., and Semiat, R. "Performance Improvement of Horizontal Evaporator-Condenser Desalination Units." Desalination 21 (1977): 221-233.
29. Sideman, S., and Moalem-Maron, D. "Transport Characteristics of Thin Films: Evaporation, Condensation, and Mass Transfer on Smooth and Grooved Horizontal Conduits, Two-Phase Momentum." Heat and Mass Transfer in Chemical Process and Energy Engineering Systems, Vol. 2, pp. 877-896, Washington, D.C. Hemisphere Publishing Corporation, 1979.
30. Semiat, R., Sideman, S., Moalem Maron, D. "Turbulent Film Evaporation on and Condensation in Horizontal Elliptical Conduits." Heat Transfer 1978, Proc. 6th Int. Heat Transfer Conf., Toronto, Canada, 361-366, 1978.
31. Hillis, D. L, Lorenz, J. L., Yung, D. T. and Sather, N. F. "OTEC Performance Tests of the Union Carbide Sprayed-Bundle Evaporator." Department of Energy Report ANL-OTEC-PS-3, May 1979.
32. Lorenz, J. J., Yung, D., Howard, P. A., Panchal, C. B., and Poucher, F. W. "OTEC-1 Power System Test Program: Performance of One-Megawatt Heat Exchangers." Department of Energy Report ANL/OTEC-PS-10, November 1981.
33. Webb, R. L. "The Evolution of Enhanced Surface Geometries for Nucleate Boiling." Heat Transfer Eng. 2, 3-4 (1981): 46-69.
34. Chyu, M.-C., Bergles, A. E. and Mayinger, F. "Enhancement of Horizontal Tube Spray Film Evaporators." Heat Transfer 1982, Proceedings of the 7th International Heat Transfer Conference, Munich, F.R. Germany, Vol. 6, 1982: 275-280.
35. Saier, M., Kaestner, H.-W., and Kloeckler, R. "Y- and T-Finned Tubes and Methods and Apparatus for Their Making" U. S. Patent 4,179,911, December 25, 1979.

36. Yilmaz, S. and Westwater, J. W. "Effects of Commercial Enhanced Surfaces on the Boiling Heat Transfer Curve." Advances in Enhanced Heat Transfer, HTD Vol. 18, pp. 73-91, New York: ASME, 1981.
37. Yilmaz, S., Hwalek, J. J. and Westwater, J. W. "Pool Boiling Heat Transfer Performance for Commercial Enhanced Tube Surfaces." ASME Paper No. 80-HT-41, 1980.
38. Marto, P. J. and Lepere, J. "Pool Boiling Heat Transfer from Enhanced Surfaces to Dielectric Fluids." Journal of Heat Transfer 104 (1982): 292-299.
39. Stephan, K. and Mitrovic, J. "Heat Transfer in Natural Convective Boiling of Refrigerants and Refrigerant-Oil-Mixtures in Bundles of T-Shaped Finned Tubes." Advances in Enhanced Heat Transfer, pp. 131-146, New York: ASME, 1981.
40. Stephan, K., Mitrovic, J. "Heat Transfer in Natural Convective Boiling of Refrigerant-Oil Mixtures." Heat Transfer 1982, Proceedings of the 7th International Heat Transfer Conference, Munich, F.R. Germany, Paper PB12, 1982.
41. Fujie, K., Nakayama, W., Kuwahara, H., and Kakizaki, K. "Heat Transfer Wall for Boiling Liquids." U. S. Patent 4,060,125, November 29, 1977.
42. Fujie, K., Nakayama, W., Kuwahara, H., Nakayama, Y., and Kakizaki, K. "High-Flux Heat Transfer Tubes 'Thermoexcel's': Their Performance and the Results of Feasibility Test in a Refrigerating Machine." XIV International Congress of Refrigeration, Moscow, Paper B1, 97, 1975.
43. Arai, A., Arai, N., Fushima, T., Nakayama, W., Fujie, K. "Heat Transfer Characteristics of 'Thermoexcel' Tubes in Heat Exchangers of Turbo-Refrigerating Machines." IIF-IIR Commissions B1, B2, and B3, pp. 15-20, Belgrade, Yugoslavia, 1977.
44. Nakayama, W., Daikoku, T., Kuwahara, H., and Nakajima, T. "Dynamic Model of Enhanced Boiling Heat Transfer on Porous Surfaces." Journal of Heat Transfer 102 (1980): 445-456.
45. Torii, T., Hirawawa, Kuwahara, S., Yanagida, H., and Fujie, K. "The use of heat Exchangers With Thermoexcel's Tubing in Ocean Thermal Energy Power Plants." ASME Paper No. 78-WA/HT-65, 1978.
46. Ogata, H. and Nakayama, W. "Heat Transfer to Boiling Helium from Machined and Chemically Treated Copper Surfaces." Proceeding of the 1981 Cryogenic Engineering Conference, San Diego, CA., Vol. 27, 1982: 309-317.

47. Nakayama, W., Daikoku, T., and Nakajima, T. "Modeling of Liquid Suction Mechanism in Porous Surface Boiling." ASME, Paper No. 80-HT-122, 1980.
48. Nakayama, W., Daikoku, T., Nakajima, T. "Effects of Pore Diameters and System Pressure on Saturated Pool Nucleate Boiling Heat Transfer from Porous Surfaces." Journal of Heat Transfer 104 (1982): 286-291.
49. Nakayama, W., Daikoku, T., and Nakajima, T. "Enhancement of Boiling and Evaporation on Structured Surfaces with Gravity Driven Film of R-11." Heat Transfer 1982, Proceedings of the 7th Int. Heat Transfer Conf., Munich, F. R. Germany, Vol. 4, 1982: 409-414.
50. Grant, A. G. "Porous Metallic Layer and Formation." U. S. Patent 4,064,914, 1977.
51. Bergles, A. E. and Chyu, M.-C. "Characteristics of Nucleate Pool Boiling from Porous Metallic Coatings." Journal of Heat Transfer 104 (1982): 279-285.
52. Czikk, A. M., Gottzmann, C. F., Ragi, E. G., Withers, J. G. and Habdas, E. P. "Performance of Advanced Heat Transfer Tubes in Refrigerant - Flooded Liquid Coolers." ASHRAE Transactions 1, Part I, 1970: 96-109.
53. Gottzmann, C. F., O'Neill, P. S. and Minton, P. E. "High Efficiency Heat Exchangers." Chemical Engineering Progress 69, 7 (July 1973): 59-75.
54. Czikk, A. M. and O'Neill, P. S. "Correlation of Nucleate Boiling from Porous Metal Films." Advances in Enhanced Heat Transfer, pp. 53-60. New York: ASME, 1979.
55. Czikk, A. M., O'Neill, P. S. and Gottzmann, C. F. "Nucleate Boiling from Porous Metal Films: Effect of Primary Variables." Advances in Enhanced Heat Transfer, HTD Vol. 18, pp. 109-122, New York: ASME, 1981.
56. Chyu, M.-C. "Boiling Heat Transfer from a Structured Surface." M.S. Thesis. Iowa State University: Ames, Iowa, 1979.
57. McMurray, D. C., Myers, P. S., and Uyehara, O. A. "Influence of Impinging Jet Variables on Local Heat Transfer Coefficients Along a Flat Surface With Constant Heat Flux." Proceedings of the 3rd International Heat Transfer Conference, Vol. II, (1966): 292-299.

58. Miyasaka, Y. and Inada, S. "The Effect of Pure Forced Convection on the Boiling Heat Transfer Between a Two-dimensional Subcooled Water Jet and a Heated Surface." Journal of Chemical Engineering of Japan, 13, 1 (1980): 22-28.
59. Myers, G. E. Analytical Methods in Conduction Heat Transfer. New York: McGraw-Hill Book Company, 1971.
60. Thomson, A. K. G. "Heat Transmission in Film-Type Coolers." Journal of the Society of Chemical Industry, 56, (1937): 380T-384T.
61. Adams, F. W., Broughton, G., and Conn, A. L. "A Horizontal Film Type Cooler." Industrial and Engineering Chemistry, Vol. 28, No. 5, p. 537, 1936.
62. Junkhan, G. H. and Bergles, A. E. "Heat Transfer Laboratory Data Acquisition System." Engineering Research Institute, Iowa State University, December 1976.
63. Meyer, C. A., McClintock, R. B., Silvestri, G. J., and Spencer, R. C., Jr. ASME Steam Tables, New York: The American Society of Mechanical Engineers, 1967.
64. Sparrow, E. M. and Lee, L. "Analysis of Flow Field and Impingement Heat/Mass Transfer due to a Nonuniform Slot jet." Journal of Heat Transfer 97 (1975): 191-197.
65. Gardon, R. and Akfirat, J.C. "The Role of Turbulence in Determining the Heat Transfer Characteristics of Impinging Jets." International Journal of Heat and Mass Transfer 8 (1965): 1261-1272.
66. Miyazaki, H. and Silberman, E. "Flow and Heat Transfer on a Flat Plate Normal to a Two-Dimensional Laminar Jet Issuing From a Nozzle of Finite Height." International Journal of Heat and Mass Transfer 15 (1972): 2097-2107.
67. Dukler, A. E. "Fluid Mechanics and Heat Transfer in Vertical Falling Film Systems." Chem. Eng. Prog. Symp. Ser., 56, 30 (1960): 1-10.
68. Stauzione, K. A. "An Optical Approach to Investigate Nucleate Boiling in Thin Water Films." AIAA International Meeting & Technical Display "Global Technology 2000", May 6-8, 1980, Baltimore, MD, AIAA-80-0897.
69. McAdams, W. H. Heat Transmission, 3rd Ed., New York: McGraw-Hill Book Company, Inc., 1954.

70. Ayub, Z. H. Heat Transfer Laboratory, Iowa State University, Ames, Iowa, Private communication, 1984.
71. Perry, R. H., and Chilton, C. H. Chemical Engineers' Handbook, New York: McGraw-Hill Book Company, 1973.
72. Steel, G. D. and Torrie, J. H. Principles and Procedures of Statistics, New York: McGraw-Hill Book Company, 1980.

VIII. ACKNOWLEDGMENTS

The author would like to express his sincerest gratitude to Dr. A. E. Bergles, for his encouragement and help throughout the study. The opportunities for free thinking, liberal discussion, and complete execution are gratefully appreciated and have been very much enjoyed. Acknowledgment is also due to other members in the graduate study committee, Dr. G. H. Junkhan, Dr. R. H. Pletcher, and Dr. B. R. Munson, for their teaching and advice. The energy aspect of the study program was enhanced by Dr. W. J. Cook.

This study was supported in part by the U. S. Department of Energy under Contract DE-AC22-78ET13127 and Grant DE-FG07-81ID12222. Experimental facilities and support services were provided by the Department of Mechanical Engineering and the Engineering Research Institute. Test sections and technical assistance provided by Mr. C. F. Gottzmann and Mr. P. S. O'Neill of the Linde Division of Union Carbide Corporation, Mr. K. Menze of Wieland-Werke AG, and Dr. W. Nakayama of Hitachi, Ltd. are gratefully acknowledged. Invaluable suggestion on heat transfer analysis within the test cylinder was made by Dr. S. P. Sukhatme of Indian Institute of Technology-Bombay, then Visiting Professor at Iowa State University.

Initial experiments were carried out at the Institut fuer Verfahrenstechnik, Universitaet Hannover, FGR. The author wishes to acknowledge a research assistantship granted by Professor F. Mayinger, Institut Direktor.

The author is grateful to his parents for their understanding and encouragement. Gratitude is also expressed to Professor Mingking Chyu, now

at Arizona State University, for being a good brother and helpful fellow heat transfer researcher. Thanks are also due to Mrs. Donna Birdsong and Mrs. Lorraine O'Brien for their typing.

IX. APPENDIX 1: DESIGN OF A PERFORATED-PIPE FLOW DISTRIBUTOR

As described in the section for experimental apparatus (IV.A.1), the flow distributor employed in the present study had a perforated pipe distributing incoming liquid in the shell. The temperature distribution of the efflux along the slot on the shell would not have been uniform unless the inlet liquid with substantial subcooling was evenly distributed in the shell. (See Fig. 13.) The purpose of the present section is to describe the design of a perforated pipe with guaranteed distributing capability based upon the usual fluid mechanics considerations.

The configuration of interest is a perforated pipe closed on one end, with fluid feeding in on the other. The flow distribution from each hole is uniform when there is a proper balance among (a) kinetic energy of the inlet flow, (b) energy loss due to friction along the length of the pipe and (c) energy loss across the outlet holes [71]. When the inlet-stream kinetic energy predominates, a greater amount of fluid will be discharged from the holes near the closed end; when friction losses along the pipe predominate, a smaller amount of fluid will be discharged near the closed end. When an upstream disturbance, such as that produced by a bend, is superimposed upon a high velocity inlet stream, the flowrate from the outlet holes near the pipe inlet and near the closed end can be greater than in the middle. A rule of thumb for design is that the ratios of kinetic energy of the inlet flow to the pressure drop across the outlet hole, and of friction loss in the pipe to the pressure drop across the outlet hole should be no greater than one-tenth, i.e.,

$$\frac{KE_i}{\Delta h_o} < 0.1$$

and

$$\frac{\Delta h_p}{\Delta h_o} < 0.1 \quad (A1)$$

The kinetic energy of the inlet stream is

$$KE_i = \frac{\alpha u_i^2}{2g} \quad (A2)$$

where α is the correction factor to compensate for using average velocity u_i , with value depending on the velocity profile.

The loss in head due to friction and momentum recovery over the length of the pipe can be shown to be

$$\Delta h_p = \left(\frac{4fL}{3D} - 2 \right) \frac{u_i^2}{2g} \quad (A3)$$

where f is the Fanning friction factor. The loss in head across the outlet holes can be estimated by

$$\Delta h_o = \left(\frac{Q}{CA_o} \right)^2 \frac{[1 - (A_o/A_i)^2]}{2g} \quad (A4)$$

where C is the orifice coefficient.

The final dimension of the perforated pipe obtained through trial-and-error is shown in Fig. A1. Both of the criteria in Eq. (A1) are met and the ratios are actually smaller than 0.06. The percentage of maldistribution between the first and the last outlets can be calculated by

$$\text{Percent maldistribution} = 100 \left(1 - \sqrt{1 - \frac{\Delta h_p}{\Delta h_o}} \right) \quad (A5)$$

The percentage of maldistribution of the present design is estimated to be smaller than three percent.

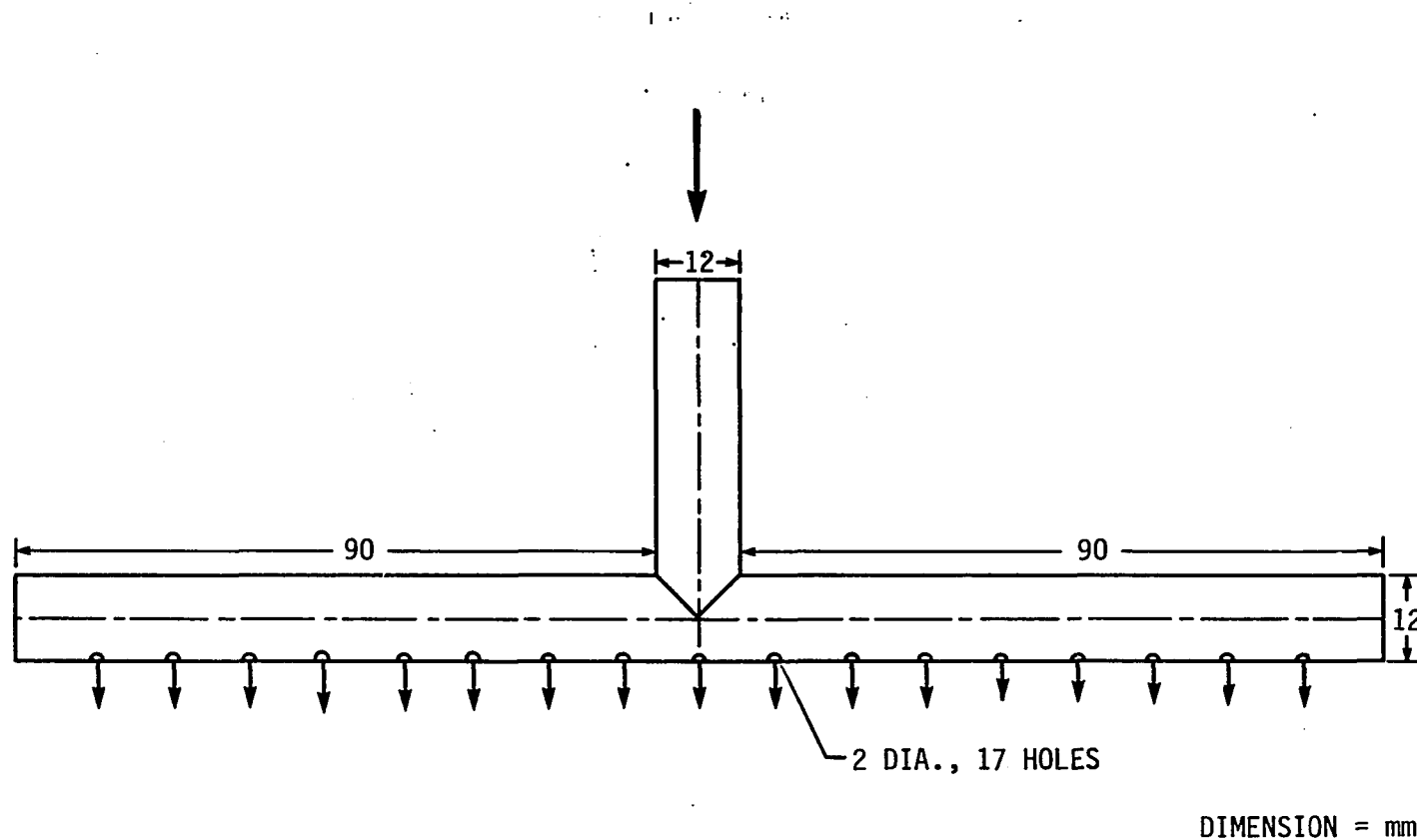


Fig. A1. Perforated-pipe fluid distributor

X. APPENDIX 2: LOCATING THE THERMOCOUPLES

A. Introduction

Test cylinders tested in the present study were drilled with thermocouple wells running axially at locations very close to the outer surface. The well must be small to minimize the disturbance of the temperature field. The well must also be deep enough so that the temperature measured by the thermocouple is free from end effects. With proper depth, the thermocouple lead loss is also minimized. In drilling such deep small-diameter holes, i.e., holes with small aspect (diameter-to-depth) ratio, failure to achieve a straight hole results in so-called drift or runout.

Usually, the displacement of the bottom of the hole is difficult to measure quantitatively. One possibility is to use a drilling technique which can be depended upon to yield sufficiently straight holes, and let the displacement of the bottom stand as a limited error after the degree of straightness has been checked by suitable means. To check the straightness of the hole, the conventional way is to use a piece of drill rod, longer than the depth of the hole and slightly smaller in diameter, with rounded ends. Failure of the rod to drop freely to the bottom of the hole should be taken as evidence that the hole is not straight. In the present case, it was necessary to accept the hole as it is anyway, even though it was usually not straight. There was a sizeable expense involved in drilling each hole, and it was undesirable to have too many abandoned holes in the cylinder since this would disturb the temperature distribution. However, it is important to locate the bottom of the hole where the thermocouple junction will be placed and the local temperature measured. Of critical

importance is the radial distance between the thermocouple junction and the outer surface of the cylinder. This distance is used to calculate the conduction temperature drop, which corrects the measured temperature to obtain the true surface temperature.

Ultrasonic technique and X-ray radiography performed at the Ames Laboratory, were tried as locating techniques in the present study. They worked for the cylinder with a plain surface, but not for those cylinders having structured surfaces. In this section, a novel method is presented which uses only rods to measure the required radial distance.

B. Method

The present method features inserting a rod down to the bottom of the hole, estimating the slope of the rod with a gauge in alignment with the tube surface, and calculating the distance between the surface and the bottom of the hole. As shown in Fig. A2(a), the rod A is placed in the hole, and B is the gauge in contact with the tube surface. The rod A must have a diameter considerably smaller than the hole, and it must be pushed outwards radially, so that one end of the rod is in contact with the lateral surface of the hole. The other point of contact is at the mouth of the hole. There should be only two points of contact, even if the hole is slightly curved.

An arbitrary point P is taken on gauge B, and d , d_2 , and l_2 are measured, as shown in Fig. A2(b) and (c). A toolmaker's microscope was used in the present measurement. By considering at the exaggerated geometry as shown, the distance between the bottom of the hole and the tube

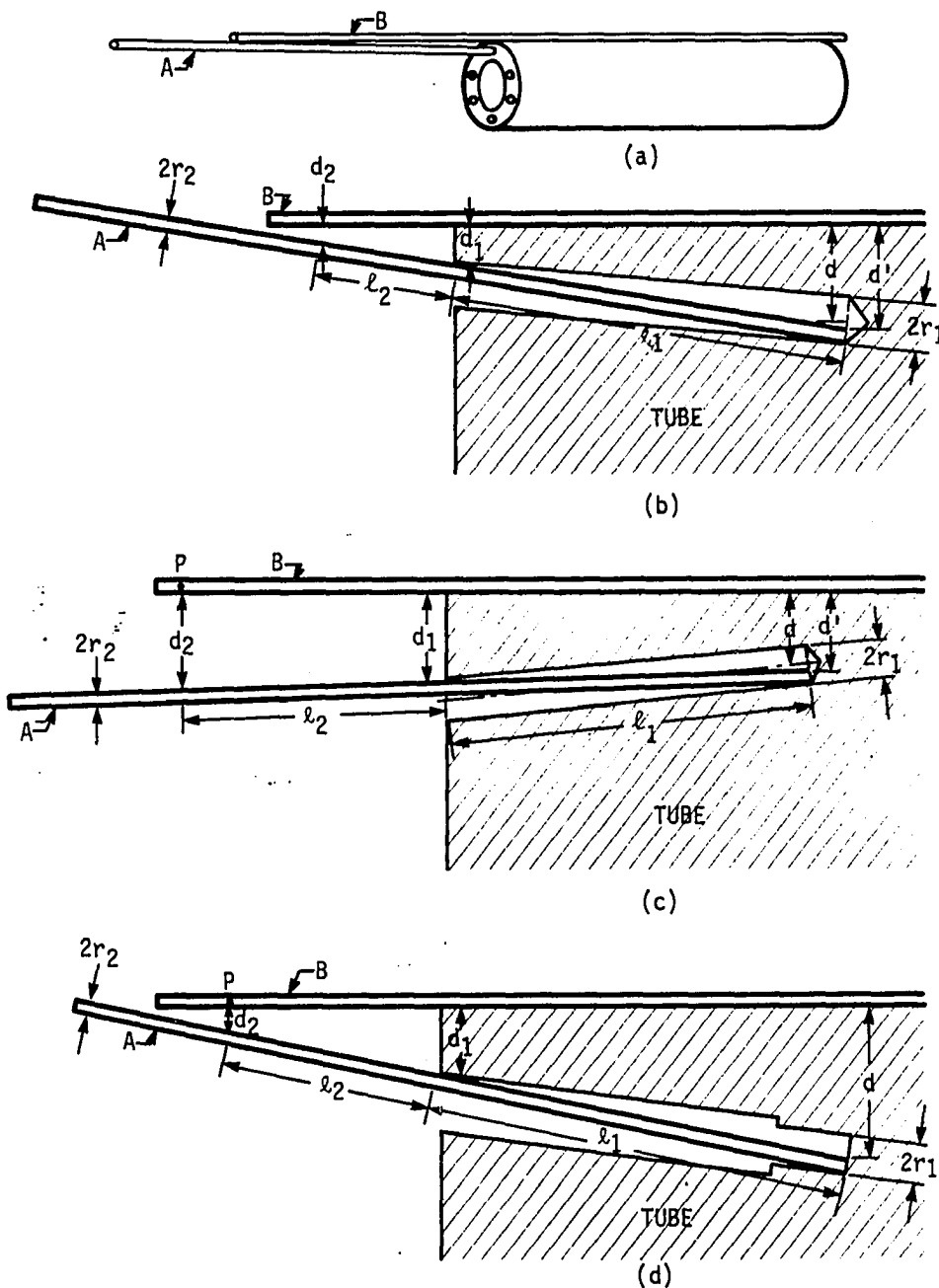


Fig. A2. Technique to measure the radial distance between the bottom of thermocouple well and the tube surface
(not to scale)

surface can be expressed as

$$d = (d_1 - d_2)(l_1/l_2) + d_1 - r_1 + 2r_2 \quad (A6)$$

with r_1 and r_2 the radius of the hole and the rod, respectively. Equation (A6) is true for the hole to drift radially either inwards or outwards, as shown in Figs. A2(b) and (c), respectively.

For those thermocouple walls prepared by two stages of drilling, as shown in Fig. A2(d), eq. A6 is still valid. Note that the radius of the bottom instead of the mouth should be taken as r_1 in this case.

XI. APPENDIX 3: CALIBRATION OF INSTRUMENTS

A. Calibration of Temperature Measurement System

1. Introduction

The temperature measurement system employed in the present study was composed of thermocouple junctions; an electronic reference junction Kaye Instrument Model K170-36C; an A/D converter, Hewlett-Packard Model 3490A; a scanner, Hewlett-Packard Model 341SA; a mini-computer, Hewlett-Packard Model 9825A; and a printer, Hewlett-Packard Model 9871A. The process of temperature measurement consists of the A/D converter reading the voltage between the thermocouple junction and the ice-point reference through the scanner and then having the computer convert the digitized emf reading from the A/D converter to temperature. The sources of error in the system could be the thermocouple wire, ice-point reference, A/D converter, and the function which the computer uses to convert emf to temperature. Instead of calibrating those components individually, the system was calibrated as a whole to obtain more reliable error information.

Thermocouple junctions prepared by segments of matched strands of wire from the same spool need not be calibrated individually. Usually, couples are taken from each end of a pair of strands, or, if it is very long, at suitable intervals. Any discrepancy among the calibration data of these thermocouples made from the same pair of strands will be indicative of a gradual change in thermoelectric properties along the length.

2. Calibration

a. Experiment Readings of the present temperature measurement system were compared with those of a precision mercury-in-glass type

thermometer with both the thermocouples and the thermometer immersed in a constant temperature oil bath, as shown in Fig. A3. Thermocouples to be calibrated were attached to the bulb of the thermometer to make sure the same temperature was sensed all the time. Five thermocouples formed by segments taken from matched strands of copper-constant wire (Omega, AWG 24) of 300 feet. As specified by the manufacturer, there was a knot at 82 feet. Hence, two thermocouples were formed by segments of wire from each end of the 82 foot wire, designated as T/C 1 and T/C 2. The other three thermocouples, T/C 3, T/C 4, and T/C 5 were from one end, the center, and the other end of the 218 foot wire, respectively. The calibration standard was a Brooklyn Thermometer mercury-in-glass precision thermometer, ranging from 167 to 221°F, with accuracy of $\pm 0.02^{\circ}\text{F}$. The thermometer was calibrated for total immersion. However, it was necessary to have a portion of the column protrude in order to take accurate readings.

Correction for the total-immersion thermometer used at condition of partial immersion was determined by attaching a small auxiliary thermometer to the center of the emergent stem of the thermometer to be corrected, as in Fig. A3. The mean temperature of the emergent stem was thus measured by the auxiliary thermometer. The correction may be calculated from

$$\text{Correction} = 0.00009N(T - T_{\text{aux}}) \quad (\text{A7})$$

for a Fahrenheit thermometer, where T is the main thermometer reading, and T_{aux} the auxiliary thermometer reading. N is the number of scale degrees equivalent to the emergent stem length, in °F. The correction was added to the main thermometer reading to obtain the true temperature. The calibration data of correction vs. indicated temperature for the five

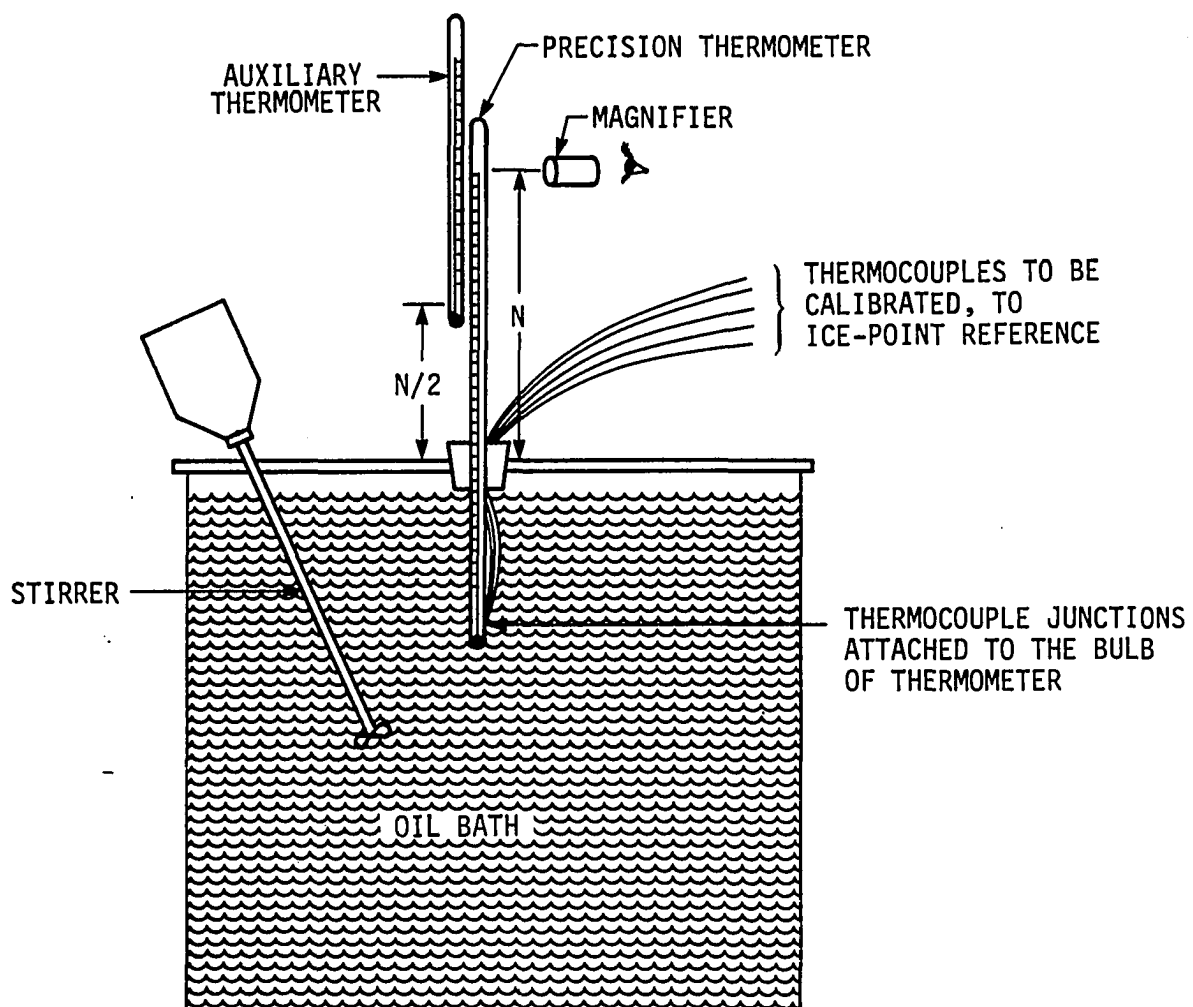


Fig. A3. Calibration of temperature measurement system

thermocouple samples were plotted in Fig. A4.

b. Statistics Based on the calibration data, a quadratic polynominal was taken to fit the data:

$$Y(x) = b_0 + b_1 x + b_2 x^2 \quad (A8)$$

where x is the indicated temperature, and $Y(x)$ the error between the indicated value and the true value. The least-squares criterion requires

$$\begin{aligned} b_0 n + b_1 \sum_{j=1}^n x_j + b_2 \sum_{j=1}^n x_j^2 &= \sum_{j=1}^n y_j \\ b_0 \sum_{j=1}^n x_j + b_1 \sum_{j=1}^n x_j^2 + b_2 \sum_{j=1}^n x_j^3 &= \sum_{j=1}^n x_j y_j \\ b_0 \sum_{j=1}^n x_j^2 + b_1 \sum_{j=1}^n x_j^3 + b_2 \sum_{j=1}^n x_j^4 &= \sum_{j=1}^n x_j = y_j \end{aligned} \quad (A9)$$

where n is the total number of data points. The parameters b_0 , b_1 , and b_2 were obtained from these equations. The least-squares fit of the 115 calibration data points for these particular five thermocouples is

$$T_{\text{true}} - T_{\text{ind}} = 1.2928 \times 10^{-5} (T_{\text{ind}})^2 - 0.0054138 (T_{\text{ind}}) + 0.17848 \quad (A10)$$

where temperatures are in °F, and T_{ind} denotes temperature indicated by the measurement system. This expression takes care of the systematic error or the bias of the temperature measurement system. It is still necessary to define the imprecision due to random error or nonrepeatability.

The confidence interval for a predicted y at a specified x value is

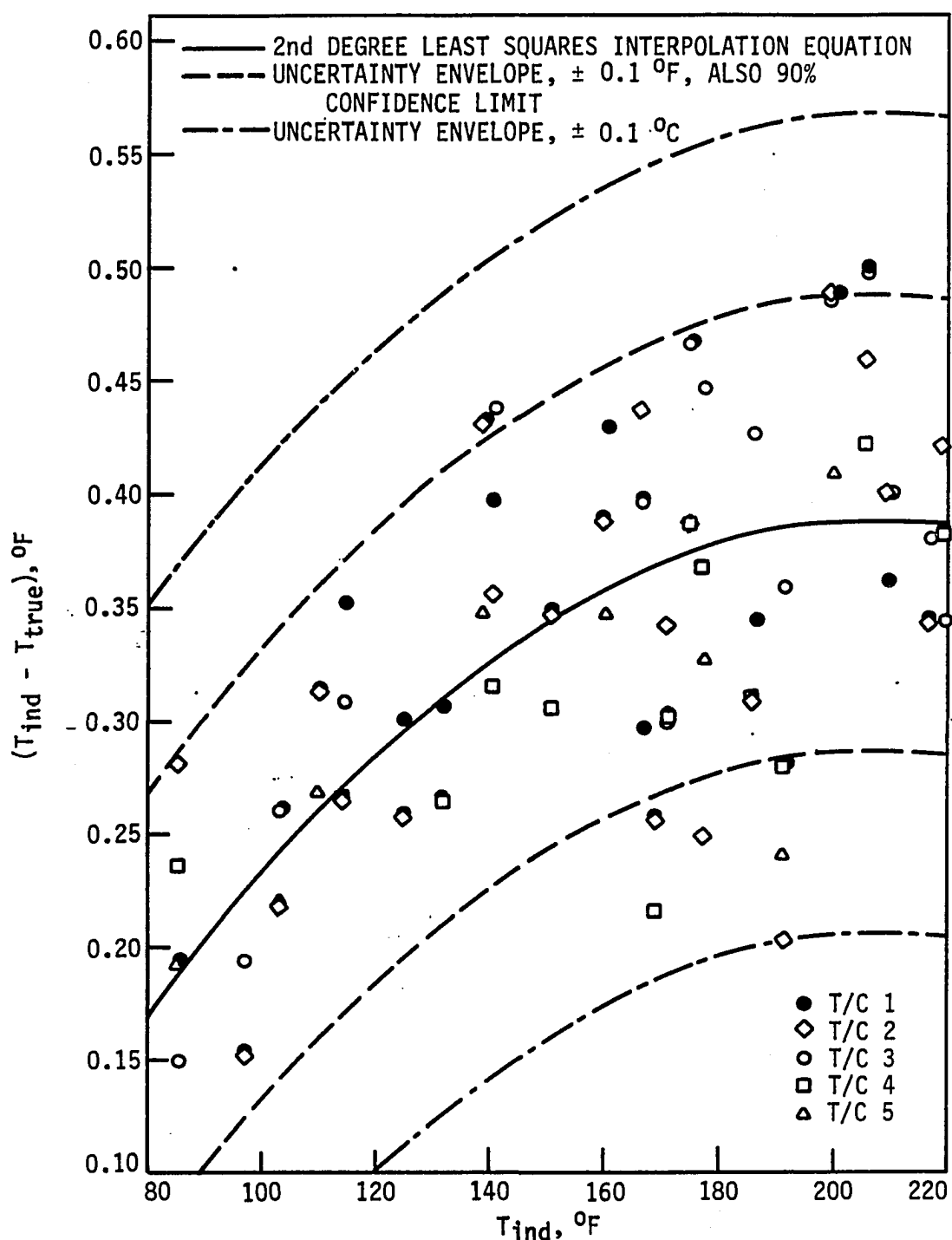


Fig. A4. Calibration curve for temperature measurement system

given as [72]

$$\hat{y}_{(x)} - A < y < \hat{y}_{(x)} + A \quad (\text{A11})$$

where \hat{y} = predicted value of y at x

$$A = t_{\alpha/2; (n-2)} \cdot S_{yx} \cdot i + \frac{1}{h} + \frac{(X - \bar{X})^2}{\sum_{i=1}^n (X_i - \bar{X})^2}$$

t = Student's t statistic

$1-\alpha$ = confidence level

S_{yx} = the standard deviation of y for x

$$= \frac{\sum_{i=1}^n (y_i - \hat{y}_i)^2}{n-3}$$

It was calculated that the 90 percent confidence limits were at $\pm 0.1^\circ\text{F}$ for the calibrated temperature measurement system, as shown in Fig. A4. It was also shown that all the data points were covered by an uncertainty envelope of $\pm 0.1^\circ\text{C}$.

3. Conclusion

The temperature measurement system using thermocouple junctions formed by segments of wire from this particular spool will have an accuracy of $\pm 0.1^\circ\text{F}$ as the 90 percent confidence limits, after the correction given by eq. (A10) is considered.

B. Calibration of Wattmeter

The wattmeter (Weston Model 310) employed in the present study was

calibrated at the Electronic Services of the Engineering Research Institute. The average calibration curve obtained by linear regression with least-squares criterion was

$$P_{\text{true}} = 1.027P_{\text{ind}} - 0.002867 \quad (\text{A12})$$

where P's are in kW, and P_{ind} denotes the power indicated by the wattmeter. The confidence limits were estimated by eq. (A11). At low wattage, the inaccuracy is dominated by the imprecision of the wattmeter, as is estimated by eq. (A11) while at high wattage, the uncertainty of calibration standard power dominates. The error of the wattmeter was taken as $\pm 2.5\text{W}$ throughout the range of test.

C. Calibration of Flowmeter

The flowmeter employed in the current study was a Brooks Full-View Rotameter, Model 1110, Size 8, with tube size of $\frac{1}{2}$ in., and a Type RV, rib-guided viscosity immune float. It was calibrated by passing water at a constant flowrate through the flowmeter, and weighing the collected water over a specified time interval. Before calibration, a limitation set by the manufacturer was checked to determine whether the viscosity of the metered liquid would permit calibration with water at room temperature. The calibration data were very well fitted by a straight line. The average calibration curve obtained by linear regression with the least-squares criterion was

$$Q_c = 7.928 \times 10^{-3} x + 0.02421 \quad (\text{A13})$$

with Q_c the flowrate of water at room temperature used for calibration, in GPM, and x the flowmeter reading in percent. The 90 percent confidence limits estimated by eq. (A11) were ± 0.02 GPM.

To convert the flowrate of calibrating liquid to that of the metered liquid, which is water at about 90°C , a sizing factor is required:

$$SF = \frac{(S_{f_1} - S_{l_1})S_{l_2}}{(S_{f_2} - S_{l_2})S_{l_1}} \quad (\text{A14})$$

where

S_{f_1} = specific gravity of the float material used for calibration

S_{f_2} = specific gravity of the material of float used when the flowrate of process fluid is measured

S_{l_1} = specific gravity of calibrating liquid, water at room temperature for the present case

S_{l_2} = specific gravity of metered liquid, water at 95°C for the present case

The flowrate of metered fluid is related to that of the calibrating fluid by the sizing factor:

$$Q_m = \frac{Q_c}{SF} \quad (\text{A15})$$

with Q_m the volume flowrate of metered fluid.

XII. APPENDIX 4: HEAT CONDUCTION STUDY OF THE TEST SECTION

A. Effect of Axially Non-Uniform Heat Flux Distribution at Inner Surface

1. Introduction

The axial non-uniformity in heat flux distribution within the hollow copper cylinder is mainly due to the existence of the non-heating zones in the commercial heater set in the tube. The detailed sketch of the structure of the cartridge heater based on the information provided by the manufacturer under special request is shown in Fig. A5. This sketch is quite different than that given in the commercial catalog prepared by the manufacturer. The discrepancy between the real heater structure and that described in the catalog was first discovered by boiling a bare heater in the water and observing the region where nucleate boiling took place. Regions with less nucleation going on obviously corresponded to gaps in the tightly wound resistance wire. An extra inactive zone other than those described in the catalog was located in this test. The exact length of inactive zones was obtained from the manufacturer, because the length obtained by measuring the nucleating zone of the heater in a boiling test would not have been accurate.

The sketch shows three essentially inactive zones in the heater: two of about the same length at each end, and another short one at the center. The inactive zones at the ends are necessary to keep the winding from touching the sheath; the middle one is introduced because two parallel the windings are connected there. It is necessary to understand how the longitudinal heat flux distribution in the test cylinder is influenced by the non-heating zones in the heater. Although this seems to be a rather

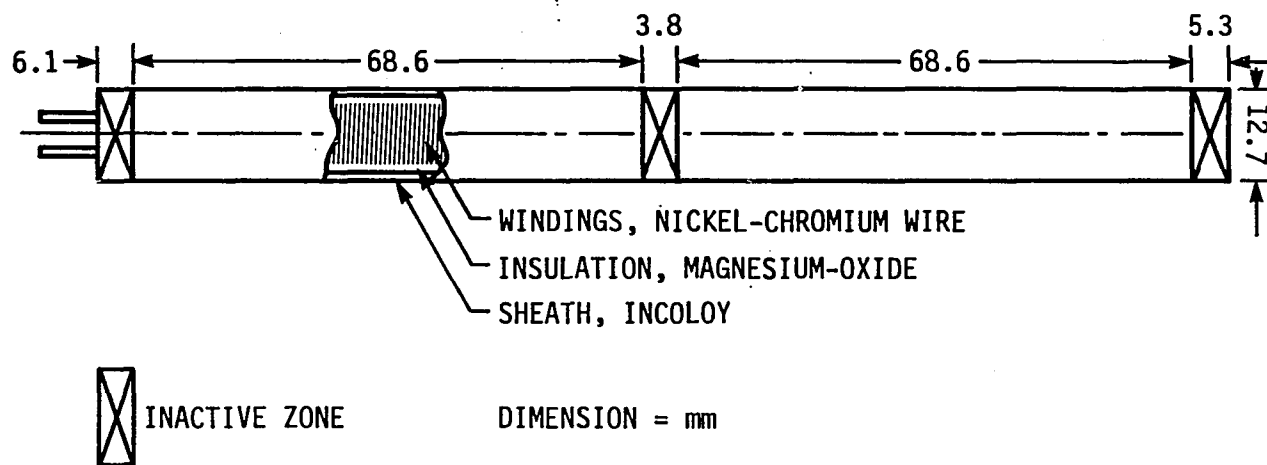


Fig. A5. Watlow Firerod J6A36 Cartridge Heater, 1kW, 240v

common situation in engineering practice, no existing solution to the problem seemed to be available.

2. Analytical solution

The two-dimensional (r, z), steady heat conduction problem in cylindrical coordinates will be solved here. By symmetry, the domain of interest can be limited to a section between the centers of the central inactive zone and the active section shown as Section AB in Fig. A6. The following boundary value problem was developed by assuming uniform heating in the active zone and no longitudinal heat transfer across the center planes of the active and inactive zones:

$$\begin{aligned} \frac{\partial^2 T}{\partial r^2} + \frac{1}{r} \frac{\partial T}{\partial r} + \frac{\partial^2 T}{\partial z^2} &= 0, \quad R_i < r < R_o, \quad 0 < z < 1 \\ \frac{\partial T}{\partial z} &= 0 \text{ at } z = 0, 1 \\ -k \frac{\partial T}{\partial r} &= h(T - T_\infty) \text{ at } r = R \\ -k \frac{\partial T}{\partial r} &= f(z) = \begin{cases} 0, & 0 < z < a \\ q_i'', & a < z < 1 \end{cases} \end{aligned} \tag{A16}$$

By letting $\tau = T(r, z) - T_\infty$, the problem can be reduced to

$$\frac{\partial^2 \tau}{\partial r^2} + \frac{1}{r} \frac{\partial \tau}{\partial r} + \frac{\partial^2 \tau}{\partial z^2} = 0, \quad R_i < r < R_o, \quad 0 < z < 1 \tag{A17a}$$

$$\frac{\partial \tau}{\partial z} = 0 \text{ at } z = 0, 1 \tag{A17b}$$

$$-k \frac{\partial \tau}{\partial r} = h\tau \text{ at } r = R_o \tag{A17c}$$

$$-k \frac{\partial \tau}{\partial r} = f(z) = \begin{cases} 0, & 0 < z < a \\ q_i'', & a < z < 1 \end{cases} \text{ at } r = R_i \tag{A17d}$$

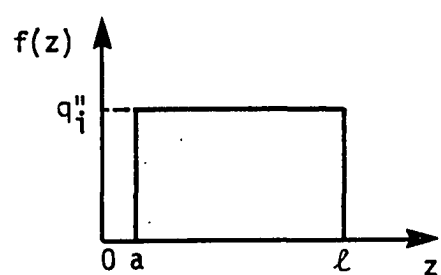
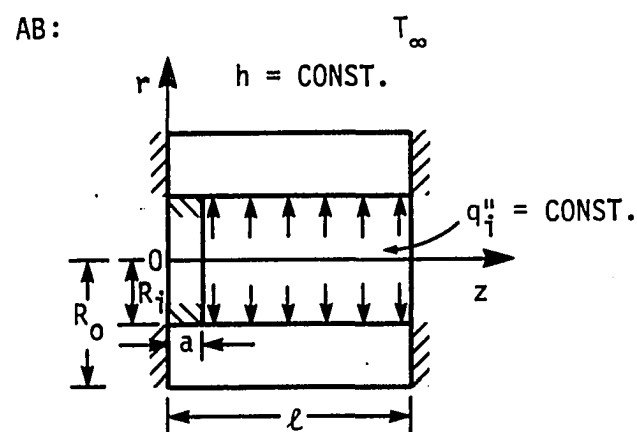
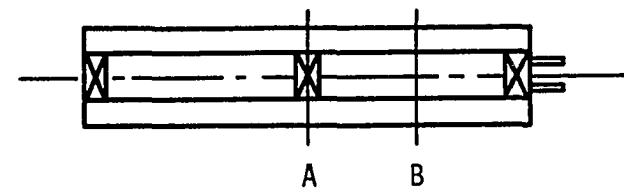


Fig. A6. Heat conduction problem with step change in heat flux at inner boundary of a hollow cylinder

To solve this problem, we assume the separability of the function $\tau(r, z)$ into an r - and a z -dependent functions in the form

$$\tau(r, z) = R(r) Z(z) \quad (A18)$$

the substitution of eq. (A18) into eq. (A17a) yields

$$\frac{1}{rR} \frac{d}{dr} (rR') = - \frac{Z''}{Z} \quad (A19)$$

In this equation, the left-hand side is a function of r , and the right-hand side is a function of z . Therefore, both sides must be equal to a separation constant λ^2 ; thus,

$$\frac{d}{dr} (rR') - \lambda^2 rR = 0 \quad (A20)$$

and

$$Z'' + \lambda^2 Z = 0 \quad (A21)$$

Eq. (A21) can be solved as

$$Z(z) = C_1 \cos \lambda z + C_2 \sin \lambda z \quad (A22)$$

with C_1 and C_2 constants. The boundary condition as described by eq. (A17b) requires $C_2 = 0$ and

$$Z_n(z) = C_1 \cos \lambda_n z \quad (A23)$$

with the eigenvalues

$$\lambda_n = \frac{n\pi}{l}, \quad n = 0, 1, 2, 3, \dots \quad (A24)$$

At $n = 0$, eq. (A20) gives

$$\frac{d}{dr}(rR') = 0 \quad (A25)$$

The boundary condition at $r = R_o$ as described by eq. (A17c) gives

$$R' + \frac{h}{k} R = 0 \text{ at } r = R_o \quad (A26)$$

The $R(r)$ at $n = 0$ is then solved as

$$R_o(r) = C_2 \left[\ln\left(\frac{r}{R_o}\right) - \frac{k}{h} \right] \quad (A27)$$

with C_2 constant. For $n \neq 0$, eq. (A20) is a modified Bessel function of order zero. Along with the boundary condition given by eq. (A26), $R_n(r)$ is solved as

$$R_n(r) = C_{3n} I_0(\lambda_n r) + C_{4n} K_0(\lambda_n r), \quad n = 1, 2, 3 \dots \quad (A28)$$

where C_{3n} and C_{4n} are constants, I_0 the modified Bessel function of the first kind of order zero and K_0 the modified Bessel function of the third kind of order zero. The complete solution for the temperature function $\tau(r, z)$ is constructed by a linear superposition of the above separated elementary solutions in the form

$$\begin{aligned} \tau(r, z) &= \sum_{n=0}^{\infty} R_n(r) Z_n(z) \\ &= C_5 \left[\ln\left(\frac{r}{R_o}\right) - \frac{k}{hR_o} \right] + \sum_{n=1}^{\infty} [C_{6n} I_0(\lambda_n r) + C_{7n} K_0(\lambda_n r)] \cos \lambda_n z \end{aligned} \quad (A29)$$

The substituting of eq. (A28) into the non-homogeneous boundary

condition given by eq. (A17d) yields

$$\begin{aligned} -\frac{kC_5}{R_i} &= k \sum_{n=1}^{\infty} [C_{6n} I_1(\lambda_n R_i) - C_{7n} K_1(\lambda_n R_i)] \lambda_n \cos \lambda_n z \\ &= \begin{cases} 0, & 0 < z < a \\ q_i'', & a < z < 1 \end{cases} \end{aligned} \quad (\text{A30})$$

where I_1 is the modified Bessel function of the first kind of order one, and K_1 , the modified Bessel function of the third kind of order one. The constants C_5 , C_{6n} , and C_{7n} can be obtained through the theory of Fourier series,

$$C_5 = -\frac{q_i'' R_i}{k} (1 - \frac{a}{l}) \quad (\text{A31})$$

$$\begin{aligned} C_{6n} &= 2q_i'' \sin(\lambda_n a) [\frac{h}{k} K_0(\lambda_n R_o) - \lambda_n K_1(\lambda_n R_o)] / k l \lambda_n^2 \{ [\frac{h}{k} K_0(\lambda_n R_o) \\ &\quad - \lambda_n K_1(\lambda_n R_o)] I_1(\lambda_n R_i) + K_1(\lambda_n R_i) [\frac{h}{k} I_0(\lambda_n R_o) + \lambda_n I_1(\lambda_n R_o)] \} \end{aligned} \quad (\text{A32})$$

$$\begin{aligned} C_{7n} &= -2q_i'' \sin(\lambda_n a) [\frac{h}{k} I_0(\lambda_n R_o) + \lambda_n I_1(\lambda_n R_o)] / k l \lambda_n^2 \{ [\frac{h}{k} K_0(\lambda_n R_o) \\ &\quad - \lambda_n K_1(\lambda_n R_o)] I_1(\lambda_n R_i) + K_1(\lambda_n R_i) [\frac{h}{k} I_0(\lambda_n R_o) + \lambda_n I_1(\lambda_n R_o)] \} \end{aligned} \quad (\text{A33})$$

By substituting eqs. (A31), (A32), and (A33) into equation (A29), the final form of the solution for temperature is obtained:

$$\begin{aligned} T(r, z) - T_{\infty} &= -\frac{q_i'' R_i}{k} (1 - \frac{a}{l}) (\ln \frac{r}{R_o} - \frac{1}{Bi_{R_o}}) \\ &\quad + \frac{2q_i'' l}{\pi^2 k} \sum_{n=1}^{\infty} [\frac{A_n}{n^2} I_0(\frac{n\pi r}{l}) + \frac{B_n}{n^2} K_0(\frac{n\pi r}{l})] \cos(\frac{n\pi z}{l}) \end{aligned} \quad (\text{A34})$$

Where $B_i_{R_o} = \text{radius Biot number} = \frac{hR_o}{k}$

I_0 = modified Bessel function of the first kind of order zero

K_0 = modified Bessel function of the third kind of order zero

$$A_n = \frac{1}{M} \sin\left(\frac{n\pi a}{1}\right) [B_{i_1} K_0\left(\frac{n\pi R_o}{1}\right) - n\pi K_1\left(\frac{n\pi R_o}{1}\right)]$$

$$B_n = -\frac{1}{M} \sin\left(\frac{n\pi a}{1}\right) [B_{i_1} I_0\left(\frac{n\pi R_o}{1}\right) + n\pi I_1\left(\frac{n\pi R_o}{1}\right)]$$

$$B_{i_1} = \text{length Biot number} = \frac{h_1}{k}$$

K_1 = modified Bessel function of the third kind of order one

I_1 = modified Bessel function of the first kind of order one

$$- M = I_1\left(\frac{n\pi R_i}{1}\right) [B_{i_1} K_0\left(\frac{n\pi R_o}{1}\right) - n\pi K_1\left(\frac{n\pi R_o}{1}\right)]$$

$$+ K_1\left(\frac{n\pi R_i}{1}\right) [B_{i_1} I_0\left(\frac{n\pi R_o}{1}\right) + n\pi I_1\left(\frac{n\pi R_o}{1}\right)]$$

And the solution for the radial heat flux distribution, obtained by partial differentiation of temperature with respect to r , is

$$\frac{q''(r,z)}{q''_1} = \frac{R_i}{r} \left(1 - \frac{a}{1}\right) - \frac{2}{\pi} \sum_{n=1}^{\infty} \left[\frac{A_n}{n} I_1\left(\frac{n\pi r}{1}\right) - \frac{B_n}{n} K_1\left(\frac{n\pi r}{1}\right) \right] \cos\left(\frac{n\pi z}{1}\right) \quad (A35)$$

where

$$q'' = \frac{\text{Total Power}}{2\pi \cdot R_i \cdot (1-a)} \quad (A36)$$

The temperature and radial heat flux distributions for the test cylinder and the commercial heater used in the present study were calculated by a computer and shown as an example in Figs. A7 and A8. The temperature distribution is, of course, most non-uniform near the inner surface of the cylinder ($r = R_1$). The distribution smooths out as the heat diffuses radially and axially towards the outer surface. The temperature approaches an asymptotic value with increasing distance from the non-heating zone, as shown by the profiles in Fig. A7. The radial heat flux distribution shown in Fig. A8, seems to converge to a constant value even more rapidly. The step change in heat flux at the inner surface is obviously smoothed out by the thick-walled tube used in the tests. The temperature and radial heat flux distributions at $r = 0.88 R_0$ are given special notice because this is the radial position where the thermocouples are inserted in the cylinder. The surface heat flux at the longitudinal position where the thermocouples were located was taken as the true heat flux for the data. The temperature drop over the distance between the thermocouple bead and the base surface can be calculated through eq. (A34).

B. Identification and Effect of the Circumferentially Non-Uniform Heat Flux Distribution at Inner Surface

1. Introduction

The non-uniformity of the circumferential heat flux distribution at the inner surface of the test tube may be due to the non-uniform heat flux generated by the commercial cartridge heater inserted in the tube, or the

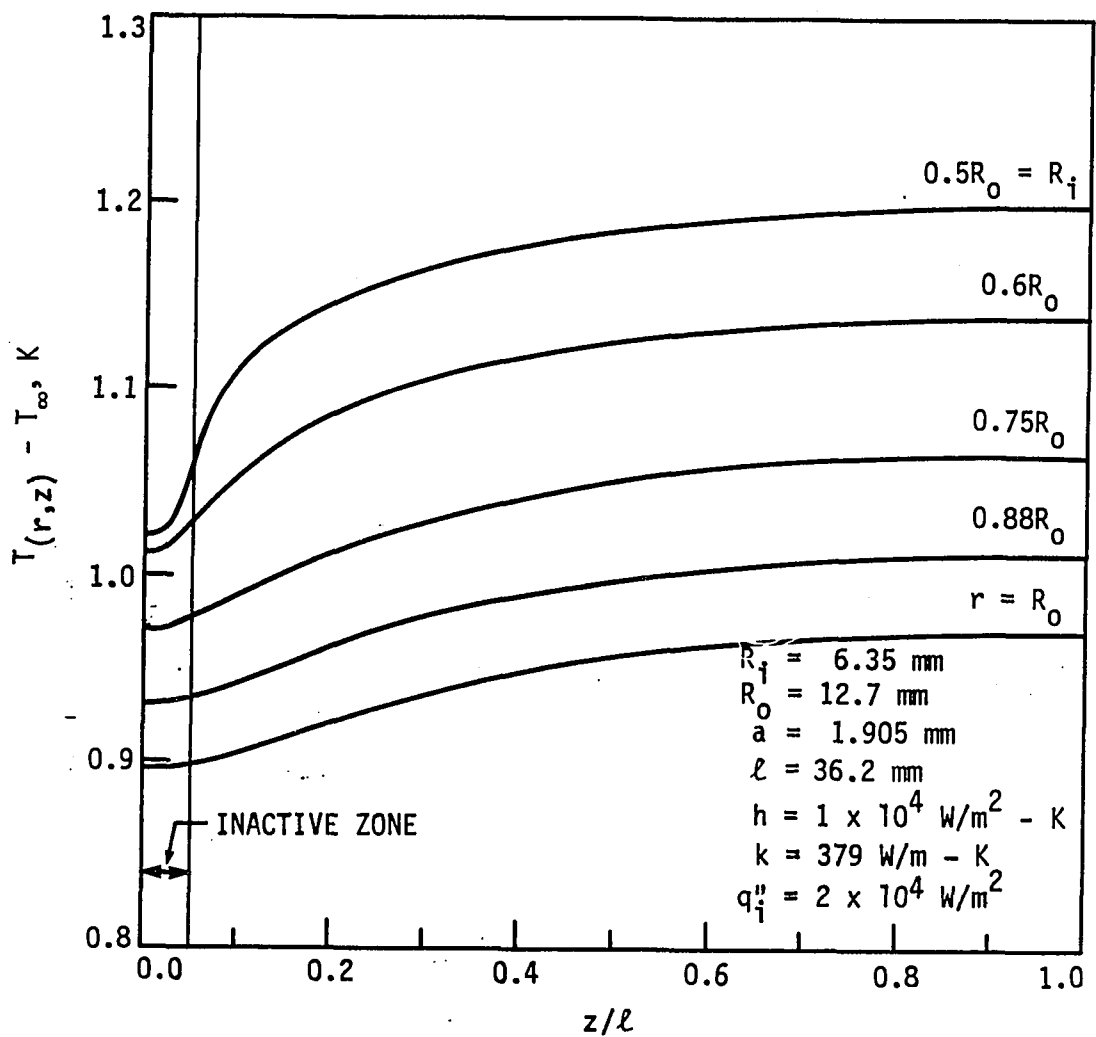


Fig. A7. Influence of inactive zone in the heater on the temperature distribution in the test cylinder

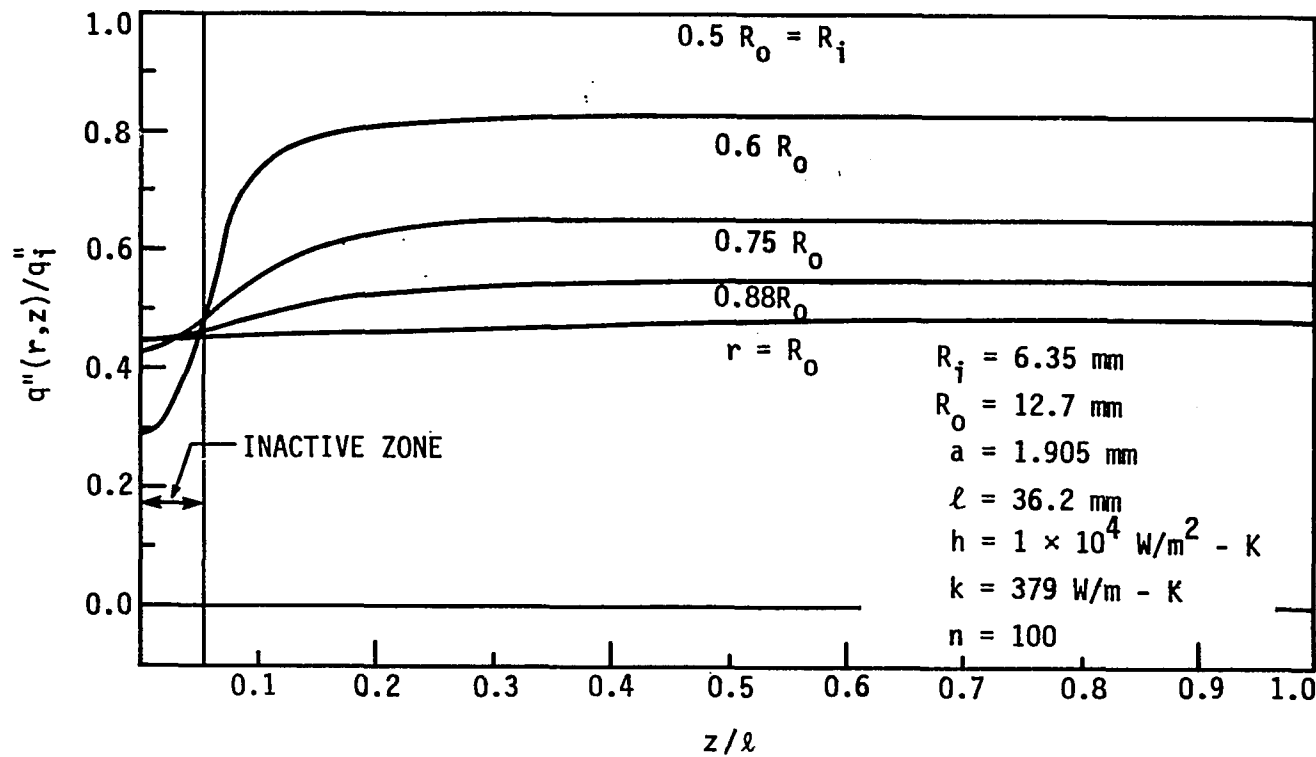


Fig. A8. Influence of inactive zone in the heater on the radial heat flux distribution in the test cylinder

uneven thickness of solder between the tube and the heater. The latter depends upon the clearance between the tube and heater, and is considered of minor significance since care was taken to get a good solder bond. The non-uniform circumferential heat flux of the commercial heater may be due to uneven thickness or compactness of the insulating powder between the heating coil and the sheath (Fig. A5).

Commercial cartridge heaters have been extensively used in heat transfer experiments for a long time. They have always been assumed to generate uniform heat fluxes axially and circumferentially, except near the ends. However, in the present study, a significantly non-uniform heat flux at the surface of a typical cartridge heater was observed. This was detected by observing the surface temperature distribution when the heat transfer coefficient at the surface of the heater was kept circumferentially uniform.

When a cartridge heater is installed in a hollow cylinder by soldering, the variation of heat flux at the inner surface of the cylinder due to the heater and/or solder can be analytically inferred by experimentally imposing a constant-heat-transfer-coefficient boundary condition at the outer surface and observing the surface temperature profile.

2. Analytical model

In this section, the steady-state heat conduction problem in a hollow cylinder with constant heat transfer coefficient at outer surface will be solved. A sinusoidal variation of heat flux at the inner surface is assumed for simplicity, although the real profile may not be sinusoidal. The maximum variation of heat flux at the inner surface, which one is most

interested in, can be learned from the present model by making this assumption.

The boundary value problem to be solved here is as shown below (Fig. A9):

$$\frac{\partial^2 T}{\partial r^2} + \frac{1}{r} \frac{\partial T}{\partial r} + \frac{1}{r^2} \frac{\partial^2 T}{\partial \theta^2} = 0 \quad 0 < \theta < \pi \quad (\text{A37a})$$

$$\left. \frac{\partial T}{\partial r} \right|_{r=R_o} = - \frac{h}{k} (T_{(R_o, \theta)} - T_\infty) \quad (\text{A37b})$$

$$\left. -k \frac{\partial T}{\partial r} \right|_{r=R_i} = \bar{q}_i'' + q_{iv}'' \cos m\theta = q_i'' \quad (\text{A37c})$$

$$\left. \frac{\partial T}{\partial \theta} \right|_{\theta=0} = \left. \frac{\partial T}{\partial \theta} \right|_{\theta=\pi} = 0 \quad (\text{A37d})$$

where \bar{q}_i'' is the average and q_{iv}'' the half amplitude of variation of the heat flux distribution at the inner boundary, and m is the number of variation cycles.

The problem is solved by assuming the separability of the function $T(r, \theta)$ into an r - and a θ -dependent functions in the form

$$T(r, \theta) = R(r) \cdot \Theta(\theta) \quad (\text{A38})$$

Substituting eq. (A38) into eq. (A37a) yields

$$\frac{r}{R} \frac{d}{dr} (rR') = - \frac{\Theta''}{\Theta} \quad (\text{A39})$$

In this equation, the left-hand side is a function of r , and the right-hand side a function of θ ; therefore, both sides must be equal to a separation constant λ^2 . This yields two ordinary differential

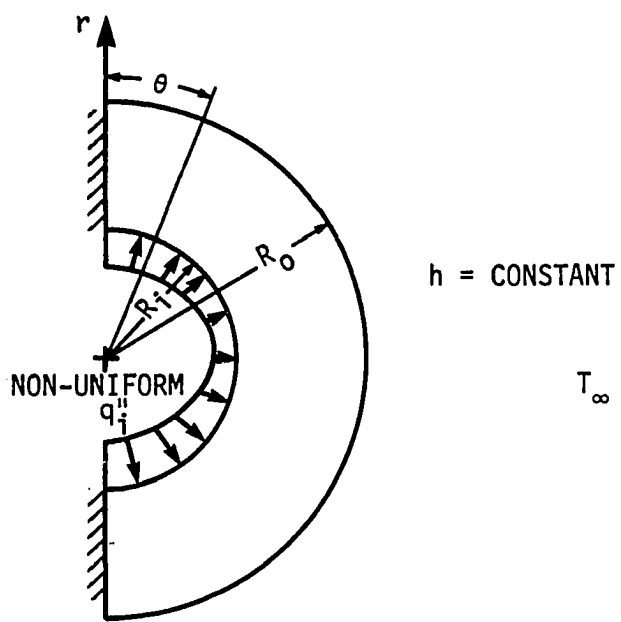


Fig. A9. Heat conduction problem with non-uniform heat flux at the inner boundary of a hollow cylinder

equations

$$r^2 R'' + rR' - \lambda^2 R = 0 \quad (A40)$$

and

$$\theta'' + \lambda^2 \theta = 0 \quad (A41)$$

The solution for θ is in the form

$$\theta_n(\theta) = C_1 \cos \lambda_n \theta + C_2 \sin \lambda_n \theta \quad (A42)$$

With C_1 and C_2 as constants. This reduces to the following solution by applying the boundary condition as given in eq. (A37d):

$$\theta_n(\theta) = C_1 \cos \lambda_n \theta \quad (A43)$$

where $\lambda_n = n$, $n = 0, 1, 2, 3\dots$ (A44)

For $\lambda_n = n = 0$, eq. (A40) reduces to

$$r^2 R'' + rR' = 0 \quad (A45)$$

This equation is readily solved as

$$R(r) = C_3 \ln r + C_4 \quad (A46)$$

with C_3 and C_4 as constants. For $n \neq 0$, eq. (A40) is solved by letting $R(r) = r^m$, with m a constant, and the solution is

$$R_n(r) = C_{5n} r^n + C_{6n} r^{-n}, \quad n = 1, 2, 3\dots \quad (A47)$$

with C_{5n} and C_{6n} as constants. The complete solution for the temperature function $T(r, \theta)$ is

$$T(r, \theta) = \sum_{n=0}^{\infty} R_n(r) \theta_n(\theta)$$

$$= a_0 \ln\left(\frac{r}{R_o}\right) + b_0 + \sum_{n=1}^{\infty} (a_n r^n + b_n r^{-n}) \cos n\theta \quad (A48)$$

with a_0 , b_0 , a_n , and b_n as constants. By applying the outer boundary condition eq. (A37b), the following relationships for the constants a_0 , b_0 , a_n , and b_n are obtained:

$$a_0 = \frac{R_o h}{k} (T_\infty - b_0) \quad (A49)$$

$$a_n = \frac{nk - hR_o}{nkR_o^{2n} + hR_o^{2n+1}} b_n \quad (A50)$$

More relationships are obtained by applying the inner boundary condition as described by eq. (A37c). Substituting eq. (A48) into eq. (A37c) yields

$$\begin{aligned} & \frac{a_0}{R_i} + \sum_{n=1}^{\infty} n(a_n R_i^{n-1} - b_n R_i^{-n-1}) \cos n\theta \\ &= -\frac{1}{k} (\overline{q_i''} + q_{iv}'' \cos m\theta) \end{aligned} \quad (A51)$$

By applying the theory of Fourier series, the constants are found to be

$$a_0 = -\frac{\overline{q_i''} R_i}{k} \quad (A52)$$

$$a_n = -\frac{q_{iv}''}{nk} + \frac{b_n R_i^{-n-1}}{R_i^{n-1}}, \quad n=m \quad (A53a)$$

$$a_n = \frac{b_n}{R_i^{2n}}, \quad n \neq m \quad (A53b)$$

For $n \neq m$, it yields the trivial solution $a_n = b_n = 0$. For $n = m$, the constants in eq. (A48) are obtained by solving eqs. (A49), (A50), (A52), and (A53a):

$$b_0 = \frac{\overline{q_i''} R_i}{h R_o} + T_\infty \quad (A54)$$

$$a_m = \frac{\overline{q_{iv}''}(km - hR_o)}{mkR_i^m \left\{ \left(\frac{R_o}{R_i}\right)^{2m} \left[\frac{km}{R_i} + h\left(\frac{R_o}{R_i}\right) \right] - \left[\frac{km}{R_i} - h\left(\frac{R_o}{R_i}\right) \right] \right\}} \quad (A55)$$

$$b_m = \frac{\overline{q_{iv}''} R_o^{2m} (km + hR_o)}{mkR_i^m \left\{ \left(\frac{R_o}{R_i}\right)^{2m} \left[\frac{km}{R_i} + h\left(\frac{R_o}{R_i}\right) \right] - \left[\frac{km}{R_i} - h\left(\frac{R_o}{R_i}\right) \right] \right\}} \quad (A56)$$

By substituting equations (A52), (A54), (A55), and (A56) into eq. (A48), the final form of the temperature function can be obtained as

$$\begin{aligned} T(r, \theta) - T_\infty &= -\frac{\overline{q_i''} R_i}{k} \ln \left(\frac{r}{R_o} \right) + \frac{\overline{q_i''} R_i}{h} \left(\frac{R_o}{R_i} \right) \\ &+ \frac{\overline{q_{iv}''} \left[r^{2m} (m-B_i) + R_o^{2m} (m+B_i) \right]}{mkR_i^{m-1} r^m \left[\left(\frac{R_o}{R_i}\right)^{2m} (m+B_i) - (m-B_i) \right]} \cos m\theta \end{aligned} \quad (A57)$$

Where $Bi = \text{Biot number} = \frac{hR_o}{k}$. At $r = R_o$, the temperature distribution is

$$T(R_o, \theta) - T_\infty = \frac{\overline{q_i''} R_i}{h} \left(\frac{R_o}{R_i} \right) + \frac{2\overline{q_{iv}''} R_o^m}{k R_i^{m-1} \left[\left(\frac{R_o}{R_i}\right)^{2m} (m+B_i) - (m-B_i) \right]} \cos m\theta \quad (A58)$$

Since the non-uniformity in the surface temperature $T(R_o, \theta)$ is solely

due to variations of the heat flux at the inner surface, a sinusoidal temperature variation at the outer boundary in phase with the q'' distribution at the inner boundary can be assumed:

$$T_{(R,\theta)} - T_\infty = \bar{T}_o + T_{ov} \cos m\theta \quad (A59)$$

where \bar{T}_o is the average and T_{ov} the half amplitude of the variation of temperature distribution at the outer surface. By equating both variational terms of eqs. (A58) and (A59), the relationship between variations in the outer surface temperature and the inner heat flux is obtained as

$$q_{iv}'' = \frac{T_{ov} k R_i^{m-1}}{2 R_o^m} \left[\left(\frac{R_o}{R_i} \right)^{2m} (m+B_i) - (m-B_i) \right] \quad (A60)$$

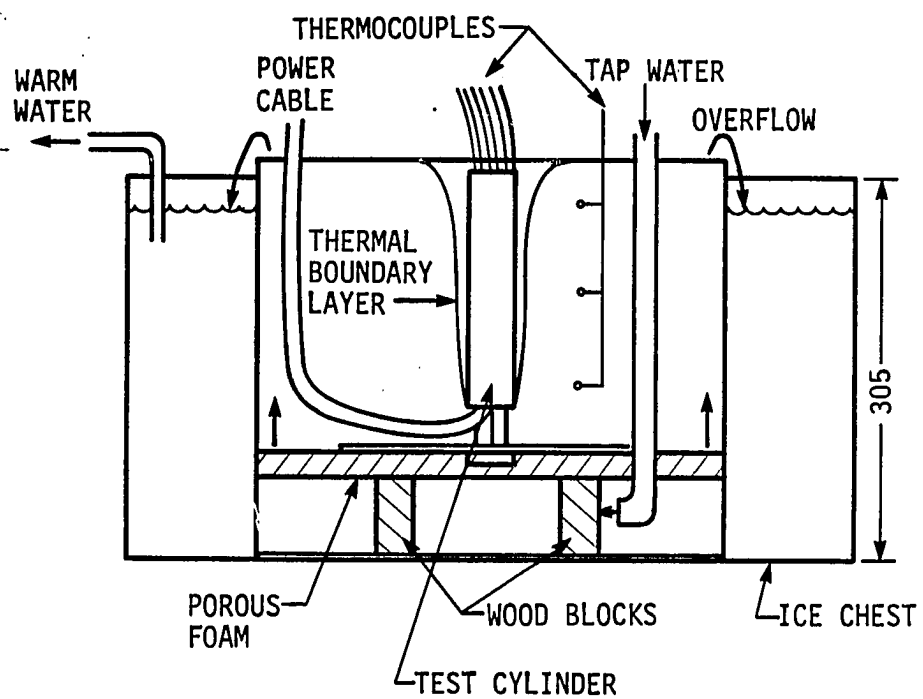
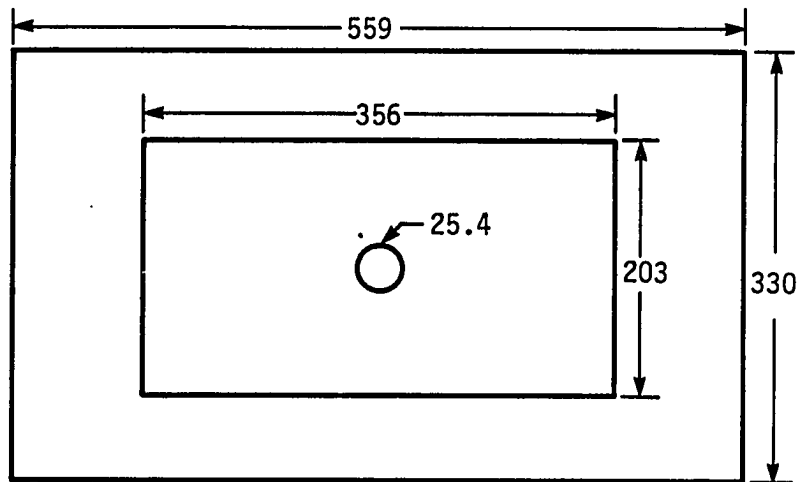
Eq. (A60) enables us to calculate the heat flux variation at the inner surface of the tube from the measured temperature variation at the outer surface. Looking at the special case where $R_i = R_o = R$, one can find that eq. (A60) becomes

$$q_{iv}'' = h \cdot T_{ov} \quad (A61)$$

This equation can be used to calculate the variation of heat flux on the sheath when a bare cartridge heater is arranged so that there is a constant heat transfer coefficient on the surface.

3. Experiment

The concern here is to design a simple test facility which provides the test tube with circumferentially uniform heat transfer coefficient at the outside surface. As shown in Fig. A10, the test section stood in the



DIMENSION = mm

Fig. A10. Test facility to investigate circumferential heat flux distribution at inner surface of the test tube

test chamber used in the falling-film evaporation tests as an inner chamber. The entire chamber was put in an ordinary ice chest insulated box. The thermocouple junctions in the wells of the test section were located at the same level. The test chamber was divided into two sections by a layer of porous foam material which was supported in place by two wood blocks. Tap water was directed into the compartment below the foam, and diffused through the foam to the upper section where the test tube was located. The warm water at the upper level overflowed to the ice chest. The water level in the test chamber was kept higher than the top of the test tube so that the tube would never become locally overheated by exposing part of the surface to the air.

The purpose of constantly adding cool tap water to the chamber was to keep the pool temperature steady; otherwise, the temperature of the pool would keep on rising due to heating by the test cylinder. The porous foam was there to attenuate any agitation introduced by the incoming tap water so that the velocity profile of the upward flow in the chamber was uniform. The inner chamber was large enough that the test tube was far away from the influence of the wall. The outer tank was used to collect the overflow from the inner chamber.

Before taking data, the test tube was rotated to check whether the surface temperature profile was affected by the local convective flow. An unchanged surface temperature profile meant circumferentially uniform heat transfer coefficient at the tube surface; thus, the surface temperature profile truly reflected the variation of heat flux at the inner surface of the tube.

The data acquisition system as described in Section IV-A-3 immediately

plotted the extrapolated circumferential temperature profile on the outside wall each time after the data was taken. Figure A11 shows a typical surface temperature profile obtained from the thermocouples.

A new commercial heater, Watlow Firerod J6A36, 1 kw, 240 v (same as that soldered in the tube), grooved longitudinally for the solder attachment of thermocouple junctions, was also tested to check the surface heat flux distribution. The bare heater was immersed as shown in Fig. A10. Eq. (A61) was used to estimate q''_{iv} .

4. Results and discussion

Based on the temperature profile in Fig. A11, which shows a full cycle of sinusoidal variation from $\theta=0$ to 2π with a half amplitude of about 0.5°C , one can determine that the number of variation cycles in $T(R_o, \theta)$ and q''_i equals unity, i.e., $m=1$. This was true for all the data taken, for either a heater inside a tube or a bare heater, although some showed profiles closer to a sinusoidal wave than the others. It was found that this may be due to the non-uniform thickness of insulation between the winding and the sheath (Fig. A5). Measurement of the magnesium-oxide insulation of a cut-off cartridge heater of the same model showed that the thickness changed cyclically from a maximum to minimum and back to maximum around the circumference, with the maximum value of 1.1340 mm and the minimum 0.9182 mm. This was obviously due to the eccentricity of the winding when it was placed in the sheath and packed with insulation. The cyclic variation of the insulation thickness was reflected by the temperature profile on the sheath surface.

When $m=1$, eq. (A60) becomes

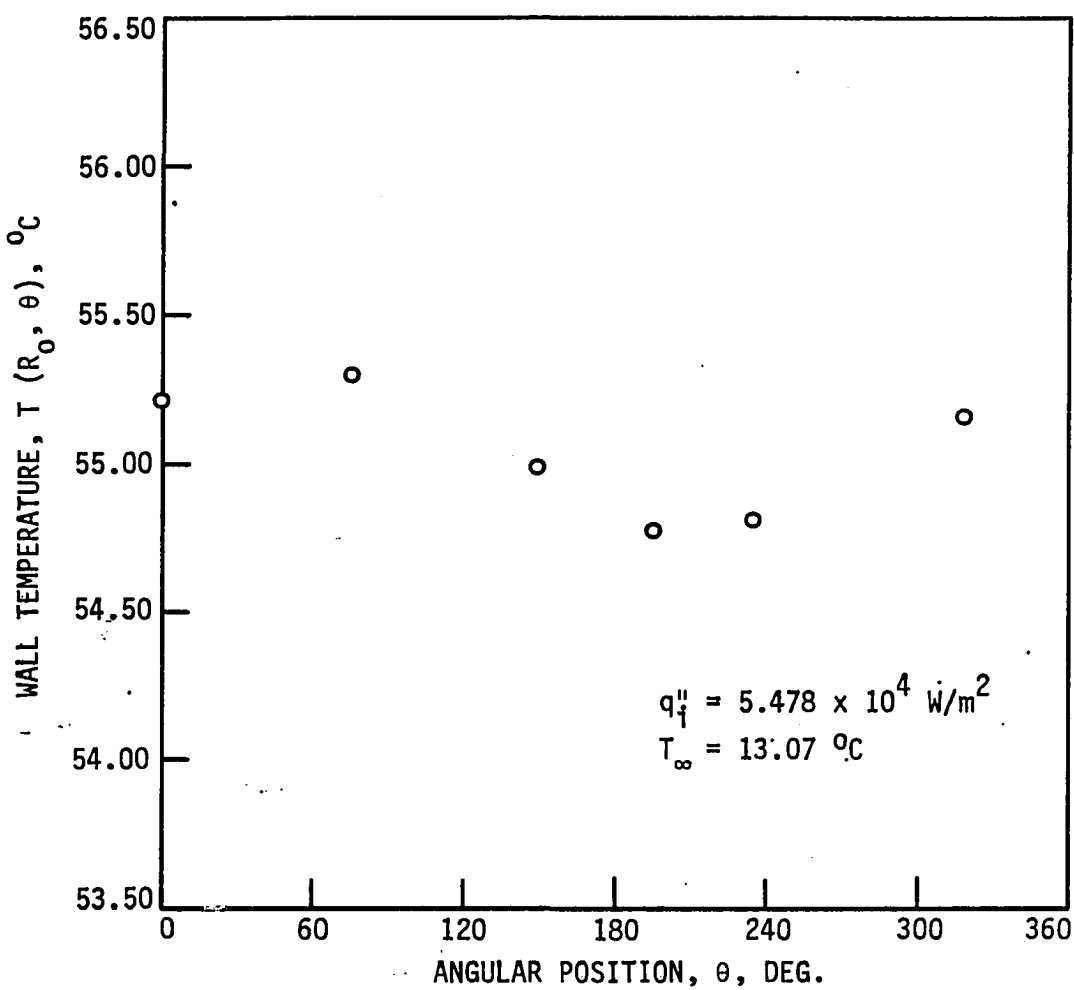


Fig. All. A typical circumferential temperature profile at the outside surface of the cylinder

$$q_{iv}'' = \frac{T_{ov}k}{2R_o} \left[\left(\frac{R_o}{R_i} \right)^2 (1+B_i) - (1-B_i) \right] \quad (A62)$$

Eq. (A62) was used to calculate the heat flux variation at the inner surface according to the measured temperature variation at the outside surface of the tube. The average surface and free stream temperatures were used to calculate the heat transfer coefficient:

$$h = \frac{\bar{q}_o''}{\bar{T}_o - \bar{T}_\infty} \quad (A63)$$

The test results revealed the surprising result that the inner heat flux distribution varied circumferentially in a range from ± 20 percent to ± 50 percent about the average. In the test using a bare commercial heater which had never been heated, the heat flux varied from as little as 3 percent at the beginning to 35 percent after eight manipulated heating-cooling cycles in 27 hours. While the cyclical variation form of the surface temperature kept unchanged, only the amplitude of variation increased. After running for 60 hours, power to the heater, indicated by the wattmeter, was observed to drop even though the voltage was controlled by a variac at a constant value. In the meantime, the resistance of the heater was found to have increased from the rated value of 57.6 ohm to 64 ohm. The drifting of power was always evident subsequently; it was, however, a slow process. The heater broke down (open circuited) after twelve heating-cooling cycles in between 62 and 70 hours.

It was evident that the non-uniformity of the heat flux on a commercial heater increases with number of heating-cooling cycles and/or

service time. Looking at the structure of a commercial heater as shown in Fig. A5, it is conceivable that the heating wire could separate from the insulation after a number of heating-cooling cycles over an extended service time, because of the difference in thermal expansion coefficients of the two materials. Once there is a gap in between, the radial heat flux from the wire to the insulation will be lower, resulting in a low local heat flux on the sheath surface. On the other hand, there will be a hot spot on the heating wire due to bad thermal contact. After more heating-cooling cycles, the gap between the wire and the insulation may become wider, making the radial heat flux more uneven, and the temperature of the hot spot on the heating wire even higher. Since the electric resistance of the heating wire rises with temperature, an increase in resistance and accordingly a decrease in power, as observed in the experiment, will take place. Finally, as the thermal contact between the wire and insulation becomes worse, the heater breaks down when the wire temperature reaches the melting point.

Since the insulation rips off from the winding due to difference in thermal expansion coefficients, the separation starts most likely at the location of the highest temperature on the winding. Due to the uneven thickness of the insulation, the point of the highest temperature on the winding locates at where the insulation thickness is the maximum and the temperature at outer surface is the minimum. As the gap between the heating wire and the insulation grows wider, the surface temperature at the corresponding point further decreases, whereas the maximum surface temperature further increases due to higher local heat flux. This results in an increase in the amplitude of variation while the wave form is

unchanged.

5. Conclusions

The variation of the outer surface temperature of the test cylinder employed in the present study due to the non-uniform heating by the commercial heater inserted is in the order of magnitude of 0.1°C , depending on the power level. This is a result of the circumferential variation of the heat flux on the heater sheath which can be as great as ± 50 percent of the average value. The non-uniformity increases with the number of heating-cooling cycles and/or service time. The thick-walled copper cylinder is an effective thermal equalizer which smooths out the substantial heat flux non-uniformity and reduces the temperature variation at the outer surface.

C. Effect of Circumferentially Non-Uniform Heat Transfer

Coefficient Distribution at Outside Surface

1. Introduction

When a horizontal tube is covered with an evaporating falling film, the heat transfer coefficient is circumferentially non-uniform, with a maximum at $\theta=0^{\circ}$ and a minimum at $\theta=180^{\circ}$. The circumferential heat transfer coefficient variation has been measured on a horizontal tube heated by conducting alternating current through the tube wall [5]. The influence of the non-uniform heat transfer coefficient on the temperature distribution within a thick-walled cylinder heated at the interior was clarified in the present study. First, the two-dimensional boundary value problem for a hollow cylinder with non-uniform heat transfer coefficient at the outer surface, and uniform heat flux distribution at the inner surface was

solved. However, the solution was implicit. The alternative way to solve the problem is to assume a non-uniform heat flux distribution instead of a non-uniform heat transfer coefficient distribution at the outer surface. The boundary value problem can then be solved explicitly, and the local heat transfer coefficient can be obtained by the local heat flux and temperature at the outer surface.

2. Analytical solution

The two-dimensional (r, θ) heat conduction problem in cylindrical coordinates is to be solved. The conduction equation and the boundary conditions are as follows (Fig. A12):

$$\frac{\partial^2 T}{\partial r^2} + \frac{1}{r} \frac{\partial T}{\partial r} + \frac{1}{r^2} \frac{\partial^2 T}{\partial \theta^2} = 0, \quad 0 < \theta < \pi \quad (\text{A64a})$$

$$\left. \frac{\partial T}{\partial r} \right|_{r=R_i} = - \frac{q_i''}{k}, \quad q_i'' = \text{constant} \quad (\text{A64b})$$

$$\left. \frac{\partial T}{\partial r} \right|_{r=R_o} = - \frac{1}{k} (q_o'' + q_{ov}'' \cos \theta) \quad (\text{A64c})$$

$$\left. \frac{\partial T}{\partial \theta} \right|_{\theta=0} = \left. \frac{\partial T}{\partial \theta} \right|_{\theta=\pi} = 0 \quad (\text{A64d})$$

The sinusoidal variation of heat flux at outer boundary agrees with the reported experimental result for the heat transfer coefficient profile at the outer surface of a horizontal tube [5]. The non-uniform heat flux at the outer boundary is a consequence of the non-uniform heat transfer coefficient distribution.

The solution of temperature distribution based on eqs. (A64a) and (A64d) was given by eq. (A48). Substituting eq. (A48) into

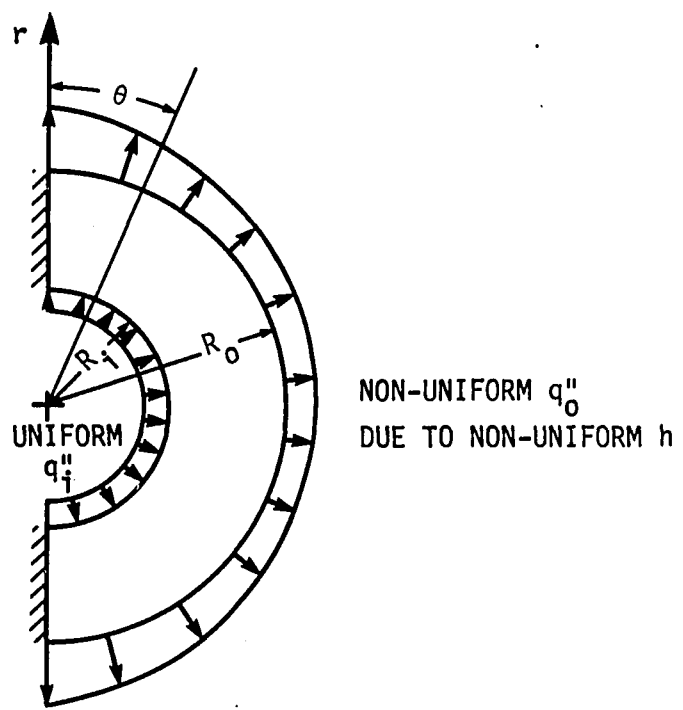


Fig. A12. Heat conduction problem with non-uniform heat flux at outer boundary of a hollow cylinder

eq. (A64b) yields

$$\frac{a_o}{R_i} + \sum_{n=1}^{\infty} n(a_n R_i^{n-1} - b_n R_i^{-n-1}) \cos n\theta = - \frac{q_i''}{k} \quad (A65)$$

By applying the theory of Fourier series one can have

$$a_o = - \frac{q_i'' R_i}{k} = - \frac{q_o'' R_o}{k} \quad (A66)$$

and

$$a_n = \frac{b_n}{R_i^{2n}} \quad (A67)$$

Substituting eq. (A48) into eq. (A64c) and applying the theory of Fourier series yields

$$a_n R_o^{n-1} - b_n R_o^{-n-1} = - \frac{q_{ov}''}{nk}, \quad n = m \quad (A68)$$

$$a_n = \frac{b_n}{R^{2n}}, \quad n \neq m \quad (A69)$$

For $n \neq m$, eqs. (A67) and (A69) yield the trivial solution $A_n = b_n = 0$.

For $n = m$, the constants A_n and b_n are obtained by solving eqs. (A67) and (A68):

$$a_m = - \frac{R_o^{m+1} q_{ov}''}{mk(R_o^{2m} - R_i^{2m})} \quad (A70)$$

$$b_m = - \frac{R_o^{m+1} R_i^{2m} q_{ov}''}{mk(R_o^{2m} - R_i^{2m})} \quad (A71)$$

By substituting eqs. (A66), (A70) and (A71) into eq. (A48), and the average temperature at outer surface, \bar{T}_o , for b_o , the final form of the temperature function is obtained as

$$\begin{aligned} T(r, \theta) - \bar{T}_o &= - \frac{\bar{q}_o'' R_o}{k} \ln(r/R_o) - \frac{R_o^2 q_{ov}''}{k(R_o^2 - R_i^2)} \left(r + \frac{R_i^2}{r} \right) \cos \theta \\ &= \bar{T}(r) + T_v(r) \cos \theta \end{aligned} \quad (A72)$$

At $r = R_o$,

$$\begin{aligned} T_{ov} &= T_v(R_o) \\ &= \frac{R_o(R_o^2 + R_i^2)}{k(R_o^2 - R_i^2)} q_{ov}'' \end{aligned} \quad (A73)$$

According to the definition of local heat transfer coefficient,

$$\begin{aligned} h(\theta) &= \frac{q''(R_o, \theta)}{\bar{T}(R_o, \theta) - T_\infty} \\ &= \frac{\bar{q}_o'' + q_{ov}'' \cos \theta}{(\bar{T}_o - T_\infty) - \frac{R_o^2 q_{ov}''}{k(R_o^2 - R_i^2)} \left(r + \frac{R_i^2}{r} \right) \cos \theta} \end{aligned} \quad (A74)$$

Since the constants of variation, q''_{ov} and T_{ov} , have opposite signs, the profiles of $q''_{ov}(\theta)$ and $T_{ov}(\theta)$ are out of phase, and $h(\theta)$ will be in phase with $q''_{ov}(\theta)$, as shown in Fig. A13. Therefore the maximum and minimum

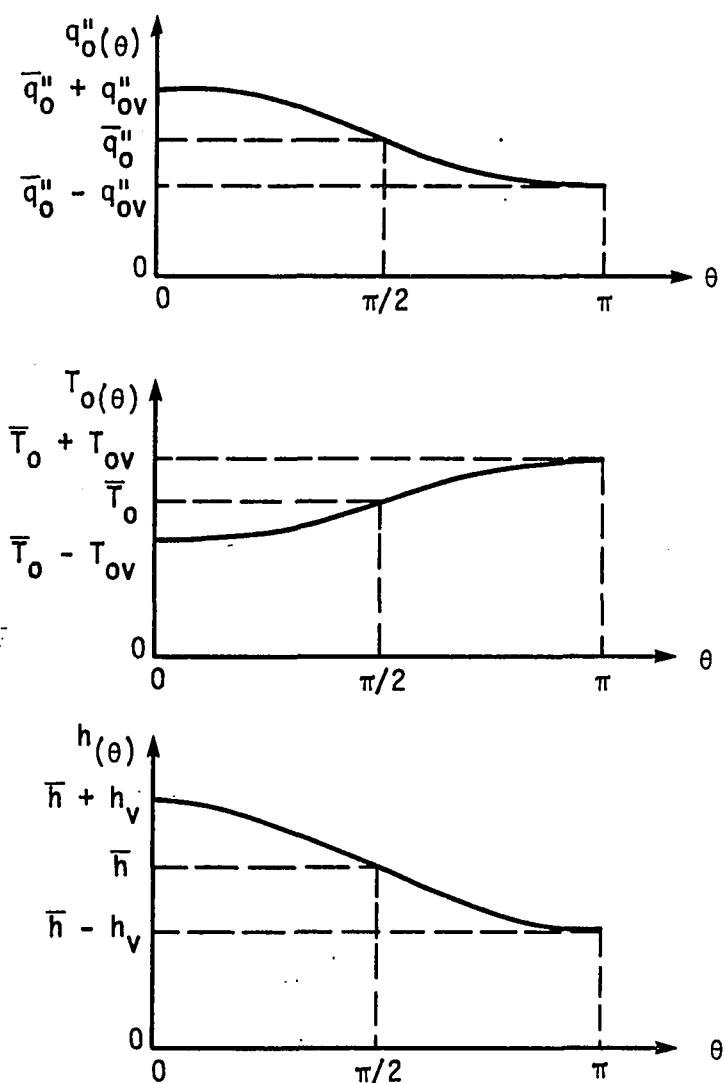


Fig. A13. Schematic profiles of heat flux, temperature, and heat transfer coefficient at the outer surface of the hollow cylinder

values of $h_{(\theta)}$ are at $\theta=0^\circ$ and $\theta=180^\circ$, respectively. The variational constant of $h_{(\theta)}$, h_v can be obtained as follows:

$$h_v = \frac{h_{\max} - h_{\min}}{2} = \frac{-\bar{\Delta T}_o (\bar{h}T_{ov} - q''_{ov})}{\bar{\Delta T}_o^2 - T_{ov}^2} \quad (A75)$$

where $\bar{\Delta T}_o$ is the difference between T_o and T_∞ . By assuming $(T_{ov})^2 \ll (\bar{\Delta T}_o)^2$, and substituting \bar{h} with a reasonable value for falling film evaporation and T_{ov} with the function of q''_{ov} given by eq. (A73), one can have a relationship between h_v and q''_{ov} . The relationship between T_{ov} and h_v can be obtained subsequently. Based on this relationship, one can estimate the circumferential variation of temperature at the outer surface of the tube due to the non-uniform heat transfer coefficient. The T_{ov} value is about 0.3°C if $\bar{h} = 10^4 \text{ W/m}^2\text{-K}$ and $h_v = 0.2 \text{ h}$ (estimated from the data of Ref. [5]).

3. Conclusions

The influence of the non-uniform heat transfer coefficient at the outer surface on the temperature distribution within a thick-walled cylinder heated at the interior was studied by solving the two-dimensional heat conduction problem in cylindrical coordinates. It was found that the variation of the outer surface temperature due to the non-uniform heat transfer coefficient distribution provided by the evaporating falling liquid film on the outer surface is in the order of magnitude of 0.1°C , depending on the average and variational values of the heat transfer coefficient.

XIII. APPENDIX 5: EXAMPLES OF COMPUTER PROGRAM FOR DATA ACQUISITION
AND REDUCTION

A. Computer Program for Falling Film Evaporation Test
with High Flux Surface

```

0: fmt 1," FFE-HF",/,/;wrt 6.1
1: dim A[30],W[30],T[30],V[30],S[12]
2: fmt 1,1x,"H",2x,"FLOW",4x,"ANGLE",5x,"HEAT",6x,"AVG",z
3: fmt 2,4x,"SAT",7x,"T1",5x,z
4: fmt 3,"T2",5x,"T3",5x,"T4",5x,"T5",5x,"T6",5x,z
5: fmt 4,"TS",10x,"T1",5x,"T2",5x,"T3",5x."SUBCL"
6: fmt 5,4x,"RATE",5x,"T11",6x,"FLUX",6x,"SPHT",3x,"TEMP"
7: fmt 6,"mm",2x,"KG/S-M",3x,"DGR",6x,"W/M^2",6x,"K",6x,"C",8x,"C",6x,"C",z
8: fmt 7,6x,"C",6x,"C",6x,"C",6x,"C",11x,"C",6x,"C",6x,z
9: fmt 8,"C",7x,"C",/
10: wrt 6.1;wrt 6.2;wrt 6.3;wrt 6.4;wrt 6.5;wrt 6.6;wrt 6.7;wrt 6.8
11: ent "LIQUID FEED FALLING DISTANCE?",r3
12: ent "FLOWMETER READING?",N
13: (1.1601224126e1*N+35.422884)/3600/2→M
14: ent "WATTMETER READING?",r1
15: ent "BAROMETER READING?",H
16: ent "ANGULAR POSITION OF T11?",r2
17: 1027.2121*r1-2.8667→P
18: 87.9*P→Q
19: fmt 6,f2.0,1x,z:wrt 6.6,r3
20: fmt 6,1x,e8.2,z;wrt 6.6,M
21: fmt 8,f4.0,z;wrt 6.8,r2
22: fmt 4,e13.3,z;wrt 6.4,Q
23: fmt 1,"C",fz2.0,"E",z
24: fmt 2,"F1R7A1H0M3T1",z
25: for I=1 to 19;wrt 709.1,I;wrt 722.2;red 722,V[I]
26: 'TEMP'(1000V[I])+A[I]
27: ('CALT'(A[I])-32)*5/9→W[I]
28: next I
29: W[1]-'COND'(1.27-.1509)→T[1]
30: W[2]-'COND'(1.27-.2057)→T[2]
31: W[3]-'COND'(1.27-.07795)→T[3]
32: W[4]-'COND'(1.27-.2041)→T[4]

```

```

33: W[5]-'COND'(1.27-.1796)→T[5]
34: W[6]-'COND'(1.27-.1436)→T[6]
35: W[7]-'COND'(1.27-.4186)→T[7]
36: W[8]-'COND'(1.27-.09942)→T[8]
37: W[9]-'COND'(1.27-.08509)→T[9]
38: W[10]-'COND'(1.27-.09914)→T[10]
39: W[11]-'COND'(1.27-.1402)→T[11]
40: W[12]-'COND'(1.27-.1338)→T[12]
41: ('TSAT'(.49115H)-32)*5/9+C
42: O→F;for I=1 to 12;T[I]-C→S[I];F+S[I]→F;next I
43: F/12→R
44: fmt 3,f7.2,z;wrt 6.3,R
45: wrt 6.3,C
46: fmt 2,"S1",z;wrt 6.2;for I=1 to 6;wrt 6.3,S[I];next I
47: W[13]-C→r6;wrt 6.3,r6;fmt 4,"AMBT",z;wrt 6.4
48: for I=14 to 16;wrt 6.3,W[I];next I
49: C-(W[14]+W[15]+W[16])/3→S;fmt 9,f8.2;wrt 6.9,S
50: fmt 1,44x,"S2",f7.2,z;wrt 6.1,S[7];for I=8 to 12;wrt 6.3,S[I];next I
51: fmt 2,7x,"DIST",z;wrt 6.2;for I=17 to 19;wrt 6.3,W[I];next I
52: C-(W[17]+W[18]+W[19])/3→S;wrt 6.9,S
53: gto 12
54: end
55: "CALT":
56: ret 1.29283e-5*p1*p1+.9945861644*p1+.1784832544
57: "COMD":
58: ret ln(1.27/p1)/379*.0127*Q
59: "TSAT":
60: ret 139.276781+6.4757873p1-.1036991p1p1
61: "TEMP":
62: if p1<=1.494;ret 31.99925+46.80117p1-1.407396p1^2+.07802p1^3-.007394p1^4
63: if p1<=3.941;ret 33.42956+44.48835p1-.07422p1^2-.253895p1^3+.02878p1^4
64: if p1<=6.62;ret 33.82822+45.39092p1-1.015078p1^2+.03592p1^3-.000642p1^4
*14727

```

B. Computer Program for Pool Boiling Test
with High Flux Surface

```

0: fmt 1,"PB-HF",/,/,/;wrt 6.1
1: dim A[30],W[30],T[30],V[30],S[12]
2: fmt 1,1x,"FLOW",4x,"ANGLE",5x,"HEAT",6x,"AVG",4x,"SAT",4x,"T1",5x,z
3: fmt 2,"T2",5x,"T3",5x,"T4",5x,"T5",5x,"T6",5x,z
4: fmt 3,"TS",5x,"P1",5x,"P2",5x,"P3",5x,"POOL"
5: fmt 4,"RATE",5x,"T11",6x,"FLUX",6x,"SPHT",3x,"TEMP",z
6: fmt 9,44x,"SPHT",25x,"SUBCL"
7: fmt 5,"KG/S-M",4x,"DGR",6x,"W/M^2",6x,"K",6x,"C",6x,"C",6x,"C",6x,"C",z
8: fmt 6,6x,"C",6x,"C",6x,"C",6x,"C",6x,"C",6x,"C",6x,z
9: fmt 7,"C",7x,"C",/
10: wrt 6.1;wrt 6.2;wrt 6.3;wrt 6.4;wrt 6.9;wrt 6.5;wrt 6.6;wrt 6.7
11: O→M
12: ent "WATTMETER READING?",r1
13: ent "BAROMETER READING?",H
14: ent "POOL LEVEL in CM?",K
15: ent "ANGULAR POSITION OF T11?",r2
16: 1027.2121*r1-2.8667→P
17: 87.9*P→Q
18: fmt 8,f4.0,z;wrt 6.8,M
19: fmt 9,f9.0,x;wrt 6.9,r2
20: fmt 1,e13.3,z;wrt 6.1,Q
21: fmt 1,"C",fz2.0,"E",z
22: fmt 2,"F1R7A1H0M3T1",z
23: for I=1 to 16;wrt 709.1,I;wrt 72.2;red 722,V[I]
24: 'TEMP'(1000V[I])→A[I]
25: ('CALT' (A[I])-32)*5/9→W[I]
26: next I
27: W[I]-'COND'(1.27-.1509)→T[1]
28: W[2]-'COND'(1.27-.2057)→T[2]
29: W[3]-'COND'(1.27-.07795)→T[3]
30: W[4]-'COND'(1.27-.2041)→T[4]
31: W[5]-'COND'(1.27-.1796)→T[5]
32: W[6]-'COND'(1.27-.1436)→T[6]

```

```

33: W[7]-'COND'(1.27-.4186)→T[7]
34: W[8]-'COND'(1.27-.09942)→T[8]
35: W[9]-'COND'(1.27-.08509)→T[9]
36: W[10]-'COND'(1.27-.09914)→T[10]
37: W[11]-'COND'(1.27-.1402)→T[11]
38: W[12]-'COND'(1.27-.1338)→T[12]
39: ('TSAT'(.49115H+.01363K)-32)*5/9+C
40: O→F;for I=1 to 12;T[I]-C→S[I];F+S[I]→F;next I
41: F/12→R
42: fmt 3,f7.2,z;wrt 6.3,R
43: wrt 6.3,C
44: for I=1 to 6;wrt 6.3,T[I];next I
45: W[13]-C→r6;wrt 6.3,r6;for I=14 to 16;wrt 6.3,W[I];next I
46: C-(W[14]+W[15]+W[16])/3→S
47: fmt 9,f8.2;wrt 6.9,S
48: fmt 1,40x,f7.2,z;wrt 6.1,T[7];for I=8 to 11;wrt 6.3,T[I];next I
49: fmt 2,f7.2;wrt 6.2,T[12]
50: gto 11
51: end
52: "CALT":
53: ret 1.29283e-5*p1*p1+.9945861644*p1+.1784832544
54: "COND":
55: ret ln(1.27/p1)/379*.0127*Q
56: "TSAT":
57: ret 139.276781+6.4757873p1-.1036991p1p1
58: "TEMP"
59: if p1<=1.494;ret 31.99925+46.80117p1-1.407396p1^2+.07802p1^3-.007394p1^4
60: if p1<=3.941;ret 33.42956+44.48835p1-.07422p1^2-.253895p1^3+.02878p1^4
61: if p1<=6.62;ret 33.82822+45.39092p1-1.015078p1^2+.035592p1^3-.000642p1^4
*14669

```

XIV. APPENDIX 6: ERROR ANALYSIS

The total error of a measurement process can be decomposed into two parts, the bias and the imprecision. Once the instrument has been calibrated by procedures as described in Appendix 3, the bias can be removed, and the remaining error is that due to the imprecision, which is called the random error or the nonrepeatability. The random error can be minimized through the experimental design but will always exist. It is necessary to estimate the total uncertainty of the experimental data by conducting a propagation-of-error analysis. The error analysis for all the physical quantity data reported, including heat flux, wall superheat, film flowrate, liquid feed height, and surface subcooling, is presented here.

The expression used to calculate the uncertainty W associated with any quantity Z is

$$W_Z = \left[\sum_{i=1}^n \left(\frac{\partial Z}{\partial X_i} W_{X_i} \right)^2 \right]^{1/2} \quad (A76)$$

where x_i is any of the n parameters of which the quantity Z is a function. Although eq. (A76) is applicable to random errors of different definitions, the 90 percent confidence limits are dealt with in this analysis. The contribution of individual source to the total uncertainty is determined by a weighing factor, $\frac{\partial Z}{\partial X_i}$.

The heat flux data presented were calculated based on eqs. (A35) and (A36). By evaluating the contributions from all the sources, it was found that the main source of uncertainty was associated with the electric

power measurement. The uncertainty of the calibrated wattmeter employed in the experiment was ± 2.5 W. (See Appendix 3B.) It was thus estimated that the uncertainty in heat flux was ± 220 W/m².

The wall superheat data were calculated by subtracting the saturation temperature and the temperature drop between the thermocouple bead and the base surface from the thermocouple readings, i.e.,

$$\Delta T = T_w - T_s - \Delta T_{\Delta r} \quad (A77)$$

The uncertainty in wall temperature after calibration was determined as ± 0.06 K. (See Appendix 3A.) The saturation temperature was calculated by an expression fitting data from steam tables. The atmosphere pressure used to calculate the saturation temperature was the main source of uncertainty. Nevertheless, the total uncertainty associated with the saturation temperature was negligible. The conductive temperature drop, $\Delta T_{\Delta r}$, was calculated according to eq. (A34) in Appendix 4A or eq. (40) in the section of data reduction. It was shown that the uncertainty associated with the heat flux or that with the power measurement, was the most outstanding. The error in the radial distance between the thermocouple bead and the base surface measured following the method described in Appendix 2 by a toolmaker's microscope, was determined as ± 0.01 mm. The uncertainty in the $\Delta T_{\Delta r}$ was estimated ± 0.01 K.

Based on the uncertainties estimated for the three terms, it was noticed that the total uncertainty in wall superheat was predominated by the temperature measurement and was estimated ± 0.06 K.

The flowrate measurement by the rotameter was the main source of uncertainty in the film flowrate calculated by eq. (36). The imprecision in the rotameter after calibration was ± 0.02 GPM, as given in Appendix 3C. Therefore, the uncertainty in the film flowrate Γ was ± 0.004 kg/s-m.

The liquid feed height was measured by a scale, with estimated error of ± 1 mm. The uncertainty in the ratio of feed height to the cylinder diameter was ± 0.1 .

The surface subcooling was measured by the calibrated temperature measurement system, for which the uncertainty was ± 0.06 K.